FOUR WAVE MIXING SPECTROSCOPY OF Cr^{3+} AND/OR Nd^{3+}-DOPED MIXED GARNET CRYSTALS

BY

FAQIR MIAN HASHMI

Bachelor of Science
University of Baluchistan
Quetta, Pakistan
1978

Master of Science
Southern Illinois University
Carbondale, Illinois
1983

Submitted to the Faculty of the
Graduate College of the
Oklahoma State University
in partial fulfillment of
the requirements for
the Degree of
DOCTOR OF PHILOSOPHY
July, 1992

FOUR WAVE MIXING SPECTROSCOPY OF

Cr^{3+} AND/OR Nd^{3+}-DOPED

MIXED GARNET

CRYSTALS

Thesis Approved:

Richard C. Powell
Thesis Adviser

Donna Kay Bundy

James P. Wicksted

John McKeever

Donald L. Thompson

Thomas C. Collins
Dean of the Graduate College

ACKNOWLEDGMENTS

I would like to express my thanks to all the people who provided material help or moral encouragement during the course of this work. First and foremost among them is my thesis advisor Dr. Richard C. Powell, who provided me the opportunity to work in his lab and displayed a perfect blend of patience, expertise and patronage during my training, as this process would have been much more difficult without his noble guidance. I would like to thank him for the joy and experience that I received while working in his laboratory. Dr. Stephen W. S. McKeever, Dr. Donna K. Bandy, Dr. James P. Wicksted and Dr. Donald L. Thompson are all gratefully acknowledged for agreeing to serve as members in my Ph. D. committee. Although their precious time, critique, and suggestions towards this project may never be compensated, it is guaranteed to help me in the future. Their willingness to respond to some short notices is highly appreciated. I would also like to thank the patience displayed by the staff in the Physics department as well as the Center for Laser Research. The financial opportunities provided by Dr. Larry H. Scott and Dr. Paul A. Westhause were immensely helpful. I am just one of the beneficiary of the role played by Dr. Westhause as Graduate Student Advisor and Associate Head of the Department of

Physics.

I would also like to thank God for providing me the energy, health, and patience to accomplish this goal. Last but not least, I could never forget the continuous support of my family. My parents (late) Salamat Hussain and Raeesa Begum Hashmi, my wife Azizah, my sister Jamila and my brother Wajid have contributed the most towards my achieving this goal. After a tiring day, my son, Sameer Asif Hashmi, provided the most pleasant sight one could wish for. My father had always emphasized the importance of education in ones life and It is to him and my mother that I dedicate this thesis.

I gratefully acknowledge the financial support for this work provided by a contract from the U.S. Army Research Office and by the National Science Foundation through grant No. DMR-87-22350. The samples used in this work were provided by Dr. George Boulon of Universite Claude Bernard Lyon I, France.

TABLE OF CONTENTS

LIST OF TABLES

LIST OF FIGURES

Figure Page

Figure Page

CHAPTER I

INTRODUCTION

The identification of a material as potential lasing medium requires a number of different processes including energy absorption, storage, migration and emission at appropriate wavelengths. These characteristics strongly depend upon properties and distribution of the active ions which in case of crystals, become quite complicated. The lack of microscopic probes makes it necessary to study the macroscopic phenomena sensitive to these microscopic parameters in order to extract the necessary information. Fluorescence lifetime quenching and site-selection spectroscopy have long been used to study the energy transfer in these and other materials. Although these techniques provide information on the total sensitizer-activator non-radiative energy transfer, they do not give an independent account of spatial energy migration which strongly depends upon the spatial distribution of active ions and their surroundings. The distribution and surroundings of active ions in crystals is very important in determining the inhomogeneous width of spectral lines which in turn affects the energy storage. Recently Four-Wave Mixing (*FWM*) spectroscopy has been very effective in studying long-range

energy migration in solids.[1-4] The transient Laser Induced Grating (*LIG*) created in these experiments is very sensitive to the characteristics of excited state of dopant ions. These characteristics also play an important role in lasing phenomenon.

Statement of the problem

The use of garnet crystals such as $Gd_3Ga_5O_{12}$ [GGG] and $Gd_3Sc_2Ga_3O_{12}$ [GSGG] doped with Cr^{3+} and/or Nd^{3+} as laser materials has stimulated an interest in the study of Physical properties of these and similar garnets. A good deal of research has been directed towards the study of material characteristics essential to lasing.[4-15] These characteristics can be altered by changing the material composition which can be accomplished by either studying other garnets such as $La_2Lu_3Ga_3O_{12}$ [LLGG][16] or by additional doping of optically inactive ions. Using the latter approach, a new mixed garnet crystal [GGGM], with the chemical formula $(Gd,Ca)_5(Ga,Mg,Zr)_2Ga_3O_{12}$, was grown by *CHRISMATEC* company in France.[12] The kinetics of pump energy strongly depends upon energy levels of the optically active ions which in case of chromium, are determined primarily by unshielded 3d-electrons and, therefore, the host lattice can strongly influence the energy transfer and optical dephasing characteristics in such materials. An understanding of how the crystal structure affects dephasing and energy transfer in Cr-doped materials is therefore essential. To this end,

Four-Wave Mixing spectroscopy is a useful tool.

In this thesis, four-wave mixing spectroscopy and fluorescence dynamics techniques are employed to study energy transfer and optical dephasing phenomena in these mixed garnet crystals doped with chromium and/or neodymium ions.

Summary of the thesis

Previous studies of the spectroscopic properties as well as preliminary *FWM* results on GGG, GSGG, and GGGM have been reported earlier.[3,4,12-15] This study extends the previous work by using *FWM* techniques to study optical dephasing and energy transfer among the Cr^{3+} and the Nd^{3+} ions by pumping into $^4T_2$ and $^4T_1$ bands of the Cr^{3+} ions and $^4G_{7/2}$ level of Nd^{3+} ions in GGGM. The results are compared to those obtained previously in other laser crystals doped with Cr^{3+} and/or Nd^{3+} ions. The fluorescence dynamics measurements are used to investigate overall nonradiative energy transfer from initially excited Cr^{3+} ions to Nd^{3+} ions in the codoped sample.

Chapter II describes the samples and outlines the experimental techniques used in these studies. The absorption and emission spectra of the samples used in this work are also discussed in this chapter. Theoretical models used to analyze the optical dephasing and the energy transfer data have been outlined in *chapter III*. In *chapter IV*, we provide the experimental data, its analysis using

the models described in *chapter III*, and discussion. The results are then compared with similar studies on other laser crystals. The presence of some common trends in the variation of these properties as a result of changing the host matrix have been identified and some possible explanations have been suggested. The conclusions and suggestions for future work are provided in *chapter V*.

CHAPTER II

OPTICAL SPECTRA AND EXPERIMENTAL DETAILS

Samples

The garnet unit cell is *cubic* with O_h symmetry.[17-19] It has a very complicated structure with three distinct site symmetries and a general chemical formula of the type $C_3A_2D_3O_{12}$, where *C* stands for dodecahedral sites with Oxygen coordination number *8*, *A* is for octahedral sites with coordination number *6* and *D* represents tetrahedral sites with coordination number *4*. Figure 1 shows an octant of this very complicated garnet structure,[19] where these three site symmetries are shown explicitly. Table I gives the coordinates of each atom in terms of the lattice parameter.

The interest in the study of Cr-doped material was enhanced with the development of *ruby laser* and the introduction of *vibronic lasers* further emphasized the need to understand the properties of these materials as best as possible. One important parameter in such materials is the crystal field splitting between ^2E and $^4T_2$ levels. The optical spectra of the transition metal ions are primarily determined by unshielded 3d valence electrons. When inside the crystal, these electrons are strongly affected by the

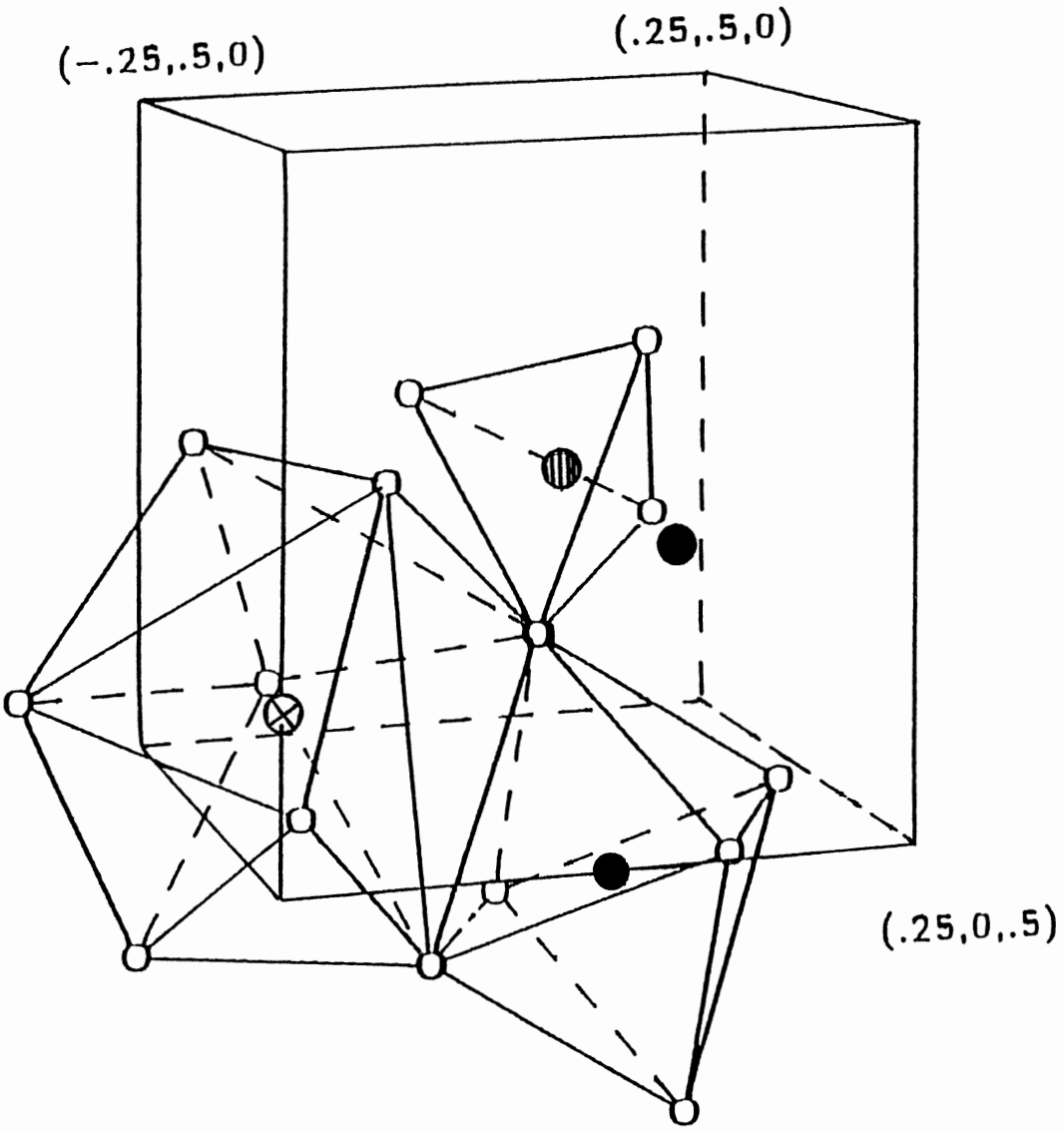

Figure 1. An Octant of Garnet Crystal Structure Showing Three Distinct Sites. [⊗ - Dodecahedral, ● - Octahedral, and ◍ - Tetrahedral.]

TABLE I

POSITION OF CATIONS (IN UNITS OF LATTICE CONSTANT) IN $(Gd,Ca)_3(Ga,Mg,Zr)_2Ga_3O_{12}$ CRYSTALS

X	Y	Z	X	Y	Z
Dodecahedral Sites (Gd^{3+}, Ca^{2+})					
1/8	0	1/4	-1/8	0	-1/4
1/8	1	1/4	-1/8	1	-1/4
5/8	0	1/4	-5/8	0	-1/4
5/8	1	1/4	-5/8	1	-1/4
1/4	1/8	0	-1/4	-1/8	0
1/4	1/8	1	-1/4	-1/8	1
1/4	5/8	0	-1/4	-5/8	0
1/4	5/8	1	-1/4	-5/8	1
0	1/4	1/8	0	-1/4	-1/8
1	1/4	1/8	1	-1/4	-1/8
0	1/4	5/8	0	-1/4	-5/8
1	1/4	5/8	1	-1/4	-5/8
5/8	1/2	3/4	1/8	1/2	3/4
3/4	5/8	1/2	3/4	1/8	1/2
1/2	3/4	5/8	1/2	3/4	1/8
3/8	1/2	1/4	-1/8	1/2	1/4
1/4	3/8	1/2	1/4	-1/8	1/2
1/2	1/4	3/8	1/2	1/4	-1/8

TABLE I (Continued)

X	Y	Z	X	Y	Z
Octahedral Sites (Ga^{3+}, Mg^{2+}, Zr^{4+})					
0	0	0	1	0	0
0	1	0	0	0	1
1	1	0	1	0	1
0	1	1	1	1	1
1/2	0	0	0	1/2	0
0	0	1/2	0	1/2	1/2
1/2	0	1/2	1/2	1/2	0
1/2	1	0	1/2	0	1
1	1/2	0	1	0	1/2
0	1	1/2	0	1/2	1
1/2	1/2	1/2	1/2	1/2	1
1/2	1	1/2	1	1/2	1/2
1/2	1	1	1	1/2	1
1	1	1/2	1/4	1/4	1/4
1/4	1/4	3/4	3/4	1/4	1/4
1/4	3/4	1/4	1/4	3/4	3/4
3/4	1/4	3/4	3/4	3/4	1/4
3/4	3/4	3/4			
Tetrahedral Sites (Ga^{3+})					
3/8	0	1/4	3/8	1	1/4
7/8	0	1/4	7/8	1	1/4

TABLE I (Continued)

X	Y	Z	X	Y	Z
-3/8	0	-1/4	-3/8	1	-1/4
-7/8	0	-1/4	-7/8	1	-1/4
1/4	3/8	0	1/4	3/8	1
1/4	7/8	0	1/4	7/8	1
-1/4	-3/8	0	-1/4	-3/8	1
-1/4	-7/8	0	-1/4	-7/8	1
0	1/4	3/8	1	1/4	3/8
0	1/4	7/8	1	1/4	7/8
0	-1/4	-3/8	1	-1/4	-3/8
0	-1/4	-7/8	1	-1/4	-7/8
3/4	7/8	1/2	1/2	3/4	7/8
3/8	1/2	3/4	3/4	3/8	1/2
1/2	3/4	3/8	1/8	1/2	1/4
1/4	1/8	1/2	1/2	1/4	1/8
-3/8	1/2	1/4	1/4	-3/8	1/2
1/2	1/4	-3/8	7/8	1/2	3/4

96 Oxygen ions are at general positions derived from an initial set of values (ζ x + η y + γ z) by all 96 operations. The 48 of these arise due to the space group elements and the other 48 can be obtained by adding (1/2,1/2,1/2). In most garnets ζ = 0.04, η = 0.05 and γ = 0.65

local crystal field and subsequent changes in the spectra are quite noticeable. For instance, the crystal field splitting between ^2E and $^4T_2$ levels ranges from -1000 cm^{-1} in LLGG[13] to 2300 cm^{-1} in ruby[20]. The tightly packed unit cell of garnet crystals is so sensitive to the size of substitutional ions that the lattice parameter changes from 12.01 Å in $Yb_3Al_5O_{12}$ (YAG)[13] to 12.57 Å in GSGG.[13] The corresponding crystal field strength changes from 1000 cm^{-1} in YAG[13] to 50 cm^{-1} in GSGG[4].

The mixed garnet crystals are obtained by introducing additional optically inactive ions in $Gd_3Ga_2Ga_3O_{12}$ crystals causing multiple ions to occupy crystallographic sites. The GGGM crystals are grown by substituting 10% of Gd^{3+} ions in dodecahedral sites by Ca^{2+} ions and 50% of Ga^{3+} ions in octahedral sites by Zr^{4+} and Mg^{2+} ions in GGG.[12] These substitutions result in a relatively high segregation coefficient of 2.8 for the Cr^{3+} ions and a larger lattice constant of 12.4942 Å. The segregation coefficient for Nd^{3+} ions in GGGM however improves to 0.75 from a low value of 0.2 in YAG. The increased value of lattice constant results in larger $Cr - O$ distances which lowers the crystal field splitting between ^2E and $^4T_2$ levels of the Cr^{3+} ions to 100 cm^{-1} in GGGM.[13] This is intermediate between the crystal field splittings of 298 cm^{-1} in the case of GGG[4] and 50 cm^{-1} for GSGG.[4] In addition, there are several nonequivalent sites for Cr^{3+} ions which causes spectral structure and significant inhomogeneous broadening of the

optical transitions. The large inhomogeneous broadening raises the concentration quenching limit making it possible to search for the optimum concentration. It also lowers the value of the stimulated emission cross-section which is desirable in the development of high average power lasers.

Three samples doped with Cr^{3+} only (Cr:GGGM), Nd^{3+} only (Nd:GGGM), and codoped with Cr^{3+} and Nd^{3+} (Cr,Nd:GGGM) used in these studies, were grown at the *CHRISMATEC* company in France by standard Czochralski method[13] and mechanically polished to reduce the surface scattering. The samples, are shown in Fig. 2 and the related information is provided in Table II.

Absorption And Emission Spectra

Room temperature absorption spectra of these samples were recorded by an *IBM 9430 UV-Visible* spectrophotometer. The room temperature absorption spectrum of Cr:GGGM shown in Fig. 3, is dominated by two strong absorption bands centered at 460 nm and 640 nm. Figure 4 shows *Tanabe-Sugano diagram*[21] for $3d^3$ ions. The parameter $\Delta E_{pp}/B$ is plotted along the horizontal axis whereas the vertical axis is the energy axis. Here ΔE_{pp} is the difference in energy between the peaks corresponding to $^4A_2$ - $^4T_2$ and $^4A_2$ - ^2E transitions in the absorption spectrum of Cr^{3+} ions and B is the *Racah parameter*. The energy levels along the solid vertical line show the corresponding order of levels for Cr^{3+} ions in GGGM. A comparison of the energy levels in

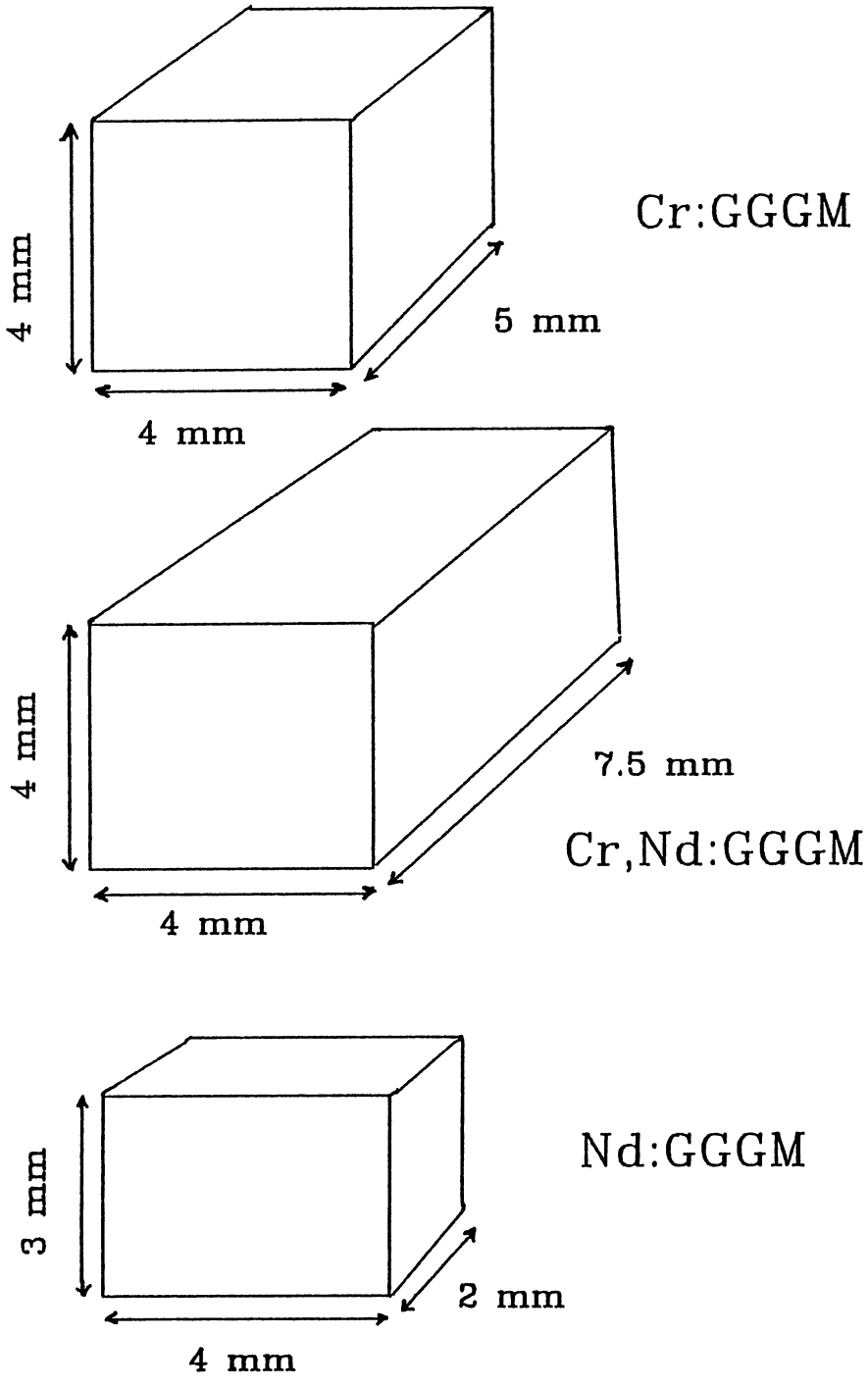

Figure 2. The Samples Used in These Studies With Corresponding Sizes.

TABLE II

SAMPLE DIMENSIONS AND DOPANT CONCENTRATIONS

Sample	Dimensions (mm^3)	Dopant Ions	Dopant Concentration (at. %)
Cr:GGGM	4 x 4 x 5	Cr^{3+}	0.30
Cr,Nd:GGGM	4 x 4 x 7	Cr^{3+} Nd^{3+}	0.20 2.80
Nd:GGGM	3 x 4 x 2	Nd^{3+}	2.80

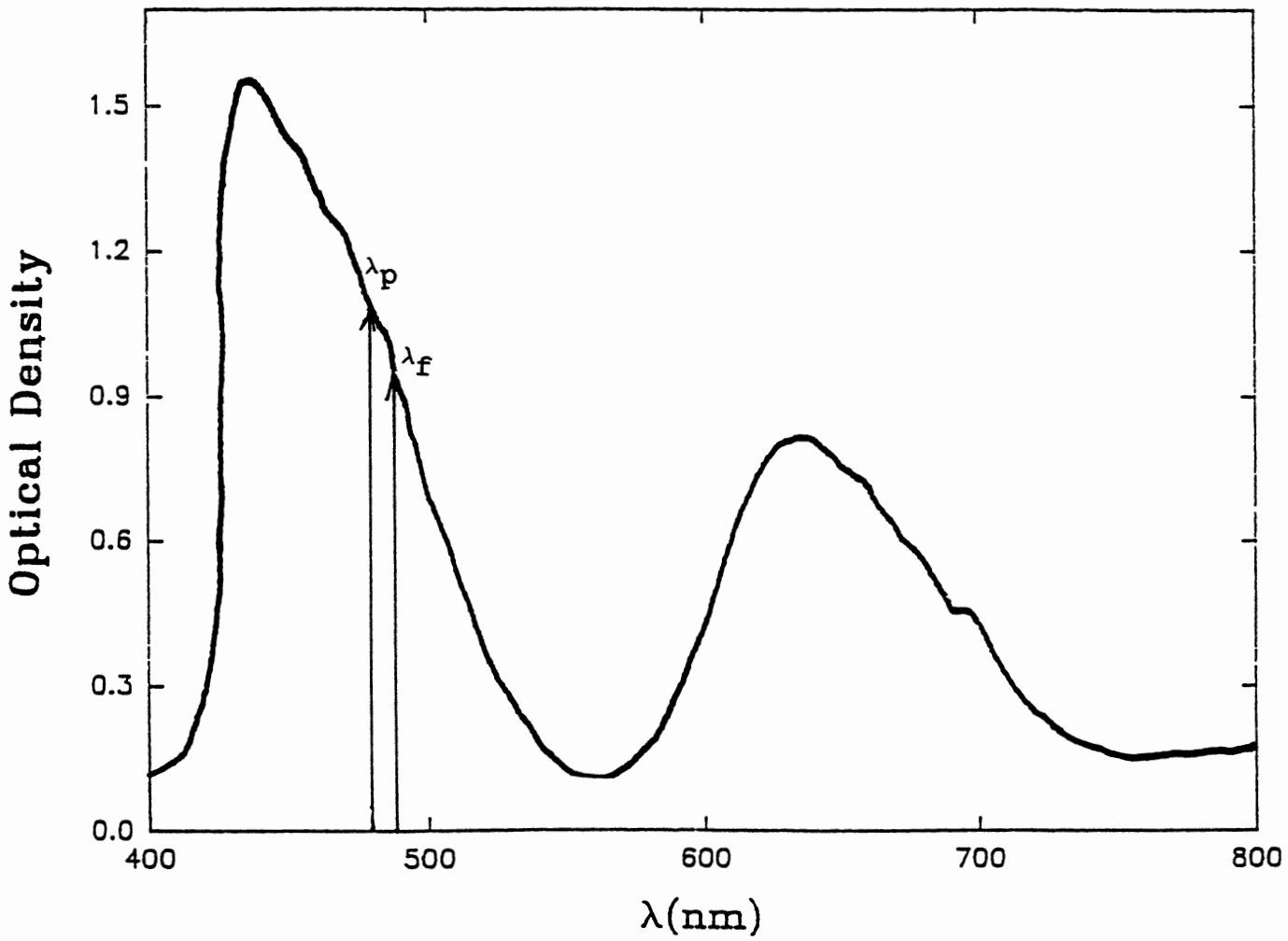

Figure 3. Room Temperature Absorption Spectrum of Cr:GGGM. λ_p and λ_f Represent the Laser Wavelengths Used for the Fluorescence Dynamics and the FWM Spectroscopy.

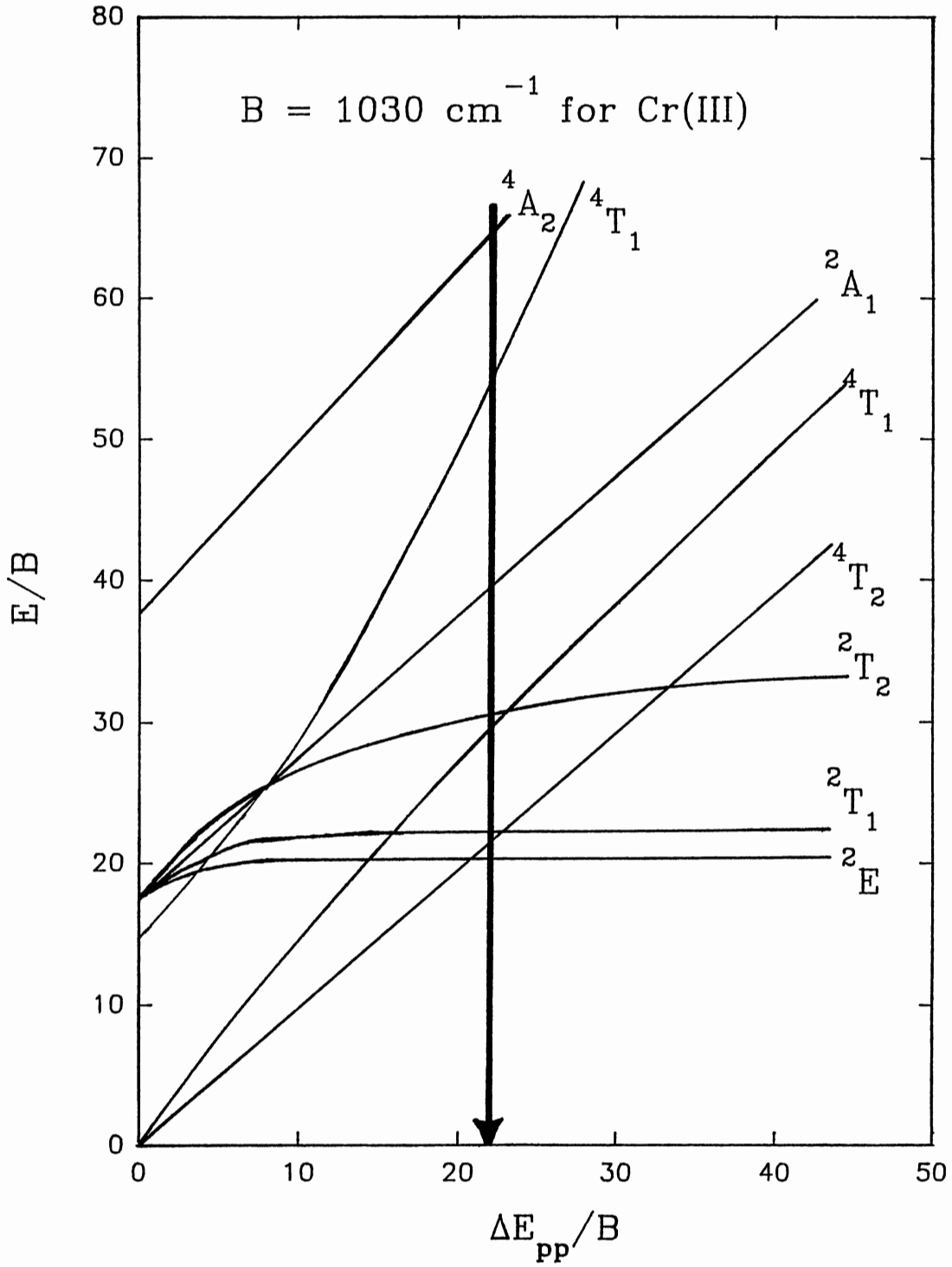

Figure 4. Tanabe-Sugano Diagram for Cr^{3+} Ions. The Vertical Line Corresponds to Crystal Field Values for Cr^{3+} Ions in GGGM.

Fig. 4 and the observed absorption spectrum in Fig. 3 shows that the higher energy band is due to $^4A_2$ - $^4T_1$ absorption transition and the lower energy band is due to $^4A_2$ - $^4T_2$ absorption transition of Cr^{3+} ions and the shoulder around 695 nm is due to the $^4A_2$ - ^2E absorption transition. The dips in the lineshape on the low energy side of $^4A_2$ - $^4T_1$ and $^4A_2$ - $^4T_2$ bands are due to overlap with the sharp, relatively weak, spin forbidden transitions from $^4A_2$ ground state to $^2T_1$ and $^2T_2$ levels respectively.

The relatively sharp lines in Fig. 5, for the room temperature absorption spectrum of Nd:GGGM are due to absorption transitions of the Nd^{3+} ions in GGGM. The inhomogeneous width of these spectral lines are much larger than the corresponding widths in other hosts.[13] Figure 6 shows the absorption spectrum of the codoped sample (Cr,Nd:GGGM). In this sample, the broad features due to absorption by Cr^{3+} ions, are overlapped by sharp features due to absorption transitions of Nd^{3+} ions in GGGM. The vertical lines in the absorption spectra labeled as λ_f and λ_p are respectively the write beam wavelengths used in the four-wave mixing experiments (to be described later) and the pump wavelength used to obtain the emission spectra in these samples.

Figure 7 shows the experimental setup used to measure the emission profile. The emission spectrum was excited by a laser beam of wavelength λ_p from *Coumarine 480* dye in a nitrogen laser-pumped dye laser, analyzed with a 1-*m*

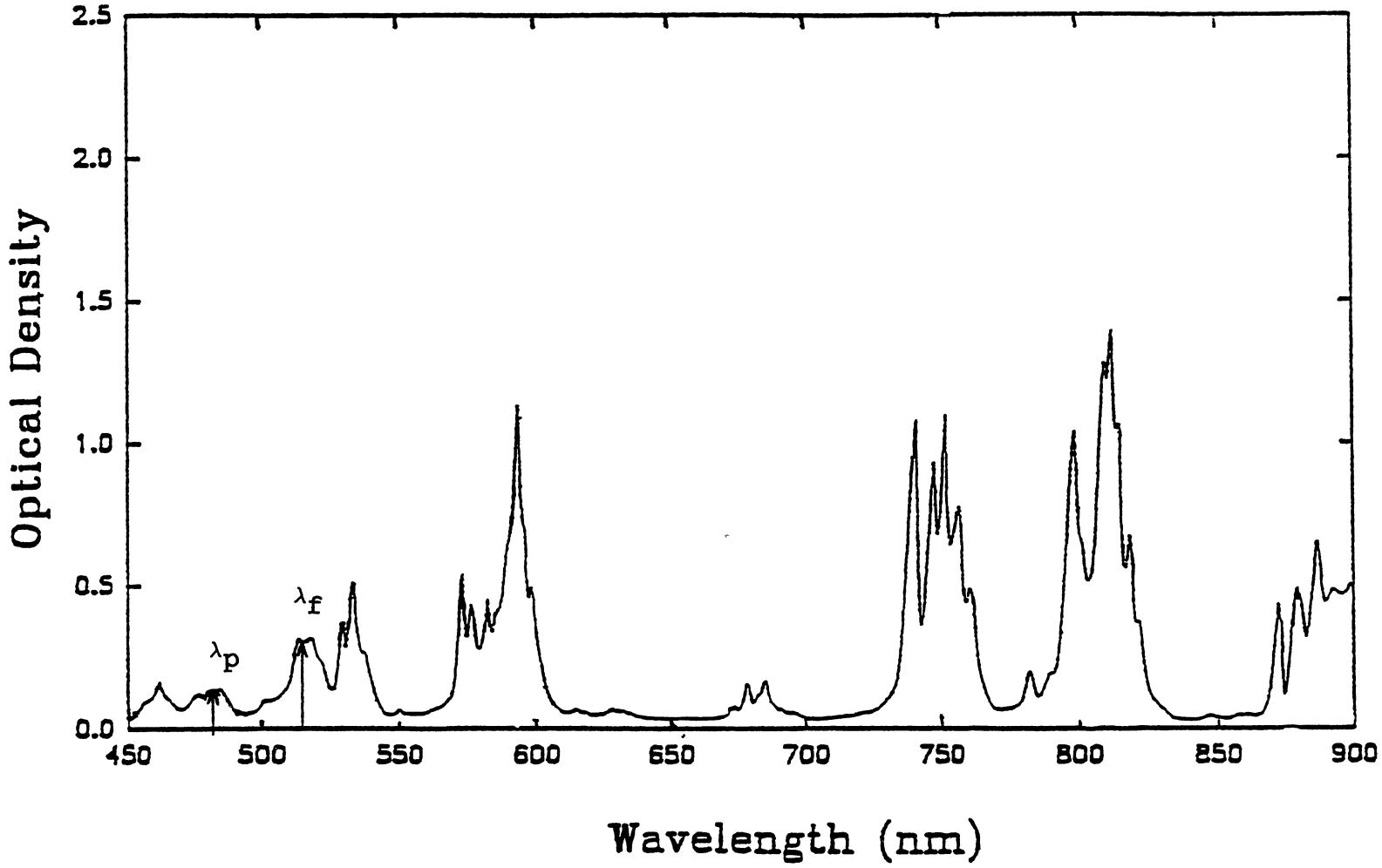

Figure 5. Room Temperature Absorption Spectrum of Nd:GGGM. λ_p and λ_f Represent the Laser Wavelengths Used for the Fluorescence Dynamics and FWM Spectroscopy.

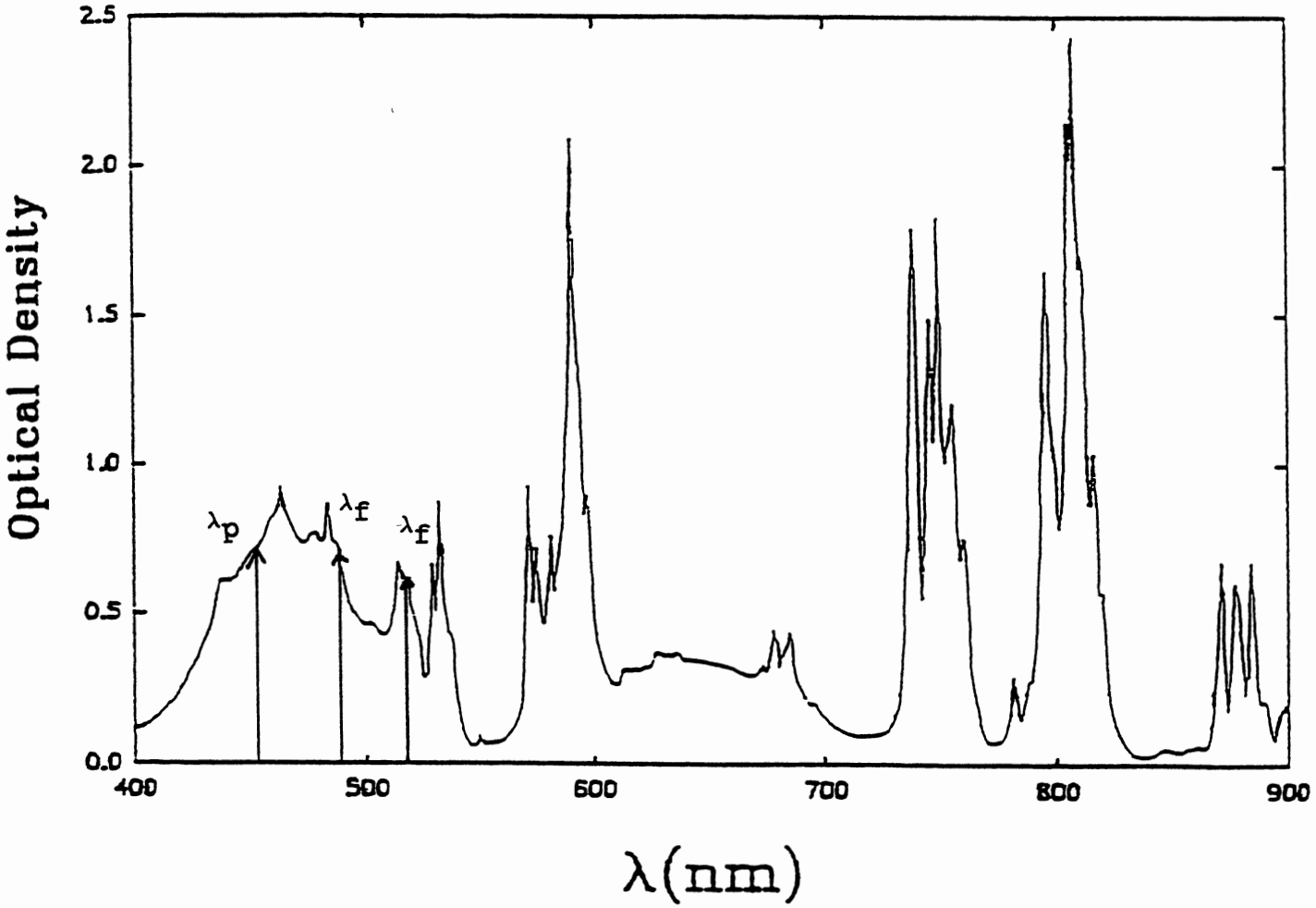

Figure 6. Room Temperature Absorption Spectrum of Cr,Nd:GGGM. λ_p and λ_f Represent the Laser Wavelengths Used for Fluorescence Dynamics and FWM Spectroscopy.

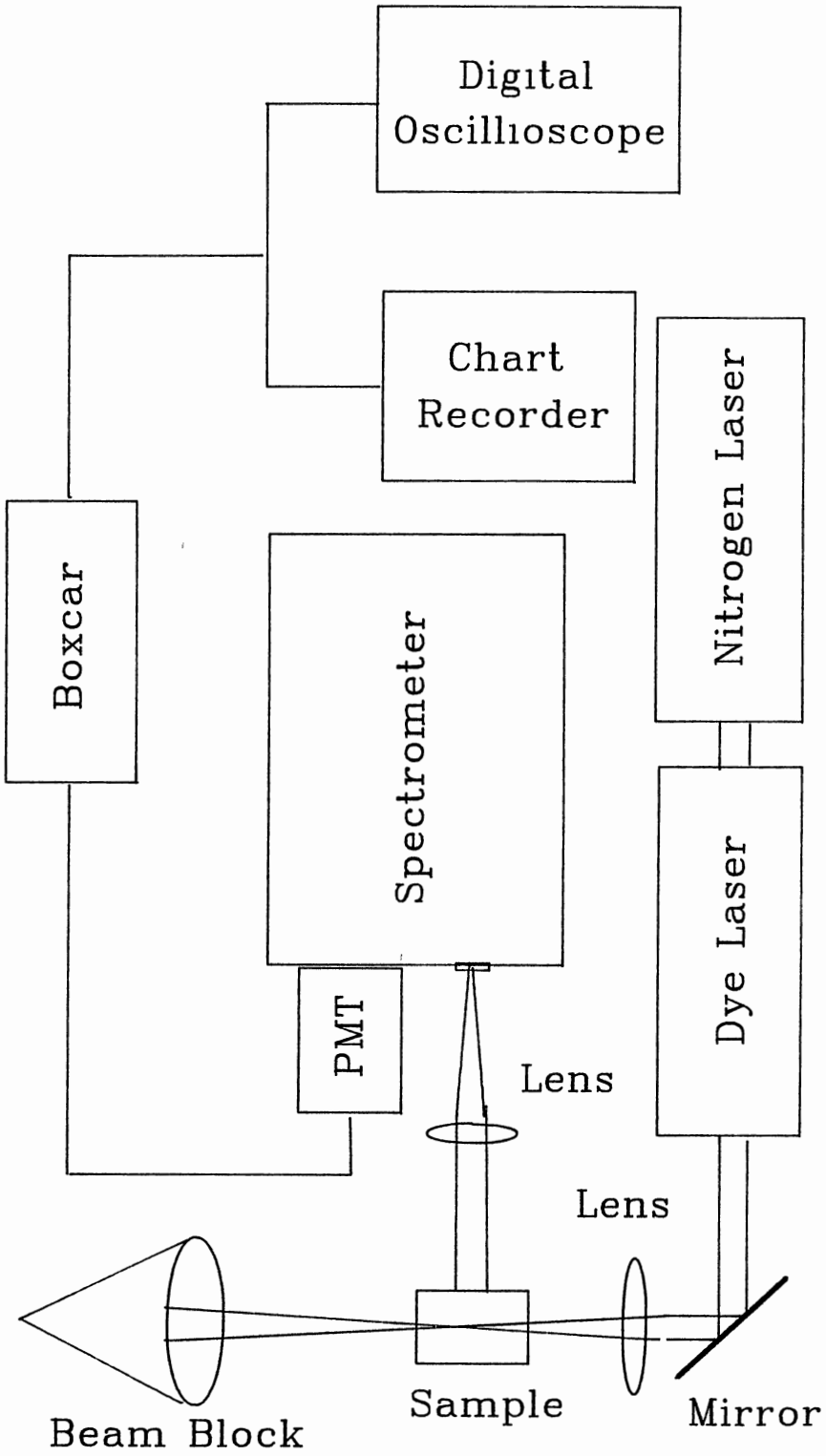

Figure 7. Experimental Setup Used to Measure the Emission Spectrum

spectrometer, and detected by an *RCA C31034* photomultiplier tube. The room temperature emission spectrum from Cr:GGGM sample is shown in Fig. 8. The fluorescence from Cr:GGGM is characterized by a very broad, Stokes-shifted emission due to $^4T_2$ - $^4A_2$ transition in Cr^{3+} ions centered at 750 nm with ^2E - $^4A_2$ transition manifesting itself as a shoulder at 695 nm. The fluorescence in Fig. 9, for the case of Nd:GGGM, is dominated by inhomogeneously broadened line at 1.064 μm. Figure 10 shows the fluorescence from Cr,Nd:GGGM sample at 20 K. The broad fluorescence due to Cr^{3+} in the codoped sample, is quenched by the radiative re-absorption by the Nd^{3+} ions.

For lifetime measurements, the sample was kept in a cryostat and the temperature was varied from 10 K to 250 K using a *CTI Cryogenics* closed-cycle helium refrigerator and a *Lake Shore Cryotronics* model 805 temperature controller. The temperature measurements were accurate to within 0.5 K. The fluorescence from Nd:GGGM were single exponentials, with lifetime ranging from 268 μsec at 10 K to 196 μsec at room temperature. However, the fluorescence from Cr:GGGM were double exponentials and the lifetimes of the short and long component at 10 K are 110 μsec and 215 μsec respectively. This is consistent with the presence of two crystal field sites in the sample. The relatively short lifetimes of the Cr^{3+} ions are consistent with the fluorescence being dominated by emission from $^4T_2$ level rather than the long-lived metastable ^2E level. The temperature

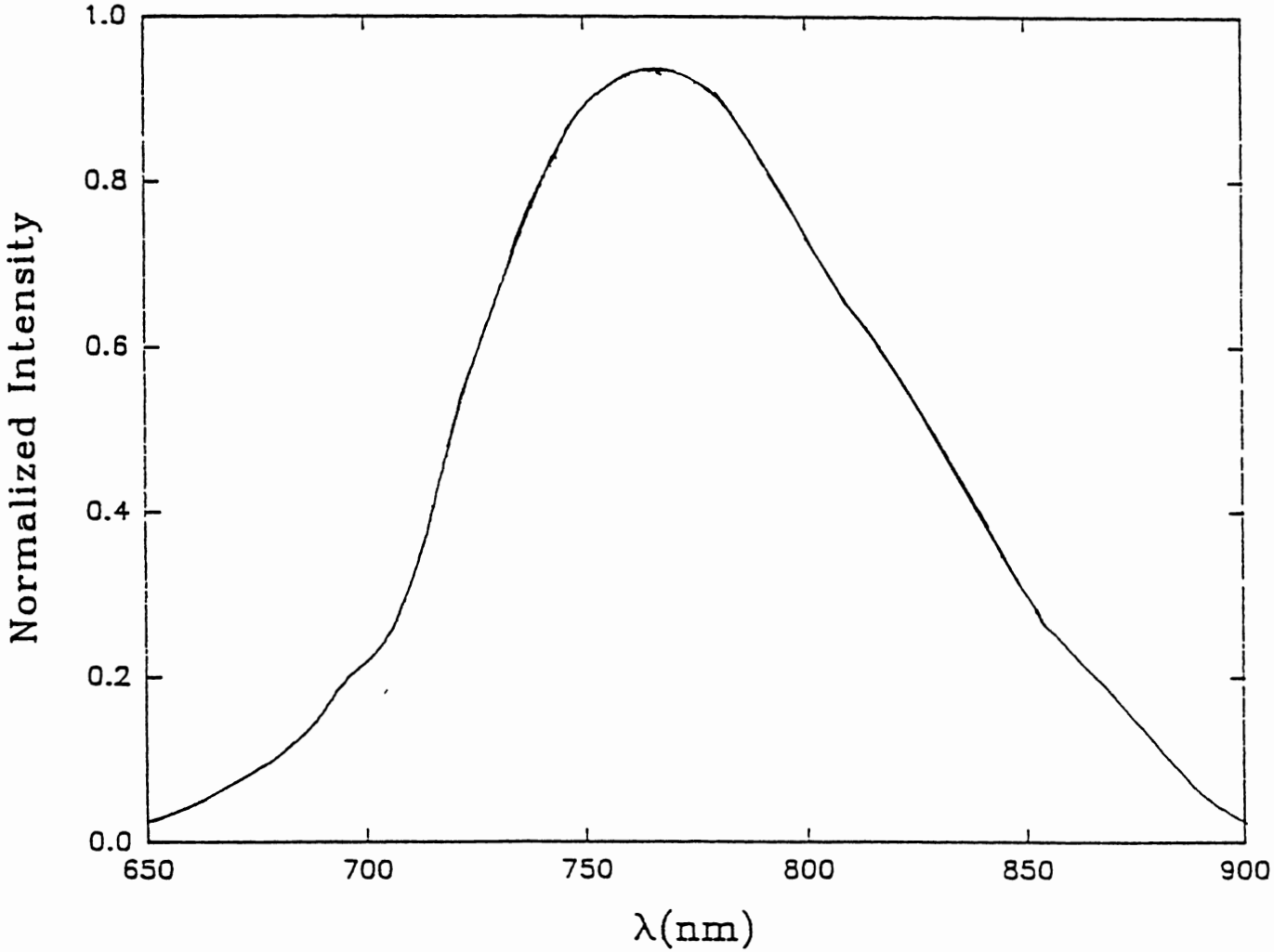

Figure 8. Room Temperature Emission Spectrum of Cr:GGGM.

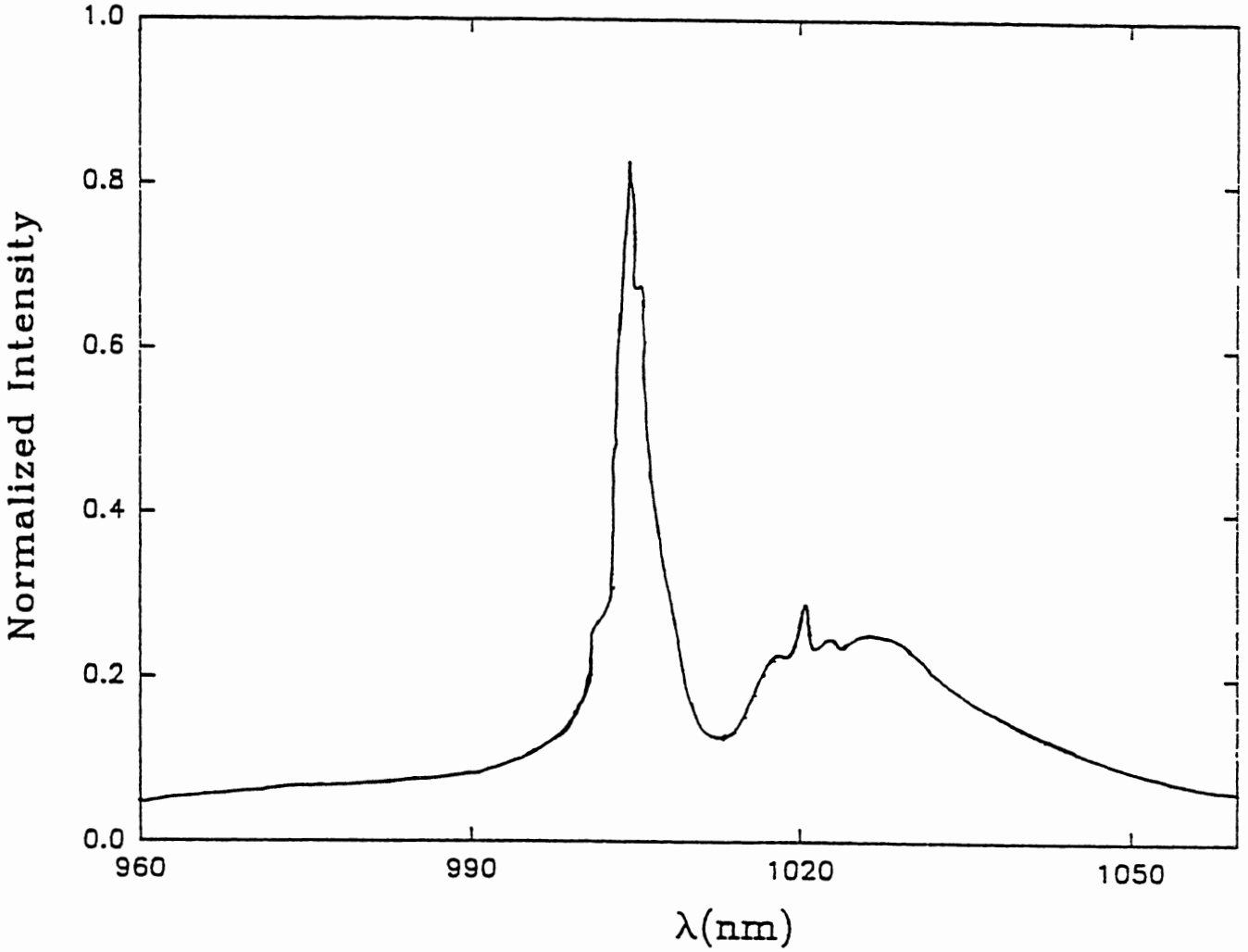

Figure 9. Room Temperature Emission Spectrum of Nd:GGGM.

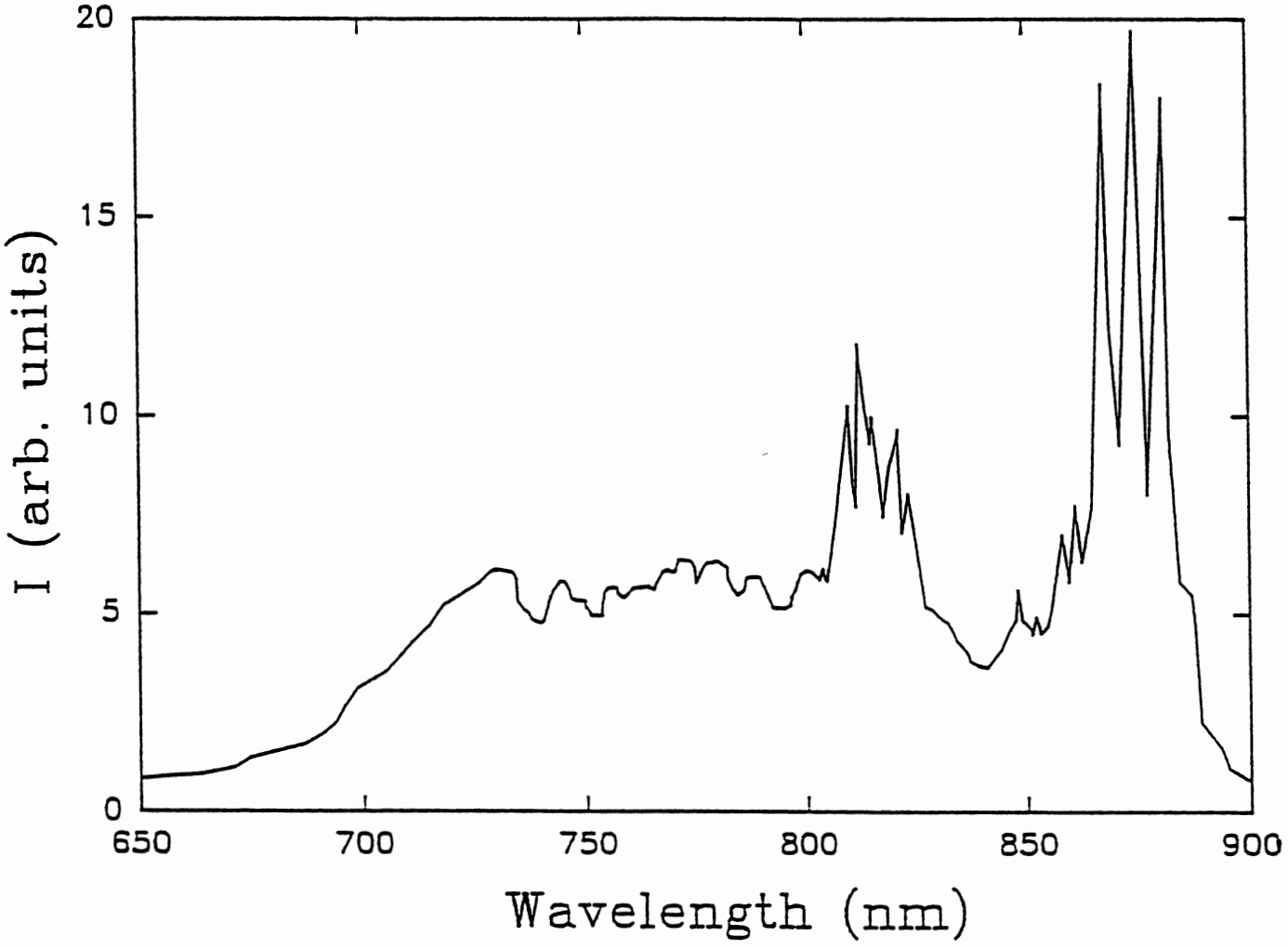

Figure 10. Room Temperature Emission Spectrum of Cr,Nd:GGGM.

dependence of the fluorescence lifetime of Nd^{3+} ions and the short component of Cr^{3+} ion fluorescence in GGGM are shown in Fig. 11 and Fig. 12 respectively.

In Cr:GGGM sample, both $^4T_2$ and ^2E levels are in thermal equilibrium and the resulting fluorescence lifetime is a weighted sum of intrinsic lifetimes of these levels. Temperature dependence of fluorescence lifetime τ_f, can be associated with the change in relative population of the two levels. Assuming Boltzmann population distribution, the measured fluorescence lifetime is given by[4]

$$\tau^{-1} = [\tau_E^{-1} + \tau_T^{-1}\exp(-\Delta E/kT)]/[1 + \exp(-\Delta E/kT)], \qquad (II-1)$$

where τ_E and τ_T are the intrinsic lifetimes of ^2E and $^4T_2$ levels respectively and ΔE is the energy separation of the two levels which in our case is 100 cm^{-1}. τ_E and τ_T were used as the fitting parameters and their values for the best fit were τ_E = 290 μsec and τ_T = 40 μsec.

Theoretical fit to temperature dependence of the fluorescence lifetime of Nd^{3+} ions in Nd:GGGM sample was obtained by the following expression.

$$\tau_f^{-1} = \tau_i^{-1} + C/[\exp(\hbar\omega/kT)-1], \qquad (II-2)$$

where τ_i is the intrinsic lifetime of $^4F_{3/2}$ level, C is a constant and ω is the phonon frequency. The second term in *Eq. (II-2)* represents the quenching of intrinsic lifetime due to nonradiative processes involving the absorption of phonons of energy $\hbar\omega$. Experimental data (Circles) in Fig.

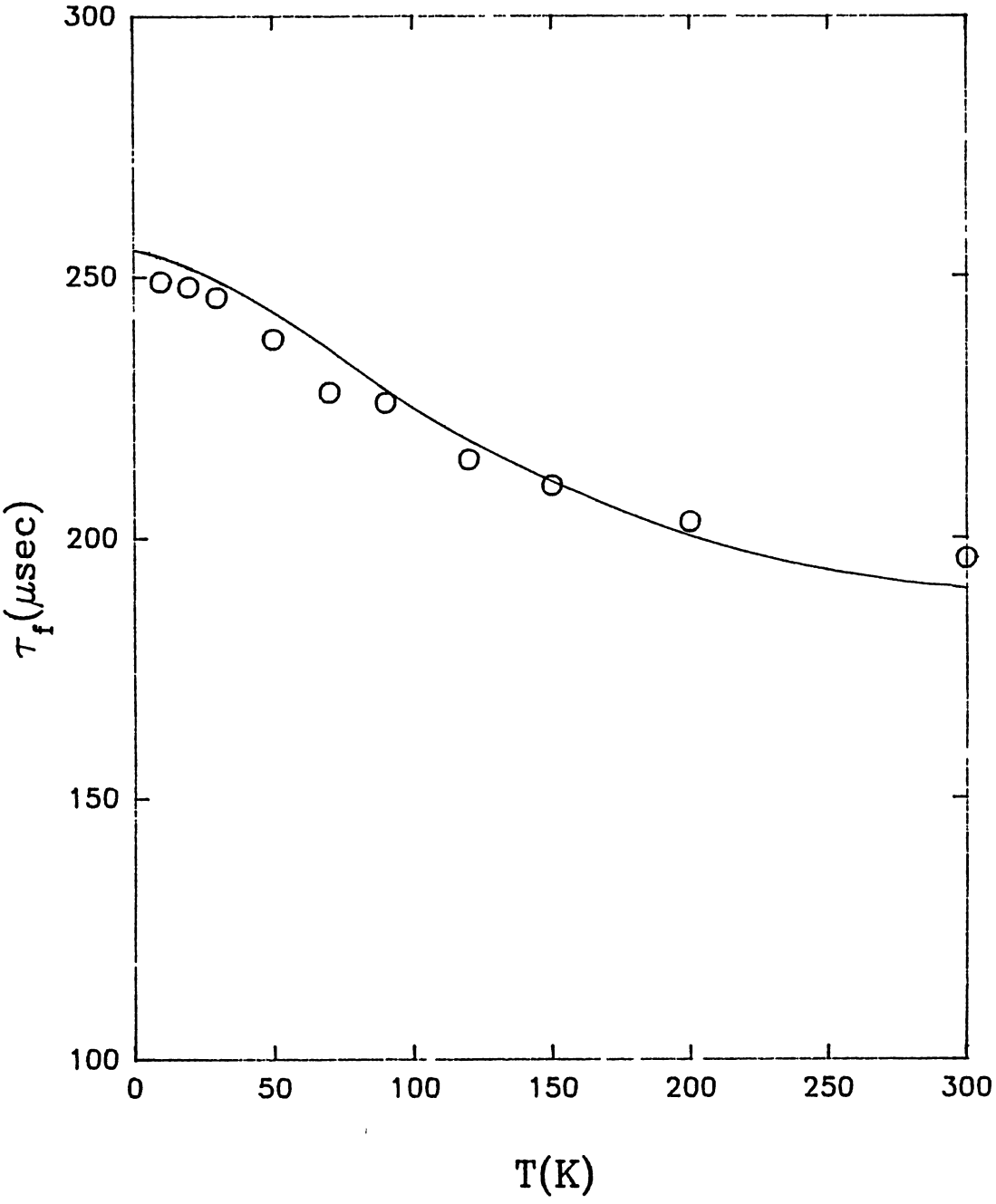

Figure 11. Temperature Dependence of the Fluorescence Lifetime of Nd^{3+} Ions in Nd:GGGM. The Circles Represent Experimental Points and the Curve Represents Theoretical Fit to the Data. (See Text for Explanation)

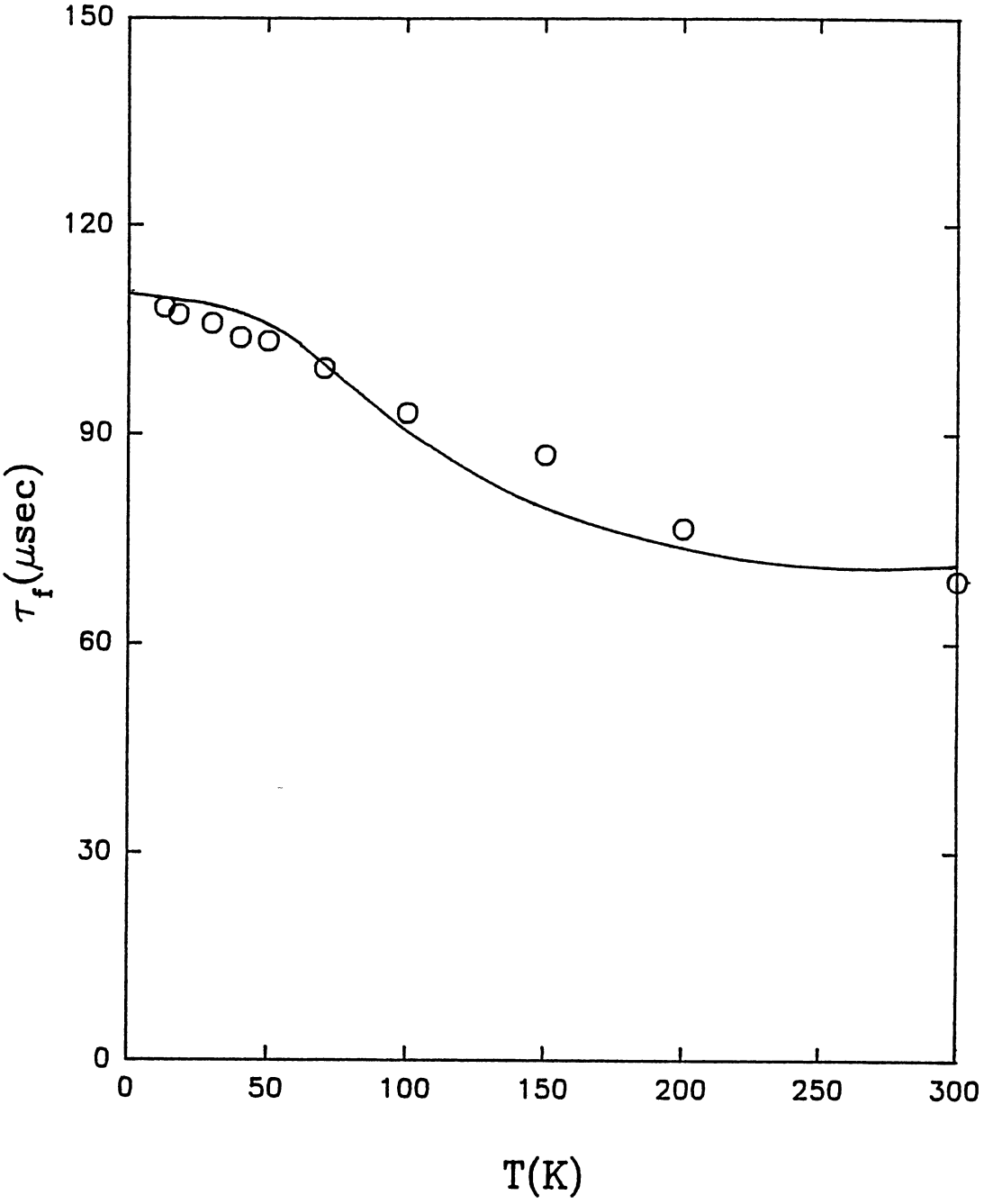

Figure 12. Temperature Dependence of the Fluorescence Lifetime of Cr^{3+} Ions in Cr:GGGM. The Circles Represent Experimental Points and the Curve Represents Theoretical Fit to the Data. (See Text for Explanation)

11 were fit to *Eq. (II-2)* using C, τ_i and ω as adjustable parameters and for the best fit C = 1625 μsec, τ_i = 287 μsec and ω = 47 cm^{-1}. The long component in Cr^{3+} ion fluorescence had the same temperature dependence as the short component.

Four-Wave Mixing Spectroscopy

FWM is an effective method for studying long range energy migration and optical dephasing phenomenon among dopant ions in solids.[1-4] The details of the procedure for using *FWM* techniques as a versatile spectroscopic tool have been described in numerous publications.[22-27] Figure 13 shows the setup used in these experiments. Emission from a *Spectra Physics* argon ion laser or argon ion laser-pumped ring dye laser was passed through a chopper and divided into two beams of equal intensities using a 50/50 beam splitter (*BS*). These two non-collinear laser beams are then focused onto the sample using appropriate mirrors M_2, M_3 and M_4. The path length is adjusted such that the two write beams cross inside the sample creating a sinusoidal interference pattern. Since the energy of laser photons is resonant with the energy of an electronic transition of the active ions, an excited state population grating is created having the same spatial pattern. This population grating produces a sinusoidal variation in the refractive index due to difference in the polarizabilities of Cr^{3+} ions in the excited state versus the ground state. A very low power

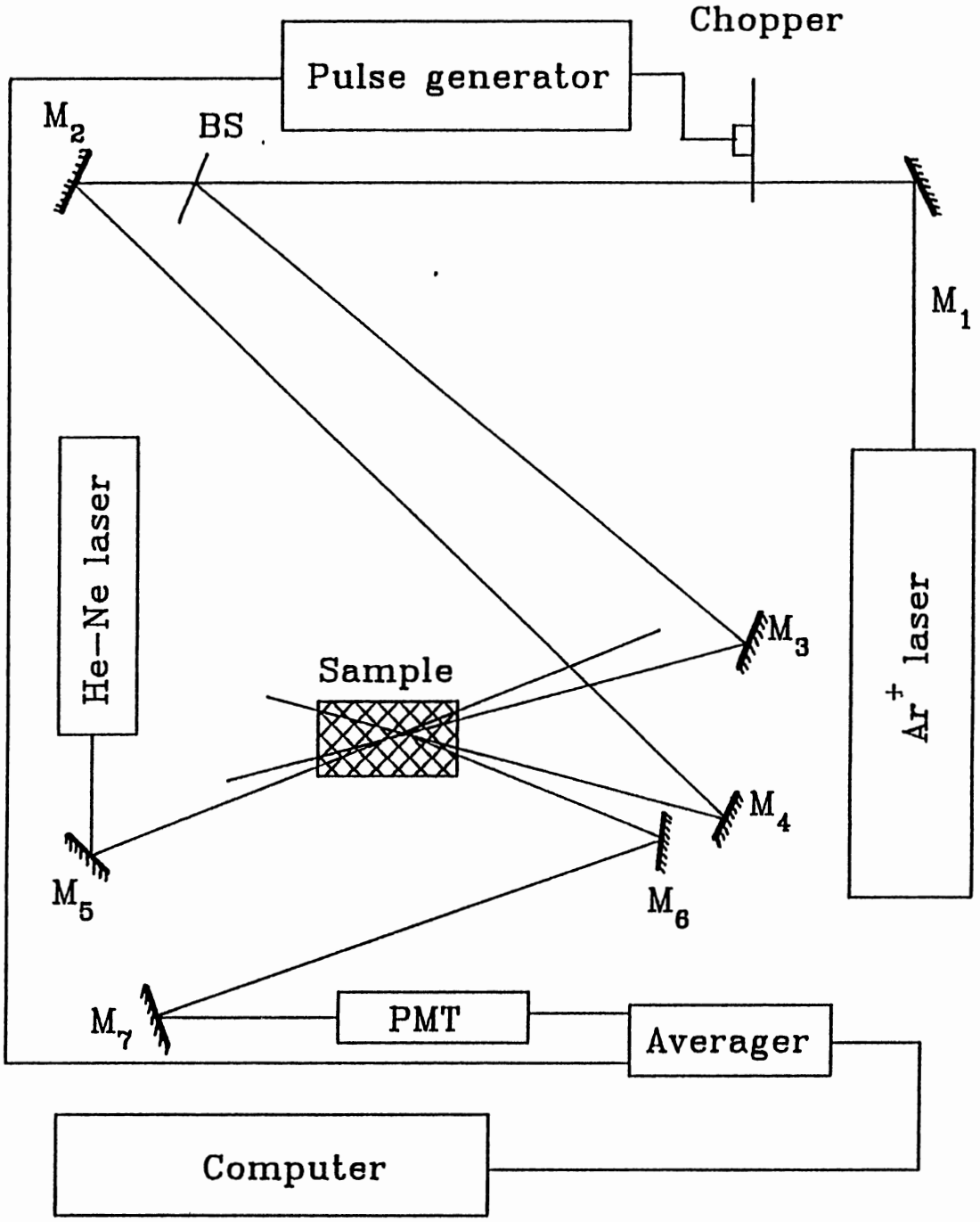

Figure 13. Experimental Setup Used for Four-Wave Mixing Spectroscopy, BS - Beam Splitter and M - Mirror. For Excitation Into the $^4T_2$ Band of Cr^{3+} Ions, an Argon Ion Laser-Pumped Ring Dye Laser was Used.

helium-neon laser beam nearly counterpropagating to one of the write beams is scattered off of this grating. When the *Bragg condition* is satisfied, a diffracted beam, called the *FWM* signal beam, nearly counterpropagating to the second write beam is observed. This *FWM* signal is then directed to an *RCA C31034* photomultiplier tube (*PMT*) using mirrors M_6 and M_7. The output from *PMT* is taken into an *EG&G Princeton Applied Research model 4202* signal averager (*averager*) and then to an *IBM XT* personal computer where the digital data is stored. The trigger to signal averager was provided by the chopper and pulse generator assembly. The sample was kept in a cryostat and *CTI-Cryogenics* closed cycle helium refrigerator and a Lake *Shore Cryotronics* model 805 temperature controller was used to control the temperature.

CHAPTER III

THEORETICAL MODEL

Four-Wave Mixing

In *FWM* techniques, two coherent laser beams interfere inside the sample to establish a sinusoidal intensity pattern. Since the laser wavelength is resonant with an electronic transition of active ions, light interacts with optical constants of the material to establish a similar spatial pattern of the excited active ions known as the Laser Induced Grating (*LIG*). The difference in polarizabilities between the excited state and the ground state of the ions acts like an excited state population grating with a grating wavevector $\vec{K}_g$ given by,

$$\vec{K}_g = \vec{K}_b - \vec{K}_a, \qquad \text{(III-1)}$$

where $\vec{K}_a$ and $\vec{K}_b$ are the wavevectors of the two write beams respectively. The spacing Λ of such a grating pattern is given by

$$\Lambda = \lambda/2\sin(\theta/2), \qquad \text{(III-2)}$$

where θ and λ are the crossing angle and the wavelength of write beams respectively. The pictorial representation of the *FWM* configuration used in these experiments is given in

Fig. 14. The two laser beams creating the grating are often referred to as the write beams. A third, much weaker laser beam with a wavevector $\vec{K}_p$ can be used to probe the depth of the grating. When the *Bragg condition* is satisfied, we observe a diffracted beam, called the *FWM* signal beam. The wavevector $\vec{K}_s$ of the signal beam is determined by the *Bragg condition* as

$$\vec{K}_s = \vec{K}_g + \vec{K}_p$$

$$= \vec{K}_b - \vec{K}_a + \vec{K}_p. \qquad \text{(III-3)}$$

In these experiments, the probe beam is nearly counter-propagating to one of the write beam characterized by the wavevector $\vec{K}_b$. We therefore have,

$$\vec{K}_p \simeq -\vec{K}_b.$$

And the *Bragg condition* reduces to,

$$\vec{K}_s \simeq -\vec{K}_a, \qquad \text{(III-4)}$$

This means that the signal beam will be nearly counter-propagating to the second write beam.

The *LIG* signal carries all of the information about physical processes influencing the population grating. There exist two different approaches to the *FWM* theory, The first approach[29,30] explicitly considers the nonlinear wave equation where the electric fields are coupled via nonlinear susceptibility of the matter and the sample is considered as an ensemble of two[29], or three[30] level

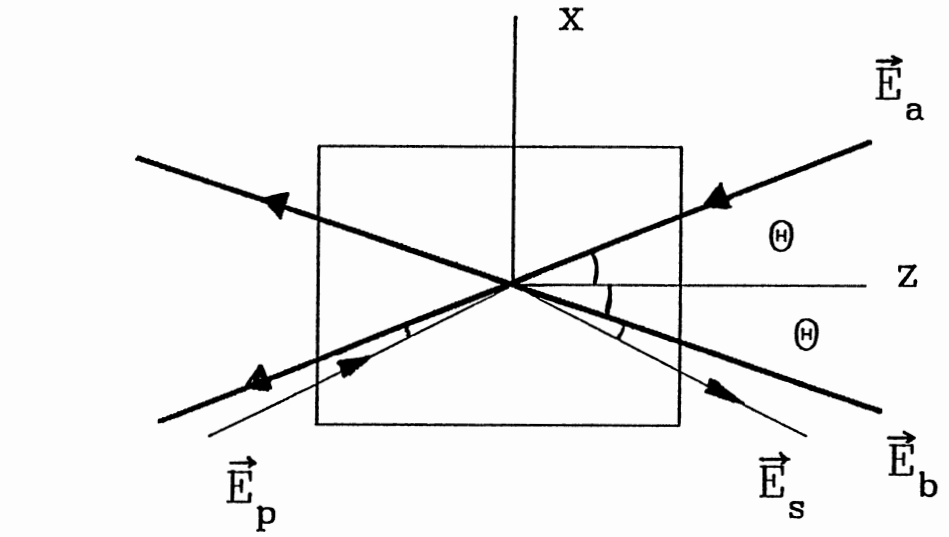

(a)

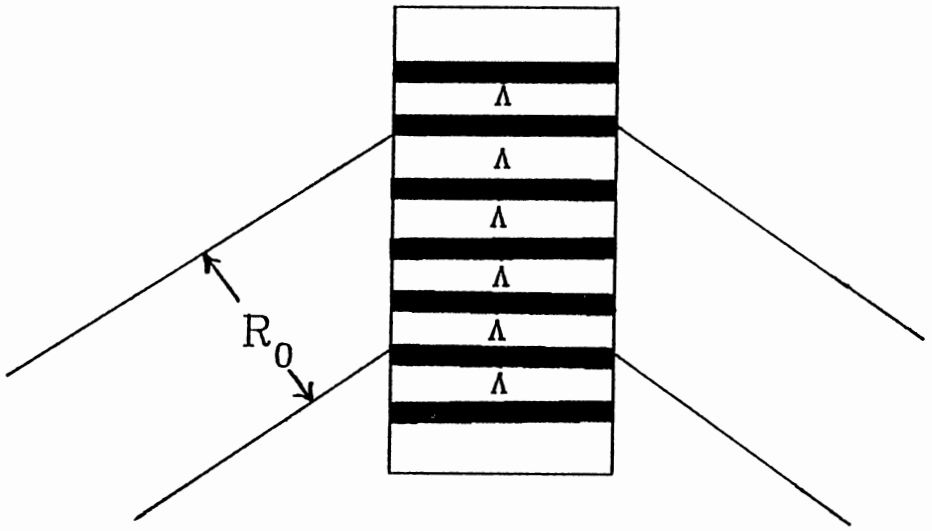

(b)

Figure 14. Pictorial Representation of (a) Four Wave Mixing Configuration and (b) Laser Induced Grating.

systems, whereas the second approach[24,31] considers the Bragg diffraction of the probe beam from the grating. The latter approach assumes a spatially varying susceptibility χ which forms the spatial grating pattern in the material.

The nonlinear wave equation is given by

$$[\nabla^2 + \epsilon\{1/c(\partial/\partial t)\}^2]\vec{E} = -4\pi\{1/c(\partial/\partial t)\}^2\vec{P}^{NL}, \qquad \text{(III-5)}$$

where

$$\vec{P}^{NL} = \chi\vec{E}, \qquad \text{(III-6)}$$

In *FWM* experiments,

$$\vec{E} = \vec{E}_a + \vec{E}_b + \vec{E}_p + \vec{E}_s \qquad \text{(III-7)}$$

where $\vec{E}_a$ and $\vec{E}_b$ are the write beams, $\vec{E}_p$ is the probe beam and $\vec{E}_s$ is the signal beam. We assume plane polarized waves for all the fields such that

$$\vec{E}_a = \vec{E}_{a0}\exp\{-i(\vec{K}_a.\vec{R}-\omega t)\}, \qquad \text{(III-8a)}$$

$$\vec{E}_b = \vec{E}_{b0}\exp\{-i(\vec{K}_b.\vec{R}-\omega t)\}, \qquad \text{(III-8b)}$$

$$\vec{E}_p = \vec{E}_{p0}\exp\{-i(\vec{K}_p.\vec{R}-\omega t)\}, \qquad \text{(III-8c)}$$

$$\vec{E}_s = \vec{E}_{s0}\exp\{-i(\vec{K}_s.\vec{R}-\omega t)\}. \qquad \text{(III-8d)}$$

In these experiments the two write beams, $\vec{E}_a$ and $\vec{E}_b$ have the same intensities, the probe beam $\vec{E}_p$, is much weaker than either of the two write beams and the signal beam $\vec{E}_s$, is even weaker. We can therefore write

$$E = E_0 + \Delta E, \qquad \text{(III-9a)}$$

where $E_0 = |\vec{E}_a + \vec{E}_b|$ and $\Delta E = |\vec{E}_p + \vec{E}_s|$, such that

$$E_0 >> \Delta E. \qquad \text{(III-9b)}$$

The susceptibility of the material is very sensitive to the state and the distribution of ions. Therefore, in the presence of external fields, its value becomes field dependent. If $\chi_g^{(1)}$ is the susceptibility of the system with all the ions in ground state, then in the presence of external fields, its value is given by

$$\chi = \chi_g^{(1)} + \{\chi_m^{(1)} - \chi_g^{(1)}\}(N_m/N) + \chi_g^{(3)} E_1 E_2^* \ldots, \qquad \text{(III-10)}$$

where N is total number of ions in the sample, N_m is population of the metastable state, E_i are the external fields and $\chi_m^{(1)}$ is susceptibility of the sample if all the atoms were in metastable state. The grating is created due to change in the population of the metastable state versus the ground state, and the corresponding contributions to susceptibility are given by the second term of Eq. (III-10).

In order to calculate the quantity $\{\chi_m^{(1)} - \chi_g^{(1)}\}N_m/N$, we assume a model for the active ions. Lawson et al.[32] using a two level system model has developed an expression for the susceptibility as

$$\chi = -(2\alpha_0/k)\{(i+\delta)/[1+\delta^2+|E|^2/|E_s|^2]\}, \qquad \text{(III-11)}$$

where

$$|E_s|^2 = \hbar^2/(T_1 T_2 \mu^2), \qquad \text{(III-12)}$$

and we can identify $\alpha_0 = \mu^2 \Delta N^e T_2 k/(2\epsilon_0 \hbar)$ as the small signal field attenuation coefficient, $\delta=(\omega-\omega_{12})T_2$ as the normalized detuning from the line center, ω as the write beam frequency, ω_{12} as the transition frequency between level 1 and level 2, μ as the dipole moment, ΔN^e as the equilibrium population difference between the two levels and T_1 and T_2 as the longitudinal and transverse relaxation times respectively. Using this definition of susceptibility, the behavior of the sample can be described by a set of four coupled differential equations.[1] These coupled differential equations were solved numerically treating real and imaginary parts of the coupling coefficients D_1 and D_2, as defined in Eq. (III-13) and Eq. (III-14) below, as adjustable parameters.

$$D_1 = D_1^r + iD_1^i = 2\pi\mu L(\kappa-\xi) \qquad \text{(III-13)}$$

$$D_2 = D_2^r + iD_2^i = \pi\mu\Delta\kappa L \qquad \text{(III-14)}$$

where L is the distance of the overlap region, κ is a parameter related to the complex index of refraction, and $\Delta\kappa$ is the laser induced modulation in κ. This can be separated into a modulation of the refractive index - Δn, and a modulation of the absorption coefficient - $\Delta\alpha$. These parameters are related to the coupling coefficients D_1^r, D_1^i, D_2^r, and D_2^i as

$$\Delta\alpha = -2\bar{\alpha}(D_2^i/D_1^i), \qquad \text{(III-15)}$$

$$\Delta n = (\bar{\alpha}c/\omega_0)D_2^r/D_1^i, \qquad \text{(III-16)}$$

where $\bar{\alpha}$ is the average absorption coefficient at the write beam wavelength and c is the speed of light. T_2-dephasing time can be calculated in terms of Δn, $\Delta\alpha$, ω_0, and ω_{12} as

$$T_2 = (2\omega_0/c)(\Delta n/\Delta\alpha)(\omega_0-\omega_{21})^{-1} \qquad \text{(III-17)}$$

The set of coupled differential equations can be solved for special cases. To see the effect of the crossing angle θ on the scattering efficiency, we consider one special case where,

$$(D_2^i)^2 + (D_2^r)^2 - (D_1^i + D_2^i)^2 \quad > \quad 0 \qquad \text{(III-18)}$$

and

$$D_1^r - D_2^r \neq \begin{cases} 0 \\ \\ [(D_2^r)^2+(D_2^r)^2 - (D_1^i-D_2^i)^2]^{1/2} \end{cases} \qquad \text{(III-19)}$$

The scattering efficiency is then given by,

$$\eta(\theta) = 2[(D_2^i)^2+(D_2^r)^2][(D_2^i)^2+(D_2^r)^2-(D_1^i+D_2^i)^2]^{-1}$$
$$\sin^2\{k[(D_2^r)^2+(D_2^r)^2-(D_1^i+D_2^i)^2]^{1/2}\ln[\tan(\theta/2)]\}. \qquad \text{(III-20)}$$

The crossing angle θ in the above expression is directly related to the overlap of the laser beams which in turn determines the modulation in complex index of refraction. The D parameters are found numerically by fitting the experimental data for the scattering efficiency η as a function of θ to Eq. (III-20).

The two level model is a reasonable approximation for the systems like atomic vapors or the photorefractive materials where two states can adequately describe the system, however for a sample containing active ions in solids, we need a model which treats ions as multilevel systems. The willingness of physicists to accept the less rigorous two level system model underscores the difficulties encountered in developing a multilevel system model. Such a model has recently been proposed by Powell et al,[33] which assumes the sample to be made up of an ensemble of effective four level systems as shown in Fig. 15. The ions are resonantly pumped from the ground state $|g\rangle$ into an intermediate state $|a\rangle$, from where they quickly relax to the metastable state $|m\rangle$. The long-lived metastable state can interact with the ground state or to the continuum of higher levels represented by $|b\rangle$. However for simplicity, these levels are assumed to be so short lived, that they almost instantaneously decay to the metastable state. Therefore for all practical purposes,

$$N = N_m + N_g. \qquad \text{(III-21)}$$

where N_m and N_g are the number of ions in the metastable state and the ground state respectively.

In case of thin samples, the intensity of *FWM* signal beam can be given by[22,23]

$$I_s = (\pi TL/2n\lambda)^2 |\Delta\chi|^2 I_p \exp(-a_p L \sec\theta), \qquad \text{(III-22)}$$

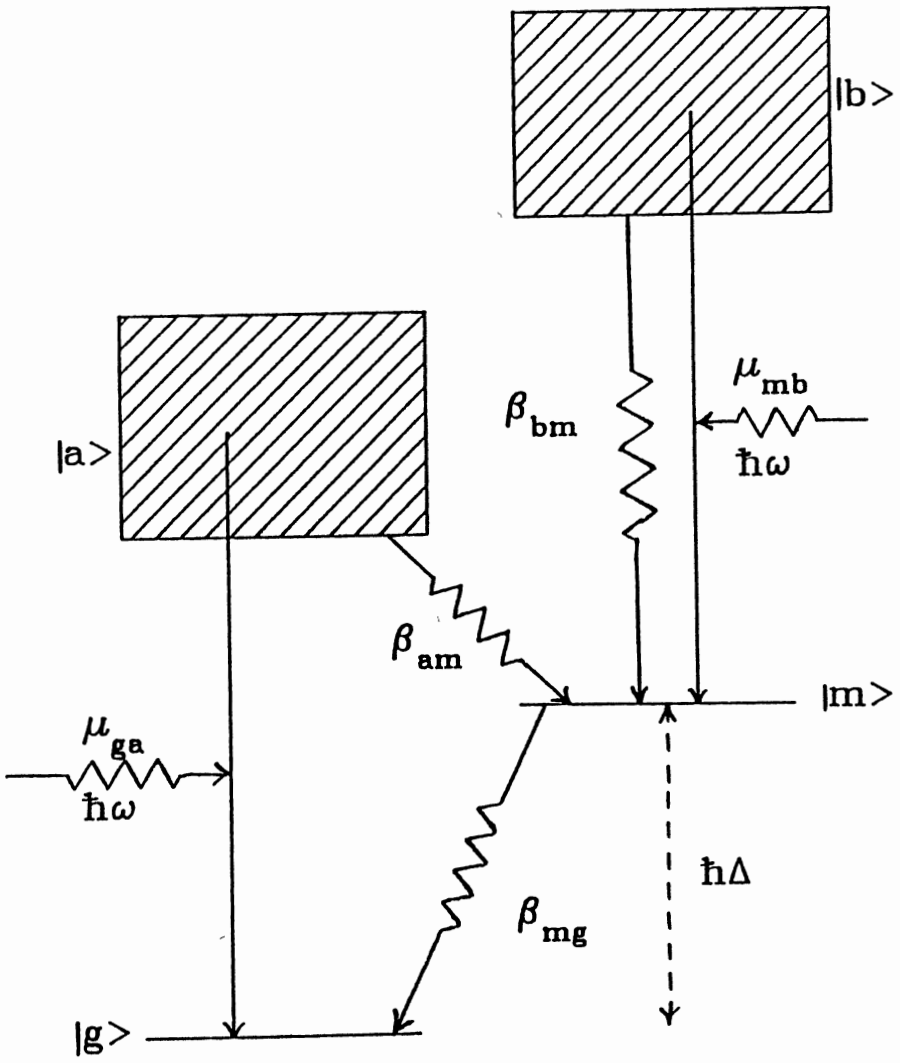

Figure 15. Four Level System Model. |g>, |m>, |a>, and |b> are the Ground, Metastable, Intermediate and Charge Transfer States of the System Respectively.

where I_p is the intensity of the probe beam, a_p is the absorption coefficient at the probe beam wavelength, T is correction for sample surface reflectivity, and $\Delta\chi$ is the laser induced change in susceptibility at the wavelength λ. Since $\Delta\chi$ is a complex quantity, the *LIG* has two components. The one due to the real part of $\Delta\chi$ is called the phase grating and the other component which is due to the imaginary part of $\Delta\chi$ is referred to as the amplitude grating. Using the effective four level system model, the mathematical expressions for the scattering efficiency of both of these parts have been developed in Ref. 33 for the case of a specific small value of the write beam crossing angle. However, the spatial profile of the metastable state population as well as the write beam overlap depends upon the crossing angle. We have therefore, extended the above model to include the effects of the dependence on the crossing angle. Figure 14 shows the experimental arrangement as it pertains to our system. The four laser beams are given by Eq. (III-8), where the propagation direction is assumed to be along the z-axis. In cylindrical coordinates, the vectors $\vec{K}$ and $\vec{R}$ can be written as,

$$\vec{R} = r\,\hat{r} + z\,\hat{z}, \qquad \text{(III-23a)}$$

$$\vec{K} = K_r\,\hat{r} + K_z\,\hat{z}, \qquad \text{(III-23b)}$$

and

$$|\vec{K}_a| = |\vec{K}_b| = k_1 + ia_w/2$$

$$|\vec{K}_p| = |\vec{K}_s| = k_3 + ia_p/2.$$

Therefore,

$$\vec{K}_a.\vec{R} - \vec{K}_b.\vec{R} = 2k_1 r\sin\theta + ia_w z\cos\theta. \qquad \text{(III-24)}$$

$$|E_{a0}|^2 = I_a,$$

$$|E_{b0}|^2 = I_b,$$

The pump rate W can be written as,

$$W = \{Im(\chi_{12})\sqrt{I_a I_b}/(16\pi N\hbar L)\}[1-\exp(-a_p L\sec\theta)] \times \cos(\theta)\cos\{2k_1 r\sin(\theta/2)\}. \qquad \text{(III-25)}$$

The polarization of the system is defined as,

$$P = (1/4\pi)\chi E.$$

Also,

$$P = N\ Tr(\mu\rho).$$

Therefore, for our system,

$$\chi = (4\pi N/E)\{\mu_{ga}\rho_{ag} + \mu_{ag}\rho_{ga} + \mu_{mb}\rho_{bm} + \mu_{bm}\rho_{mb}\}. \qquad \text{(III-26)}$$

Where μ_{ij} and ρ_{ij} are respectively the ij^{th} components of the dipole moment and the density matrix. In order to evaluate the density matrix elements ρ_{ij}, we use the Liouvill-Schrodinger equation.[34,35]

$$i\hbar d\rho/dt = [H,\rho] + i\hbar(d\rho/dt)_{decay}. \qquad \text{(III-27)}$$

In this equation the total hamiltonian H is given by

$$H = H_0 - H', \tag{III-28}$$

where H_0 is the diagonal part of hamiltonian with its diagonal elements equal to the ground state energies of the respective levels and H' is the interaction whose matrix elements between the states $|i\rangle$ and $|j\rangle$ are given by

$$H'_{ij} = -\mu_{ij}E. \tag{III-29}$$

Therefore,

$$H = \begin{bmatrix} \epsilon_g & H'_{ga} & 0 & 0 \\ H'_{ag} & \epsilon_a & 0 & 0 \\ 0 & 0 & \epsilon_m & H'_{mb} \\ 0 & 0 & H'_{bm} & \epsilon_b \end{bmatrix} \tag{III-30}$$

With the assumptions that the decay rate β_{mg} is much smaller than β_{ba}, β_{ma}, and β_{mb}, we can write down the rate equations as follows,

$$i\hbar d\rho_{gg}/dt = H'_{ga}\rho_{ag} - \rho_{ga}H'_{ag} + i\hbar\beta_{mg}\rho_{mm} , \tag{III-31a}$$

$$i\hbar d\rho_{ga}/dt = -H'_{ga}\rho_{gg} - \rho_{ga}\{\epsilon_a - \epsilon_g\} - i\hbar\rho_{ga}T_{2a}^{-1} , \tag{III-31b}$$

$$i\hbar d\rho_{mb}/dt = -\rho_{mb}\{\epsilon_b - \epsilon_m\} - H'_{mb}\rho_{mm} - i\hbar\rho_{mb}T_{2b}^{-1} , \tag{III-31c}$$

$$i\hbar d\rho_{mm}/dt = -\rho_{mb}\{\epsilon_b - \epsilon_m\} - H'_{mb}\rho_{mm} - i\hbar\beta_{mg}\rho_{mm} . \tag{III-31d}$$

These coupled differential equations can be solved simultaneously as follows:

Define the transition frequencies ω_{ga} and ω_{mb} as

$$\epsilon_a - \epsilon_g = \hbar\omega_{ga}, \qquad \text{(III-32a)}$$

$$\epsilon_b - \epsilon_m = \hbar\omega_{mb}. \qquad \text{(III-32b)}$$

At equilibrium $d\rho_{ij}/dt = 0$. We therefore define a slowly varying variable γ_{ij} such that:

$$\rho_{ij}(t) = \gamma_{ij}(t)\exp(i\omega_0 t), \qquad \text{(III-33)}$$

where ω_0 is the excitation frequency. The corresponding solution is:

$$\rho_{ga}=-\mu_{ga}E\{[(\omega_{ga}-\omega_0)-iT_{2a}^{-1}]/\hbar[(\omega_{ga}-\omega_0)^2+T_{2a}^{-2}]\}\rho_{gg} \qquad \text{(III-34)}$$

$$\rho_{ag}=-\mu_{ga}E\{[(\omega_{ga}+\omega_0)+iT_{2a}^{-1}]/\hbar[(\omega_{ga}-\omega_0)^2+T_{2a}^{-2}]\}\rho_{gg} \qquad \text{(III-35)}$$

$$\rho_{mb}=-\mu_{mb}E\{[(\omega_{mb}-\omega_0)-iT_{2b}^{-1}]/\hbar[(\omega_{mb}-\omega_0)^2+T_{2b}^{-2}]\}\rho_{mm} \qquad \text{(III-36)}$$

$$\rho_{bm}=-\mu_{mb}E\{[(\omega_{mb}+\omega_0)+iT_{2b}^{-1}]/\hbar[(\omega_{mb}-\omega_0)^2+T_{2b}^{-2}]\}\rho_{mm} \qquad \text{(III-37)}$$

The rate of change of the population of metastable state is given by

$$dN_m/dt = N_g W - \beta_{mg} N_m.$$

At steady state,

$$N_g W - \beta_{mg} N_m = 0.$$

But $N_g = N - N_m$, therefore,

$$N_m(W + \beta_{mg}) = NW$$

$$\rho_{mm} = N_m/N$$

$$= W/(W + \beta_{mg}). \qquad \text{(III-38)}$$

Similarly,

$$\rho_{gg} = 1 - \{W/(W + \beta_{mg})\}. \qquad \text{(III-39)}$$

For pumping much below saturation, $W << \beta_{mg}$ and Eq. (III-38) simplifies to,

$$\rho_{mm} \simeq W/\beta_{mg}. \qquad \text{(III-38')}$$

Therefore,

$$\rho_{gg} \simeq 1 \qquad \text{(III-39')}$$

Using Eq. (III-34) - Eq. (III-39'), the susceptibility of the material can be written as

$$\chi = 4\pi N/\hbar$$

$$*\{|\mu_{ga}|^2[1-W/(W-\beta_{mg})]([(\omega_{ga}-\omega_0)-iT_{2a}^{-1}]/[(\omega_{ga}-\omega_0)^2+T_{2a}^{-2}]$$

$$- [(\omega_{ga}+\omega_0)+iT_{2a}^{-1}]/[(\omega_{ga}-\omega_0)^2+T_{2a}^{-2}])$$

$$|\mu_{mb}|^2[W/(W-\beta_{mg})]([(\omega_{mb}-\omega_0)-iT_{2b}^{-1}]/[(\omega_{mb}-\omega_0)^2+T_{2b}^{-2}]$$

$$- [(\omega_{mb}+\omega_0)+iT_{2b}^{-1}]/[(\omega_{mg}-\omega_0)^2+T_{2b}^{-2}])). \qquad \text{(III-40)}$$

We can use this expression to calculate the values $\chi_g^{(1)}$ and $\chi_m^{(1)}$ for the material using the fact that in the valley region, the ions are in ground state where $W = 0$, and in the peak region of the grating the ions are in the metastable state where the pump rate is given by Eq. (III-23). Therefore, in the low excitation limit, $\Delta\chi$ can be written as.

$$\Delta\chi=4\pi NW/\hbar\beta_{mg}\{|\mu_{ga}|^2([(\omega_{ga}-\omega_0)-iT_{2a}^{-1}]/[(\omega_{ga}-\omega_0)^2+T_{2a}^{-2}]$$
$$-[(\omega_{ga}+\omega_0)+iT_{2a}^{-1}]/\hbar[(\omega_{ga}-\omega_0)^2+T_{2a}^{-2}])$$
$$|\mu_{mb}|^2([(\omega_{mb}-\omega_0)-iT_{2b}^{-1}]/\hbar[(\omega_{mb}-\omega_0)^2+T_{2b}^{-2}]$$
$$-[(\omega_{mb}+\omega_0)+iT_{2b}^{-1}]/\hbar[(\omega_{mg}-\omega_0)^2+T_{2b}^{-2}])\}. \qquad \text{(III-41)}$$

This result can be simplified by noting that far from resonance, $(\omega_{ga}-\omega_0) >> T_{2a}^{-1}$, and $(\omega_{mb}-\omega_0) >> T_{2b}^{-1}$, and always $(\omega_{ga}+\omega_0) >> T_{2a}^{-1}$, and $(\omega_{ga}+\omega_0) >> T_{2b}^{-1}$. Eq. (III-41) can now be written as

$$\Delta\chi=2\pi NW/\hbar\beta_{mg}[\{2\omega_{mb}|\mu_{mb}|^2/(\omega_{mb}^2-\omega_0^2)-2\omega_{ga}|\mu_{ga}|^2/(\omega_{mb}^2-\omega_0^2)\}$$
$$+i\{|\mu_{mb}|^2T_{2b}^{-1}/((\omega_{mb}-\omega_0)^2+T_{2b}^{-2})$$
$$-|\mu_{ga}|^2T_{2a}^{-1}/((\omega_{mb}-\omega_0)^2+T_{2a}^{-2})\}]. \qquad \text{(III-42)}$$

These results can be written in terms of more easily recognizable parameters such as the laser induced changes in polarizability $\Delta\alpha_p$ and the absorption cross section $\Delta\sigma$ of the material as,

$$|\Delta\chi|^2 = (2\pi NWf_L^2\beta_{mg})^2\{(\Delta\alpha_p)^2+(n\lambda/8\pi^2f_L)^2(\Delta\sigma)^2\} \qquad \text{(III-43)}$$

Using Eq. (III-25) and Eq. (III-43) in Eq. (III-22), the intensity of the scattered beam can now be written as

$$I_s=(\tau_m[\pi Tf_L]^2L/16hc)^2\{(\Delta\alpha_p)^2+(n\lambda/8\pi^2f_L^2\Delta\sigma)^2\}\exp(-a_wL\sec\theta)$$
$$*I_aI_bI_p[1-\exp(-a_pL\sec\{\theta/2\})]^2\sin^2(\theta/2)\cos^2(2k_1L\sin\theta). \qquad \text{(III-44)}$$

We now assume the gaussian profiles of radius ρ_0 $\{I = I_0\exp(-2r^2/\rho_0^2)\}$ for all the beams and integrate over the cross-sectional area of the beam to get the power. The scattering efficiency of the *LIG* signal can then be written as

$$\eta=(\tau_m[\pi Tf_L]^2L/16hc)^2\{(\Delta\alpha_p)^2+(n\lambda/8\pi^2f_L\Delta\sigma)^2\}\exp(-a_wL\sec\theta)$$
$$*P_aP_b[1-\exp(-a_pL\sec\theta)]^2Z^2\int_0^1 dt(1-t)^{-3/2}\exp(-2t/3Z) \quad \text{(III-45)}$$

where $Z = \pi\rho_0/\Lambda$. In our experiments, both the write beams had the same power, therefore in the low excitation limit,

$$\eta \propto P^2 \quad \text{(III-46)}$$

This is the same result as obtained using the two level system approximation. We therefore conclude that, well below saturation pumping levels ($W << \beta_{mg}$), the two level system model is a reasonable approximation. It is this assumption that gives us confidence to use the results derived with the two level system approximation for some of the analysis in *chapter IV*.

Optical Dephasing

The expression for the T_2-dephasing time is given by[35]

$$1/T_2 = 1/2T_1 + 1/T_2^{PD} \quad \text{(III-47)}$$

where T_1 is the relaxation time of the excited level and T_2^{PD} is the time associated with the scattering mechanisms.

The nonradiative decay rate is given by time dependent

perturbation theory as[36]

$$K_{nr} = (4\pi^2/h)|\langle\Psi_{ev}|\Delta H|\Psi_{e'v'}\rangle|^2\rho(E_f), \qquad \text{(III-48)}$$

where the primed coordinates denote the initial state of the system and the unprimed coordinates denote the final state of the system, $\rho(E_f)$ is the density of final states, and the interaction hamiltonian ΔH is given by,

$$\Delta H = qV_{ep} + H_{s.o}, \qquad \text{(III-49)}$$

where V_{ep} is electron-phonon coupling term, q is configurational coordinate and $H_{s.o}$ is the spin-orbit hamiltonian. The wavefunction $\Psi_{ev}(r,q)$ is defined in Born-Oppenheimer approximation as

$$\Psi_{ev}(r,q) = \psi_e(r,q)\chi_v(q), \qquad \text{(III-50)}$$

where $\psi_e(r,q)$ is the electronic part and $\chi_v(q)$ is the vibrational part of wavefunction. The exact form of vibrational wave function depends upon the nature of the interaction assumed. In an attempt to determine whether or not the anharmonic effects are needed to explain the observed sample to sample variation in T_2-dephasing time, the decay rates have been calculated from an excited vibrational level of $^4T_2$ band to the bottom of the ^2E level, using a purely harmonic vibrational potential and the anharmonic Morse potential. The anharmonic potential well corresponding to each electronic level is defined by the Morse potential given by,[37]

$$U(q) = D_0\{1-\exp[-a'(q-q_0)]\}^2 \qquad \text{(III-51)}$$

where D_0 is the dissociation energy, q is the configurational coordinate, q_0 is the equilibrium value of q, and a' is the anharmonicity constant.

An alternate model for describing $^4T_2$ to ^2E radiationless relaxation has been proposed by Donnelly et al.[38] In this model, the wavefunctions of the ^2E and $^4T_2$ levels are coupled via the spin orbit interaction. The unperturbed wave functions of ^2E and $^4T_2$ level are given by,

$$|^2E,\gamma_n\rangle = |^2E\rangle|\gamma_n\rangle, \qquad \text{(III-52)}$$

$$|^4T_2,\beta_l\rangle = |^4T_2\rangle|\beta_l\rangle, \qquad \text{(III-53)}$$

where $|^2E\rangle$ and $|^4T_2\rangle$ are the electronic wave functions, $|\gamma_n\rangle$ and $|\beta_l\rangle$ are the vibrational wave functions, and n and l are the vibrational quantum numbers of ^2E and $^4T_2$ levels respectively. The spin-orbit interaction $H_{s.o.}$, mixes ^2E and $^4T_2$ levels and the perturbed wave functions of these two states can be written as[38]

$$\Psi(^2E,\gamma_n) = \{|^2E,\gamma_n\rangle+\Sigma_\nu S(\beta_m,\gamma_n)|^4T_2,\beta_\nu\rangle\}/\{\sqrt{1+\Sigma_\nu S^2(\beta_\nu,\gamma_n)}\}, \qquad \text{(III-54)}$$

and

$$\Psi(^4T_2,\beta_l) = \{|^4T_2,\beta_l\rangle+\Sigma_\mu S(\gamma_\mu,\beta_l)|^2E,\gamma_\mu\rangle\}/\{\sqrt{1+\Sigma_\mu S^2(\gamma_\mu,\beta_l)}\}, \qquad \text{(III-55)}$$

where

$$S(\beta_\nu,\gamma_n)=-H\langle\beta_\nu|\gamma_n\rangle SGN(E_{\nu n})/\{\sqrt{H^2\langle\beta_\nu|\gamma_n\rangle^2+(E_{\nu n}/2)^2}+|E_{\nu n}/2|\}, \qquad \text{(III-56)}$$

$$S(\gamma_\mu,\beta_1)=-H\langle\gamma_\mu|\beta_1\rangle SGN(E_{\mu 1})/\{\sqrt{H^2\langle\gamma_\mu|\beta_1\rangle^2+(E_{\mu 1}/2)^2}+|E_{\mu 1}/2|\}, \quad \text{(III-57)}$$

and

$$E_{\nu n} = \Delta E + (\beta_\nu-\gamma_n)\hbar\omega. \quad \text{(III-58)}$$

Here H is the value of the matrix element of the spin orbit interaction $H_{s.o.}$, between ^2E and $^4T_2$ electronic states, ΔE is the crystal field splitting between ^2E and $^4T_2$ levels, and $SGN(E_{\nu n})$ is +1 for positive $E_{\nu n}$ and -1 for negative $E_{\nu n}$. An expression similar to Eq. (III-58) can be obtained for $E_{\mu 1}$.

The vibrational potential in this model is assumed to be purely harmonic with the corresponding vibrational wave function given by,

$$|\gamma_\mu(\xi)\rangle = N_\mu H_\mu(\xi)\exp(-\xi^2/2), \quad \text{(III-59)}$$

where

$$\xi = \sqrt{(M\omega/\hbar)\{q-q_0{}^e\}}, \quad \text{(III-60)}$$

$$N_\mu = 1/\sqrt{(2^\mu m!\sqrt{\pi})}, \quad \text{(III-61)}$$

and $H_\mu(\xi)$ is the μth order Hermite polynomial defined as,

$$H_\mu(\xi) = \sum_{s=0}^{\mu/2} (-1)^s(2\xi)^{\mu-2s}\mu!/\{(\mu-2s)!s!\}. \quad \text{(III-62)}$$

The vibrational wave functions $|\beta_\nu(\eta)\rangle$ can be defined in an analogous fashion.

Energy Transfer

The peak regions of the grating contain ions ın their excited state which, being unstable, will eventually decay to the stable ground state by losing the excitation. This can happen either radiatively by emitting a photon or it may interact with the phonon or other active ions in the crystal and transfer its energy nonradiatively. The latter process depends upon the interaction of excited ion with other active ions or upon its interaction with the lattice. The corresponding effects are characterized by the nearest neighbor ion-ion interaction rate V and the exciton-phonon scattering rate α.

As noticed earlier, the *FWM* scattering efficiency is very sensitive to the population of metastable state and therefore any process that takes away the excitation from he metastable state will affect the scattering efficiency of the *FWM* signal. The decay of the transient signal is therefore shortened by energy migration from the peak to the valley region of the grating. Equation (III-2) shows that as the crossing angle of the write beams increases, the grating spacing decreases and the effects of the energy transfer are enhanced. Therefore, by measuring the change in the grating decay rate as a function of the crossing angle, we can measure the long-range energy migration.

A theoretical model for the *FWM* signal decay has been developed by Kenkre et al.[39,40], which relates the exciton-phonon scattering rate and the ion-ion interaction rate to

the intensity of the *FWM* signal beam. Since the basic assumptions used in the development of this model are consistent with the conditions of our experiments, we can use this theory to measure the energy migration parameters in our samples.

According to this theory, the exponential decay of normalized transient grating signal in the presence of excitation migration can be described as

$$I_t(t) = \exp(-2t/\tau_f)\ \{J_0(bt)\exp(-\alpha t) + \tau_f \int_0^t du\ \exp[-\alpha(t-u)]J_0(b\sqrt{t^2-u^2})\}^2. \qquad \text{(III-65)}$$

Here τ_f is the fluorescence lifetime, J_o is the Bessel function of zero order, and the parameter b is defined as,

$$b = 4V\sin\{(2\pi a_0/\lambda)\sin(\theta/2)\}. \qquad \text{(III-66)}$$

Where the average active ion separation a_0, can be determined by the active ion concentration n_d according to the following expression.

$$a_0 = (3/4\pi n_d)^{1/3}. \qquad \text{(III-67)}$$

The exciton dynamics can be characterized by these parameters in terms of the diffusion coefficient D, the diffusion length L_d, the mean free path L_m, and the number of sites visited between successive scattering events N_s. These parameters are given by,

$$D = 2(Va_0)^2/\alpha, \qquad \text{(III-68)}$$

$$L_d = \sqrt{2D\tau_f}, \tag{III-69}$$

$$L_m = \sqrt{2}Va_0/\alpha \tag{III-70}$$

$$N_s = L_m/a_0 \tag{III-71}$$

respectively.

CHAPTER IV

DATA ANALYSIS AND DISCUSSION

Four-Wave Mixing

In this chapter, the experimental data obtained on all three samples used in these studies are analyzed. Four-Wave Mixing signal efficiencies, their power dependence, optical dephasing of the pump level to the metastable state, and decay of the population grating are investigated. Theoretical models discussed in *chapter III* are used to analyze the data and extract useful information on the microscopic parameters for optical dephasing phenomenon and spatial energy migration among the dopant ions. The results are compared to similar studies in other laser crystals. The *FWM* spectroscopy is used to study spatial energy migration whereas the total non-radiative energy transfer from initially excited Cr^{3+} ions to Nd^{3+} ions in the codoped sample is measured using the fluorescence lifetime quenching techniques.

Power dependence of the FWM signal

In *FWM* experiments, the interaction of laser beams with the material, changes its complex refractive index by an amount Δn and the grating induced inside the sample

reflects this change. In order to study the properties associated with the grating, the diffracted signal beam was analyzed.

The gratings of the excited Cr^{3+} ions in Cr:GGGM and Cr,Nd:GGGM samples were created by pumping into the $^4T_1$ band and the $^4T_2$ band using 488 nm line from an argon ion laser and 590 nm line of *Rhodamine-6G* dye from an argon ion laser-pumped ring dye laser respectively. An excited state population grating is observed after radiationless relaxation processes establish an equilibrium population in ^2E or $^4T_2$ level. The 514.5 nm line from argon ion laser was used to create an excited state population grating of the Nd^{3+} ions in Nd:GGGM. The scattering efficiency of the *FWM* signal for the population grating in a sample described by an effective four level system model is given by *Equation (III-45)*.

The diffracted *FWM* signal beam carries all the information about laser induced grating. The power, the wavelength and the crossing angle of the write beams affect the magnitude of *FWM* scattering efficiency. The changes in scattering efficiency as a result of variation of the above parameters are studied for all three samples. In all three samples, the *FWM* signal was found to comprise of a transient and a permanent part. When both of the write beams were blocked, the transient part of the signal decayed with a decay rate approximately equal to twice the fluorescence decay rate of the corresponding optically

active ions. This indicates that the transient part of *FWM* signal is due to excited state population grating. The small permanent signal indicates the presence of long lived changes in the sample due to other physical processes such as charge re-location or the creation of color centers. To erase the permanent grating, the sample was exposed to a single erase beam. Since the same behavior was observed in all three samples, we only show the results for Cr:GGGM in *Fig. 16*. In this figure, the intensity of *FWM* signal is plotted as a function of time and it is observed that when both the write beams are blocked at time $t = 0$, the *FWM* signal decays very rapidly to only a fraction (*12%*) of the initial value in a time interval approximately equal to one half of the fluorescence lifetime of metastable state of the Cr^{3+} ions. To erase the permanent grating, a single write beam was turned on at $t = 4$ *min*. Similar persistent *FWM* signals have also been observed in other garnet samples[3], where it was suggested that the origin of permanent part of the *LIG* may be associated with the presence of color centers. Pardavi-Horwath and Osvay[41] have reported that the doping of Ca^{2+} ions in the GGG crystals creates color centers, vacancies, and site changes of dopant ions. The permanent gratings observed in our samples are consistent with the above conclusions. However it is important to note that the presence of the permanent signal had no effect on the interpretation of fast transient signal. The characteristics of the signal beam associated

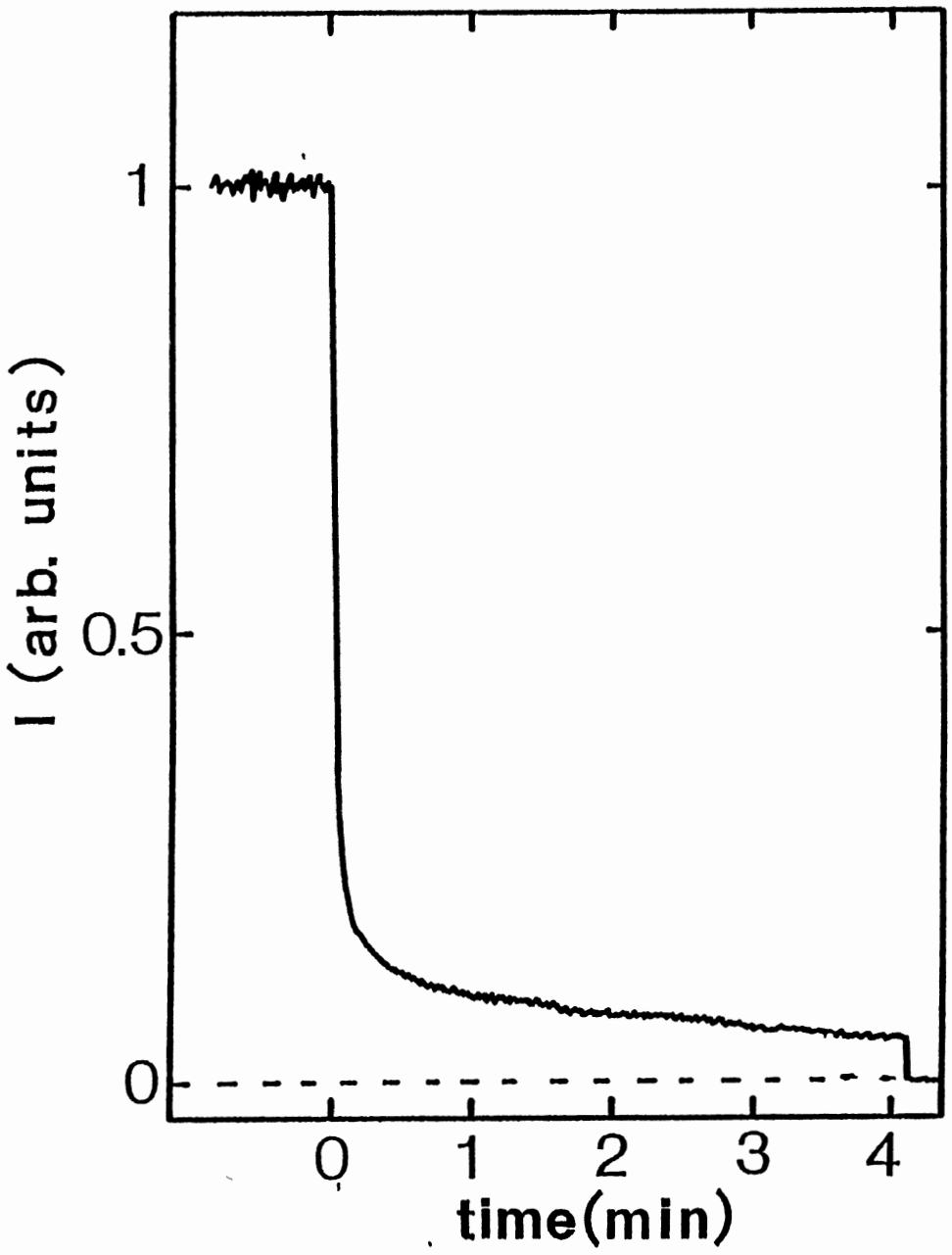

Figure 16. FWM Signal Decay After Both the Write Beams are Turned off at t = 0 Min., and After an Erase Beam is Turned on at t = 4 Min.

with the population grating are discussed in the following.

We have measured the scattering efficiency as a function of the write beam powers for both permanent as well as transient gratings in all three samples. *Figure 17* shows the results for the power dependence of *FWM* scattering efficiency in Cr:GGGM sample. The permanent grating (solid circles) appears to be independent of the write beam powers which can be explained easily if the concentration of color centers creating the permanent grating is such that even with very low powers, we can probe all of the centers and any further increase in power does not bring about any change. The transient grating (triangles) varies quadratically with the write beam power, saturates for intermediate powers, and then rises again for higher powers. The saturation effects observed at higher powers, may be due to saturating the absorption transition as expected in an effective four level system model or it may be due to higher order non-linear optical effects. The quadratic power dependence of the scattering efficiency at low write beam powers, is consistent with the predictions of *Eq. (III-45)* for the behavior of this type of grating.[1] The behavior at higher laser power indicates the onset of additional nonlinear optical processes. In the discussion following *Eq. (III-45)*, it was noted that in the low excitation limit, the results of the effective four level model are reduced to the more simpler two level model. In order to ensure the validity of the results obtained for

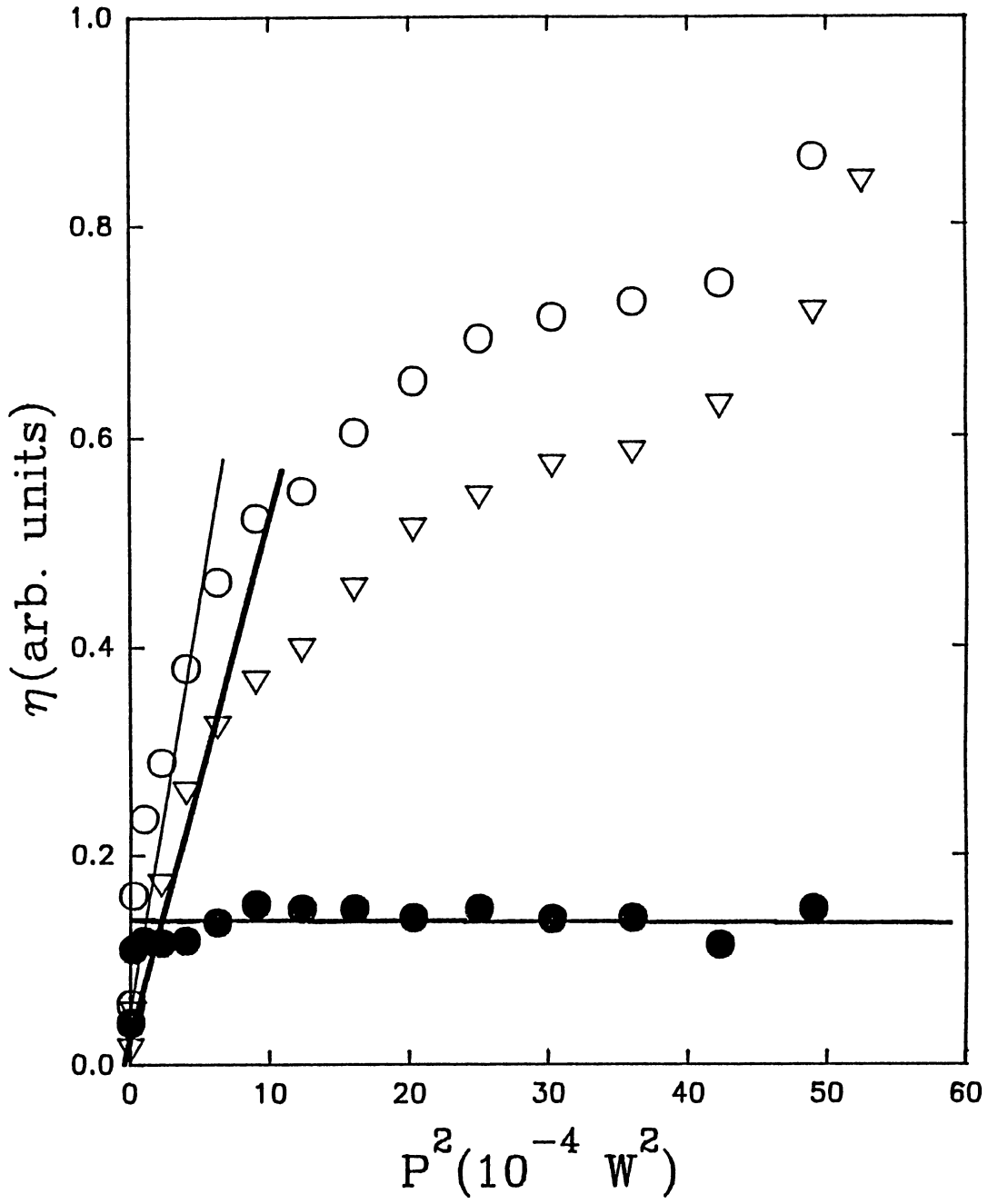

Figure 17. FWM Scattering Efficiency as a Function of Write Beam Power for Permanent (Solid Circles), Transient (Hollow Triangles), and Total (Hollow Circles) FWM Signal in Cr:GGGM.

energy migration in our samples using the two level system approximation, the write beam powers were kept low enough such that the system was well below saturation. Similar results on power dependence obtained for Nd:GGGM and Cr,Nd:GGGM samples, are plotted in *Fig. 18* and *Fig. 19* respectively.

Energy Transfer

The *FWM* signal decay of a population grating is governed by fluorescence lifetime of the excited state as well as any of the other processes affecting the excited state population distribution. The excitation energy migration among the optically active ions can strongly influence the spatial distribution of the excited ions. The *FWM* signal decay is thus shortened by migration of the excitation from peak to the valley region of the grating, and this effect is very sensitive to the distribution of the optically active ions and the grating spacing. Therefore, in the presence of spatial energy migration, the grating decay rates are expected to increase with the decreasing grating spacings, and thus a study of the variation in the grating decay rates as a function of the grating spacings should provide us information about the strength of spatial energy migration. In this section, the decay of *FWM* signal will be analyzed using the model of Kenkre et al.[39-40], discussed in *chapter III*, to extract the values of energy transfer parameters for our samples.

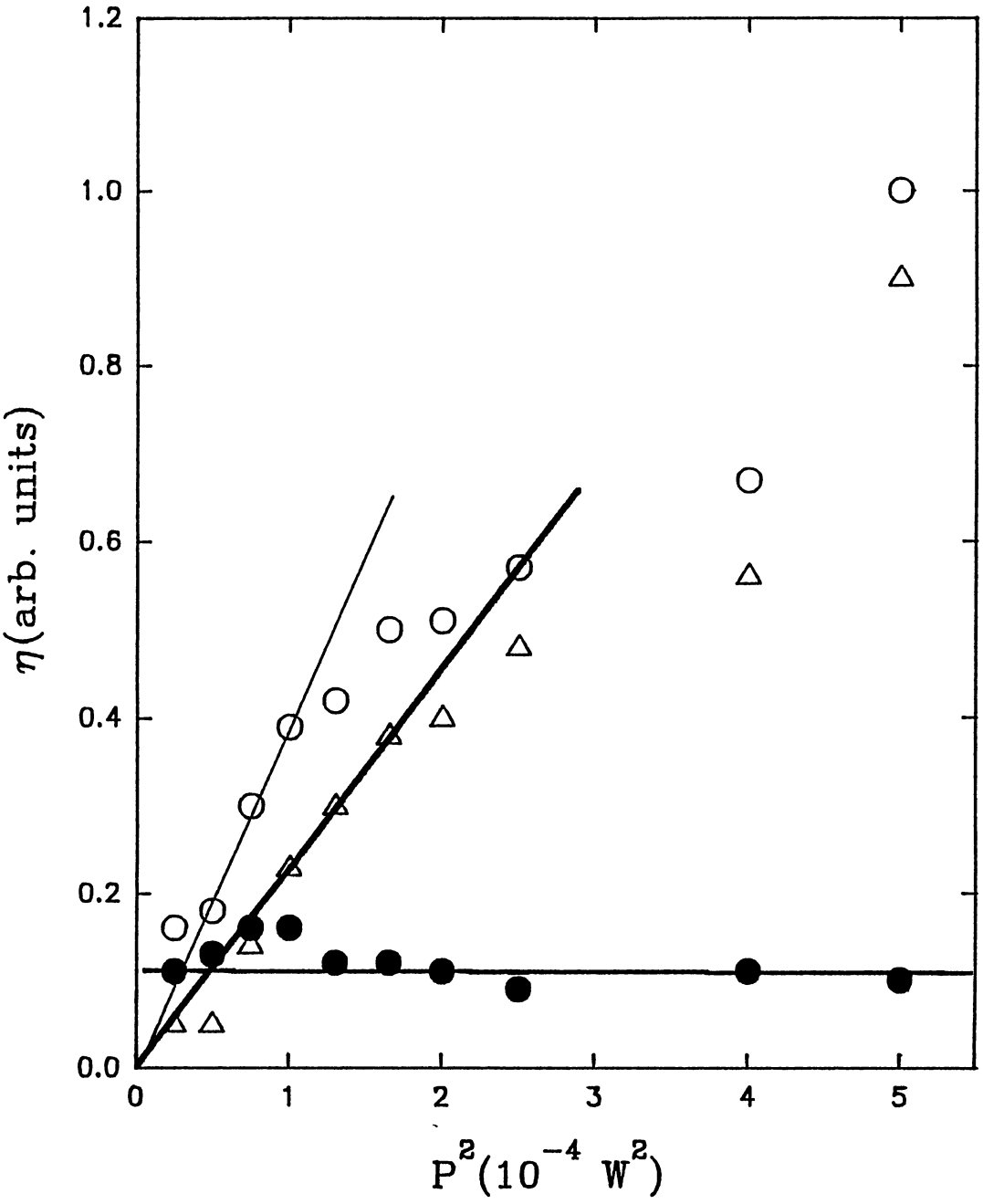

Figure 18. FWM Scattering Efficiency as a Function of Write Beam Power for Permanent(Solid (Circles), Transient (Hollow Triangles), and Total (Hollow Circles) FWM Signal in Nd:GGGM.

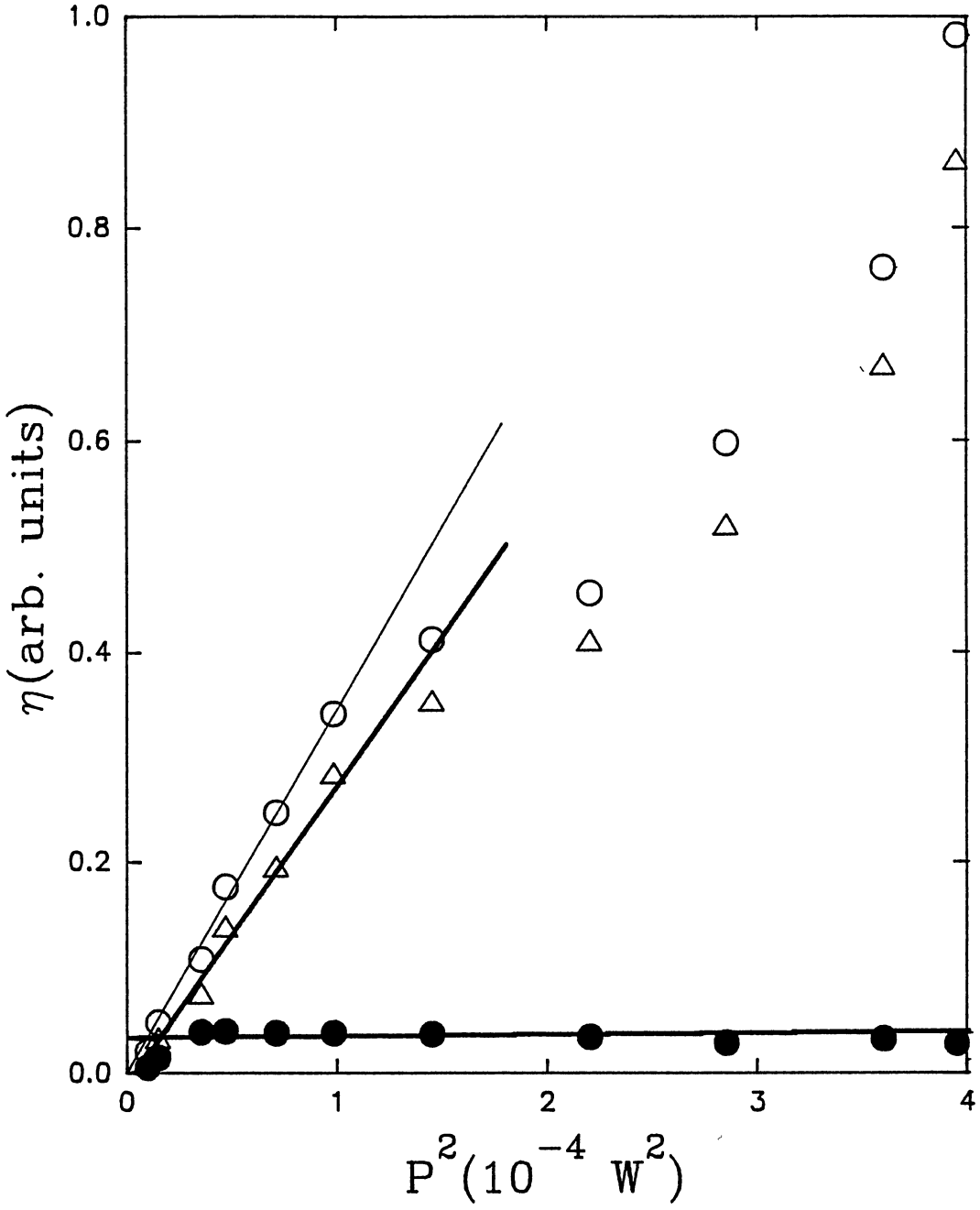

Figure 19. FWM Scattering Efficiency as a Function of Write Beam Power for Permanent (Solid Circles), Transient (Hollow Triangles), and Total (Hollow Circles) FWM Signal in Cr,Nd:GGGM.

The 488 nm and the 514.5 nm lines from an argon ion laser were used to create the excited state population gratings of the Cr^{3+} ions and the Nd^{3+} ions in these samples respectively. The write beams were interrupted by the chopper to monitor the decay of *FWM* signal.

In the limit of incoherent energy migration, the decay of *FWM* signal intensity assumes a simple exponential form given by[40]

$$I_G(t) = I_G(0)\exp[-t\{2/\tau_f - 32D(\pi/\lambda)^2\sin^2(\theta/2)\}] \qquad \text{(IV-1)}$$

where τ_f is the fluorescence lifetime of excited ions, D is the energy diffusion coefficient, θ is the crossing angle of the write beams, and λ is the write beam wavelength. For a given value of λ, the grating spacing Λ is determined by the crossing angle θ according to *Eq. (III-2)*. *Equation (IV-1)* shows that if we plot the grating decay rate (*the quantity in the curly brackets*) as a function of $\sin^2(\theta/2)$, then the slope of this curve can be used to calculate the energy diffusion coefficient D.

A typical example of the decay of transient *FWM* signal in Cr:GGGM is shown in *Fig. 20*. The decay is shown to be double exponential which is consistent with the presence of two crystal field sites for Cr^{3+} ions in this sample.[13] Since the decay rates of the two components were found to have the same temperature and crossing angle dependence, we will only show the analysis for the short component.

The grating decay rates were measured as a function of

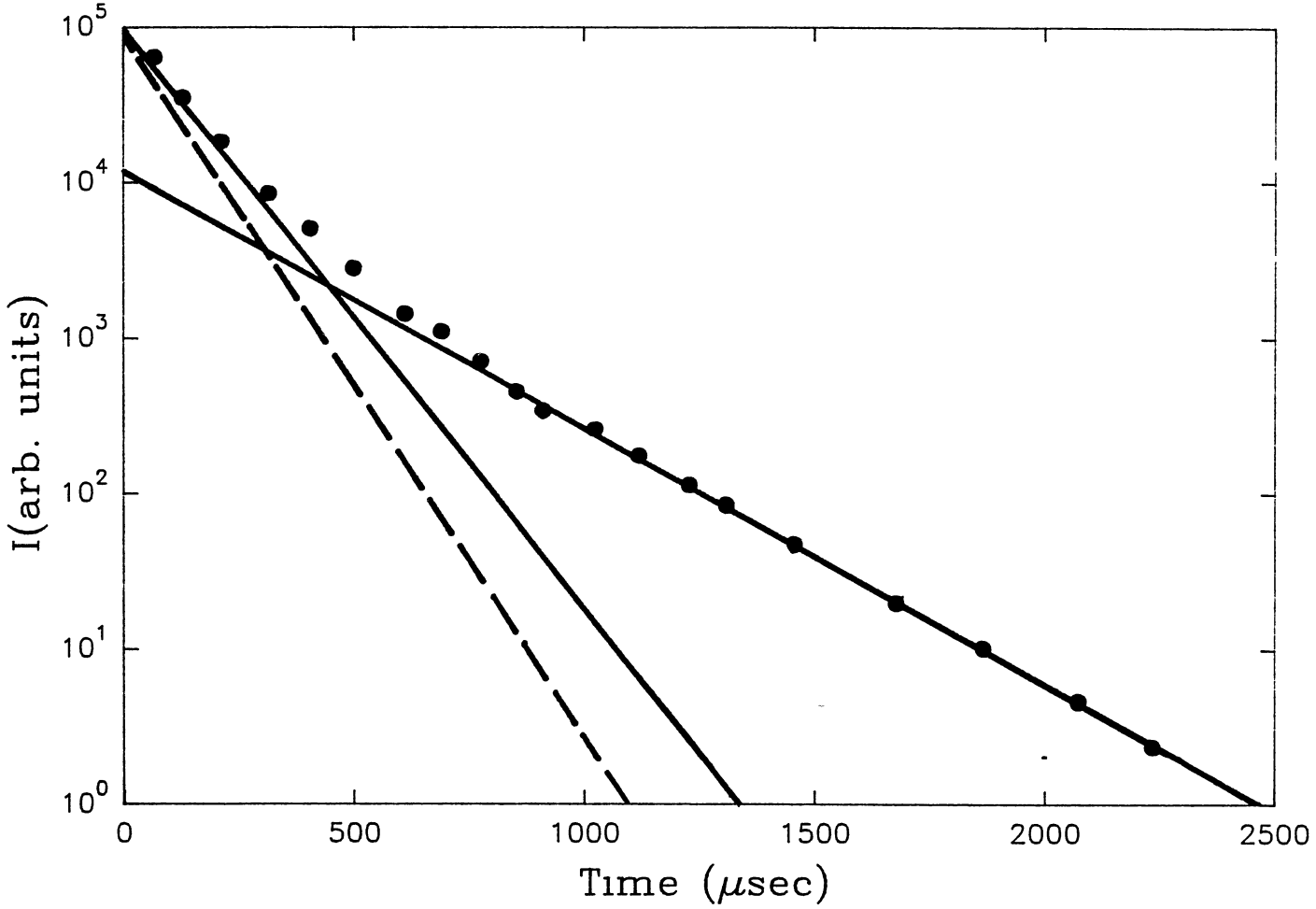

Figure 20. FWM Signal Decay Rate for Excited State Population Grating in Cr:GGGM. Total FWM Signal (circles) is made up of a Short Component (-----) and a Long Component (———).

the write beam crossing angle for temperatures between 10 K and 250 K. The crossing angles were varied from 2.5° to 22° which provides the grating spacings from 2.5 μm to 21.5 μm. In *Fig. 21*, typical results for the grating decay rates are plotted as a function of $\sin^2(\theta/2)$ for Cr:GGGM at 30 K. The plot can be easily interpolated to twice the fluorescence decay rate of Cr^{3+} ions in Cr:GGGM for $\theta = 0$, and the slope is used to calculate the energy diffusion coefficient of 5.76×10^{-5} cm^2/sec. No energy migration was observed in Cr:GGGM for temperatures exceeding 150 K. The grating decay rates for the excited state population grating of the Cr^{3+} ions in Cr,Nd:GGGM are plotted in *Fig. 22*. From the slope of this graph, we obtained a diffusion coefficient value of 4.8×10^{-7} cm^2/sec for the excitation migration among the Cr^{3+} ions in Cr,Nd:GGGM.

For multistep energy migration, the diffusion coefficient can be expressed as,[42]

$$D = 1/6 \int_0^\infty R^2 U(R) \rho(R) dR. \qquad \text{(IV-2)}$$

Here $\rho(R)$ is the probability density of finding an ion within a circle of radius R around another ion at the center and for a random distribution of ions, it is given by,

$$\rho(R) = 4\pi N_d R^2 \exp(-4\pi N_d R^3/3), \qquad \text{(IV-3)}$$

where N_d is the active ion concentration and $U(R)$ is the interaction rate between these ions. For the case of

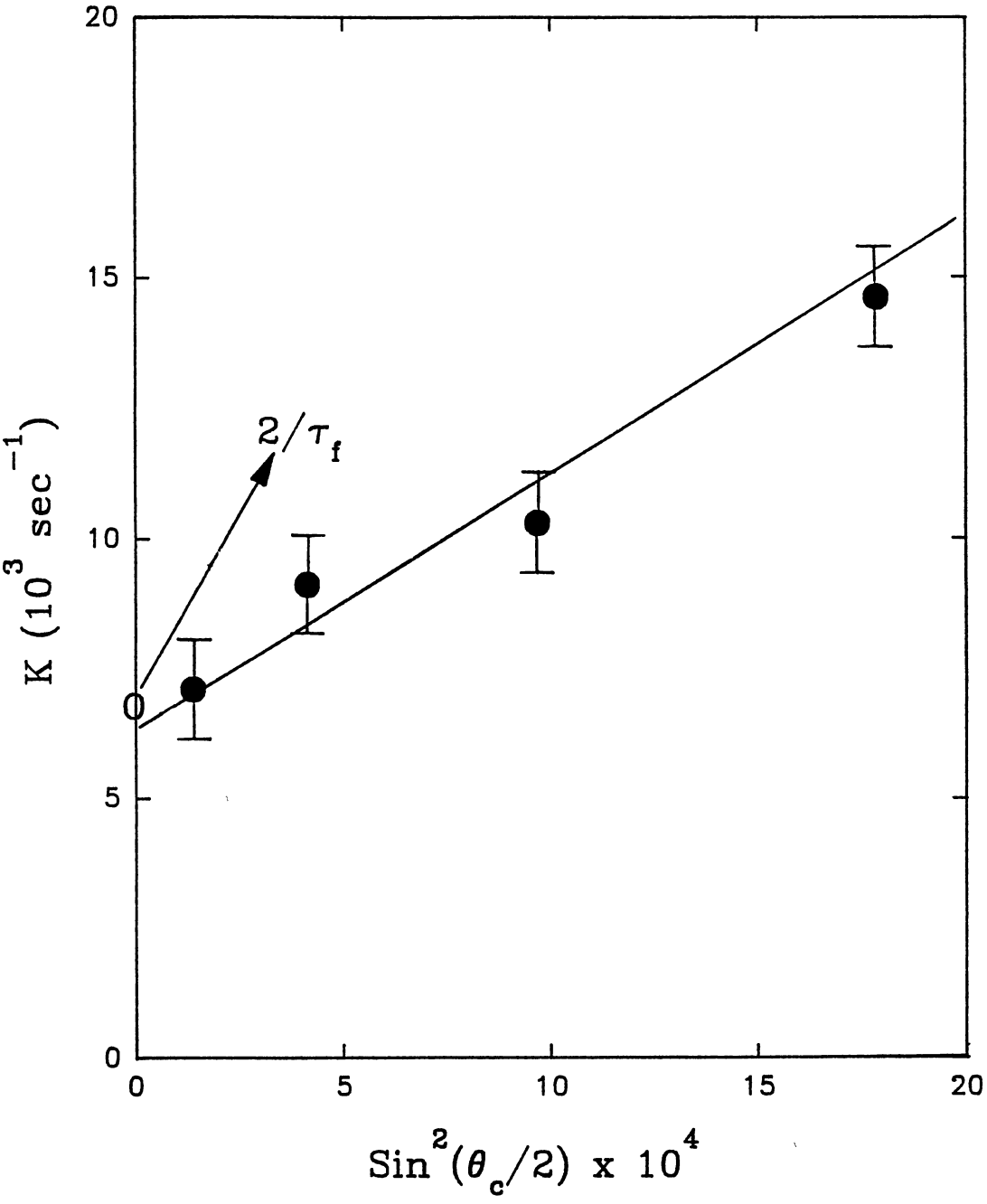

Figure 21. FWM Signal Decay Rate as a Function of $Sin^2(\theta/2)$ for Cr:GGGM. The Point at θ = 0 is Twice the Measured Fluorescence Decay Rate for Cr^{3+} Ions in Cr:GGGM.

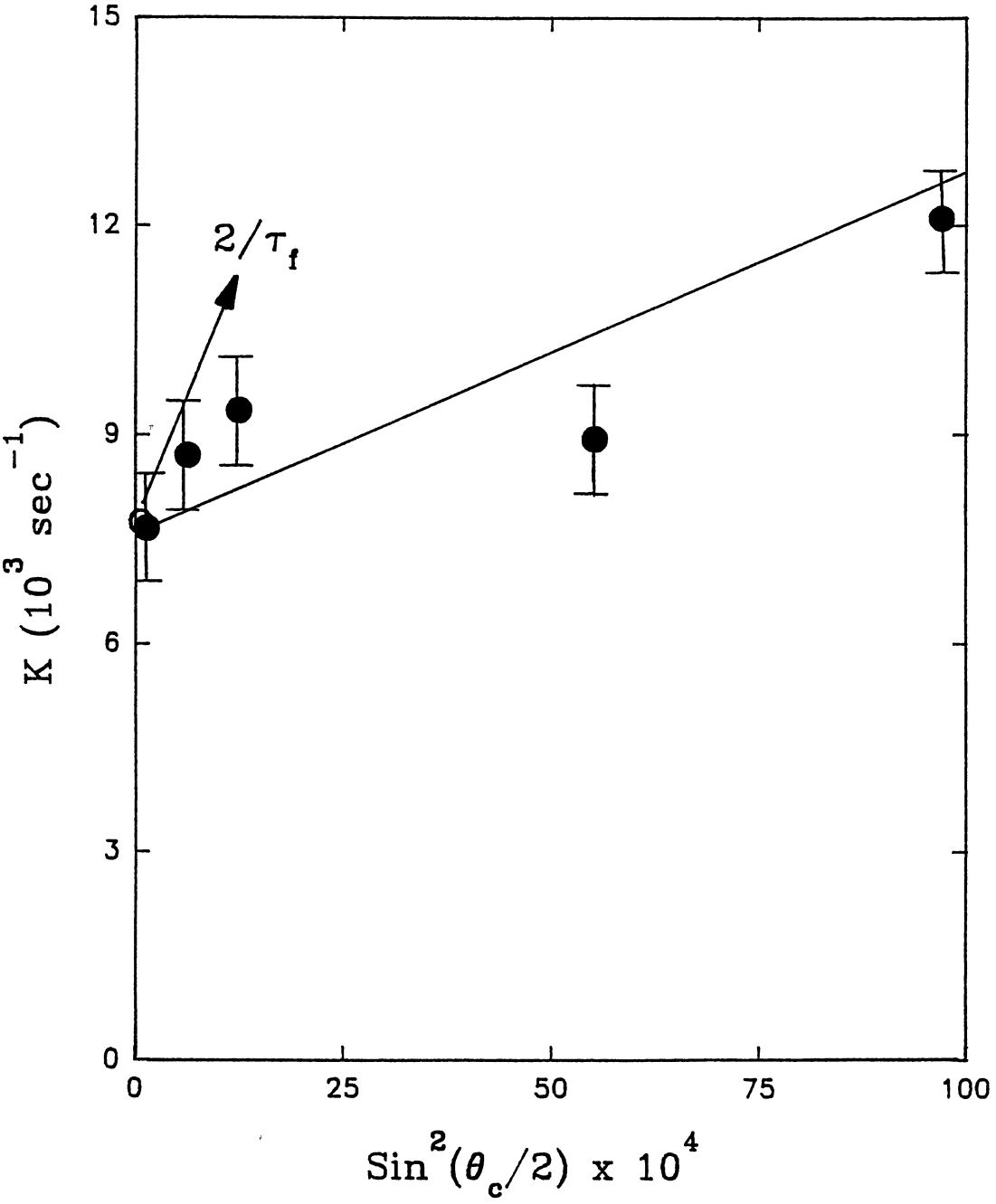

Figure 22. FWM Signal Decay Rate as a Function of $Sin^2(\theta/2)$ for Cr^{3+} Ions Grating in Cr,Nd:GGGM. The Point at $\theta = 0$ is Twice the Measured Fluorescence Decay Rate of Cr^{3+} in Cr,Nd:GGGM.

chromium ions, the interaction has been found to be predominantly of exchange character, expressed by the simple mathematical expression[43]

$$U(R) = (2\pi\Omega Z^2/\hbar)\exp(-2R/r_0)$$
$$= U_0\exp(-2R/r_0). \qquad \text{(IV-4)}$$

Here r_0 is the average Bohr radius of the wave function. Its value is always close to 1 Å and has been estimated to be 0.97 Å for ruby.[44] The parameter Z depends on the spatial overlap of the electronic wave functions and Ω depends on the overlap of the normalized emission spectrum of the sensitizers and the normalized absorption spectrum of the activators. The value of U_0 has been estimated to be 4.3×10^{14} sec^{-1} for ruby[45]. Using *Eq. (IV-3)* and *Eq. (IV-4)*, we can rewrite *Eq. (IV-2)* as,

$$D = (2\pi N_d U_0/3) \int_a^\infty R^4\exp\{-2R/L - 4\pi N_d R^3/3\}dR \qquad \text{(IV-5)}$$

where the lower limit to the integral is the distance of closest approach for the optically active ions.

The value of D for the energy migration among Cr^{3+} ions in GGGM is calculated to be 2.13×10^{-6} cm^2/sec by numerically integrating the above equation and using the estimated values of r_0 and U_0 for the case of ruby and 3.6×10^{19} cm^{-3} for chromium ions. The value of D so calculalated was not very sensitive to the choice of lower limit of the integral from 2.5 Å to 4.5 Å, therefore, the

nearest neighbor distance of 3.5 Å was used in the above calculations.[46] The uniform distribution of Cr^{3+} ions gives a larger value of inter-ionic displacement however, the smaller value used here is justified due to non-uniform distribution and the cluster formation of ions as suggested by other experiments performed on these samples. This predicted value of D is a factor of 2 smaller than the one measured for the Cr:GGGM and an order of magnitude larger than the one measured in the codoped sample. The differences between theoretical predictions and the experimental values of D can be attributed to the reasons discussed in the following.

Although the value of the parameter r_0 for GGGM is not expected to be too much different from the one used above, the value of U_0 depends upon parameters like the transition oscillator strengths and the overlap integral which are directly affected by the changes in the absorption and emission characteristics of the active ions. In the case of transition metal ions like Cr^{3+}, these characteristics are strongly affected by the local surroundings of the dopant ions producing different crystal field strengths at the sites of the dopant ions in different samples. These changes account for some of the difference between theoretical predictions and the experimental results obtained for GGGM. It should be noted however that, the value of D calculated by numerical integration of *Eq. (IV-5)* increases with the concentration of active ions and therefore, the

value of D for Cr,Nd:GGGM is expected to be smaller than the corresponding value of D in the case of Cr:GGGM. It has been observed that in GGG, some of the Gd^{3+} ions may occupy the octahedral sites instead of the usual dodecahedral sites.[47] This problem is further complicated in GGGM due to the fact that some of the (trivalent) Gd^{3+} and Ga^{3+} ions are substituted by (divalent) Ca^{2+}, Mg^{2+} and (tetravalent) Zr^{4+} ions. The values of the ionic radii for Gd^{3+}, Ca^{2+}, Ga^{3+}, Mg^{2+},and Zr^{4+} ions are 1.053 Å, 0.99 Å, 0.613 Å, 0.65 Å and 0.80 Å respectively.[48] Therefore, the substitution of some of the Ga^{3+} by Zr^{4+} in the tightly packed garnet structure, makes site-to-site variation in the local environment of Cr^{3+} ions quite complicated in GGGM. Moreover, the derivation of *Eq. (IV-5)* assumes a random distribution of ions however, it was noticed earlier that the segregation coefficient of Cr^{3+} ions in GGGM is quite large which may cause formation of the clusters of dopant ions. Since the energy transfer characteristics strongly depend upon the distribution and surroundings of the active ions, it is not unreasonable that experimentally determined value of D is larger than the theoretical predictions.

The excitation diffusion coefficient is measured as a function of temperature for all three samples. *Figure 23* and *Fig. 24* show the results for Cr^{3} ions in Cr:GGGM and in Cr,Nd:GGGM respectively. In both the samples, the experimental data (circles) can be fit to a theretical expression (line) of the form.

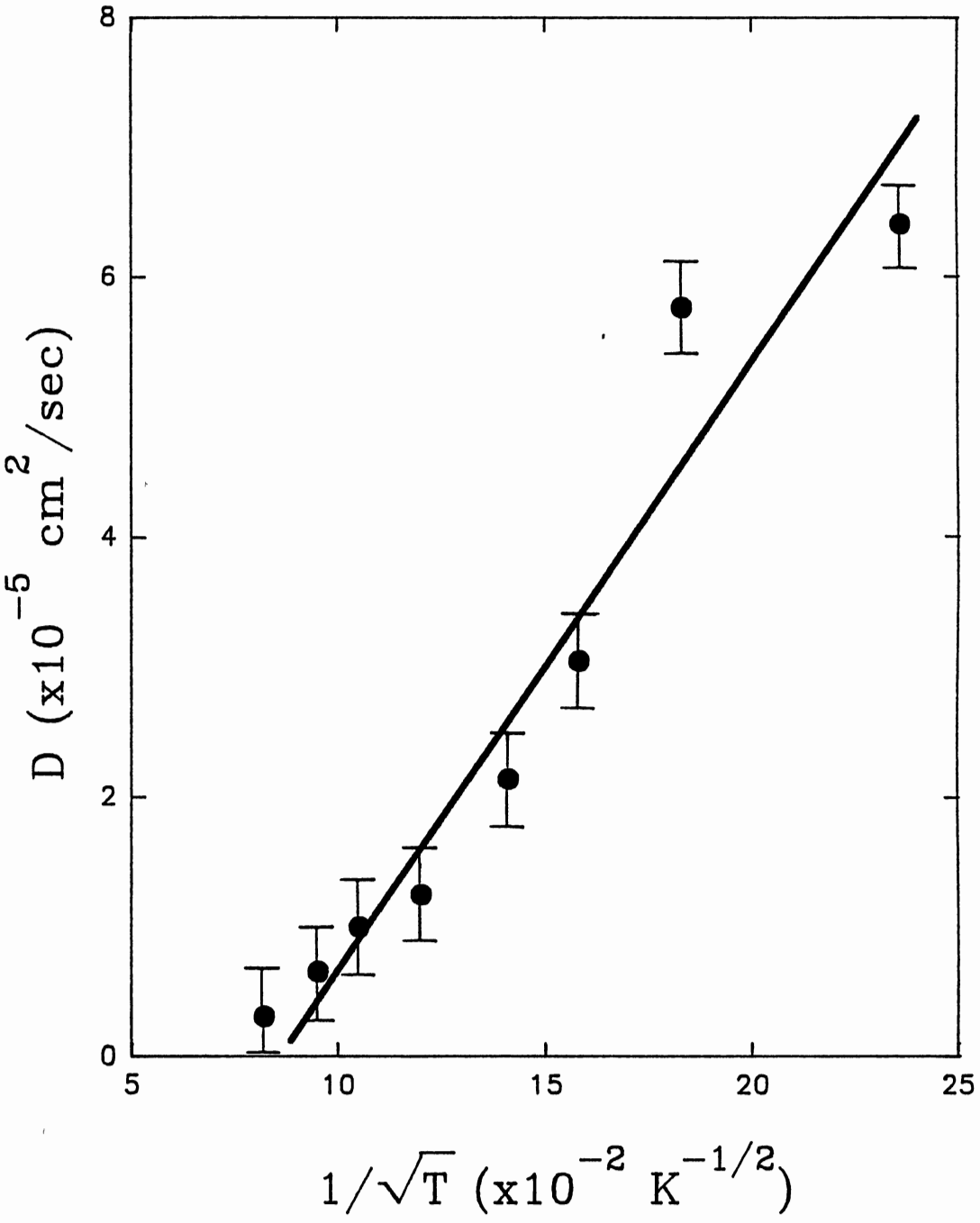

Figure 23. Temperature Dependence of Diffusion Coefficient for Energy Migration Among Cr^{3+} Ions in Cr:GGGM.

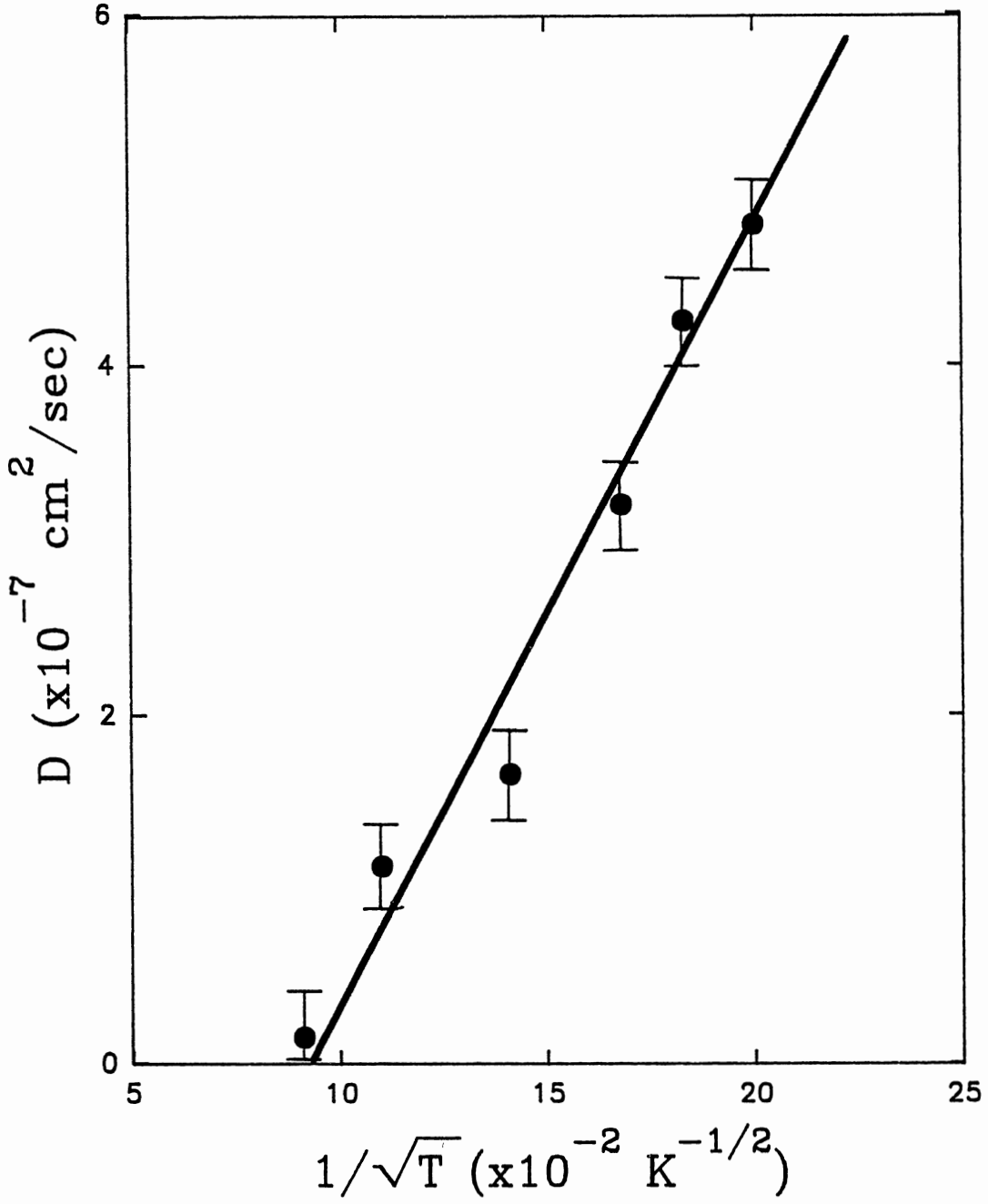

Figure 24. Temperature Dependence of Diffusion Coefficient for Energy Migration Among Cr^{3+} Ions in Cr,Nd:GGGM.

$$D = A + (B/\sqrt{T}). \qquad \text{(IV-6)}$$

Here *T* is the temperature of the sample, *A* is a constant which contains ratio of the rates of excitation scattering by acoustic phonons and by all other centers, and *B* is a constant involving the exciton velocity and the matrix element for exciton-acoustic phonon scattering. This is consistent with phonon scattering limiting the mean free path of the excitation migration.[49]

To obtain detailed information about the ion-ion interaction rate and exciton-phonon scattering rate, we have used *Eq. (III-65)*, developed by Kenkre et al.[40] for the *FWM* grating signal decay. The basic assumptions used in the development of this model are consistent with the conditions of our experiments. According to this model, in the limit of incoherent exciton migration, *Eq. (III-65)* simplifies to an exponential form and the decay of normalized transient grating signal can be described by[40]

$$I(t) = \exp(-2t\{[(1/\tau_f+\alpha)^2+b^2]^{1/2}-\alpha\}), \qquad \text{(IV-7)}$$

where τ_f is the fluorescence lifetime of the optically active ions, α is the exciton-phonon scattering rate and the parameter *b* is defined by *Eq. (III-66)*.

In *Table III*, we show the energy transfer parameters, obtained by analyzing the *FWM* signal decay in Cr:GGGM as a function of temperature and crossing angle. The ion-ion interaction rate and the exciton-phonon scattering rate for

TABLE III

ENERGY MIGRATION PARAMETERS FOR Cr:GGGM

T(K)	$\mu(sec^{-1})$ $(x10^4)$	$V(sec^{-1})$ $(x10^6)$	$D(cm^2/sec)$ $(x10^{-5})$	$L_m(\mu m)$	$L_d(\mu m)$
18	1.160	4.186	6.41	0.74	15.81
30	1.303	4.206	5.76	0.65	15.18
40	1.968	3.760	3.05	0.39	11.05
50	3.493	4.190	2.14	0.25	9.25
70	5.024	3.830	1.24	0.15	6.86
90	7.159	4.085	0.99	0.12	6.29
110	10.350	3.980	0.65	0.08	4.84
150	11.210	4.060	0.31	0.07	3.34

Cr:GGGM are plotted in *Fig. 25* as a function of temperature. The ion-ion interaction rates appear to be independent of the temperature while the exciton-phonon scattering rate increases linearly with temperature. This increase is attributed to the additional phonons available at higher temperatures.

In an attempt to understand the effects of the host lattice on the excitation migration processes in Cr-doped materials, an investigation on several Cr-doped laser crystals was carried out. No long-range energy migration was observed in ruby, the inversion site ions in alexandrite, and LLGG. Detailed information on ion-ion interaction rates and exciton-phonon scattering rates were not available from the previous results reported for GGG and GSGG. *Table IV* summarizes the results for energy transfer in GGG, GSGG, GGGM, LLGG, emerald, ruby, and inversion and mirror site ions in alexandrite at 25 K. The characteristics of energy transfer vary significantly from host to host depending on parameters such as the distance between Cr^{3+} ions, the lifetime of the metastable state, the spectral overlap between absorption and emission, and the electron-phonon interactions. The variation of each of these parameters from host to host makes it difficult to establish a simple trend for energy transfer in Cr-doped crystals.

One critical parameter in a diffusion or random walk picture of energy migration is the spacing a_0, between the

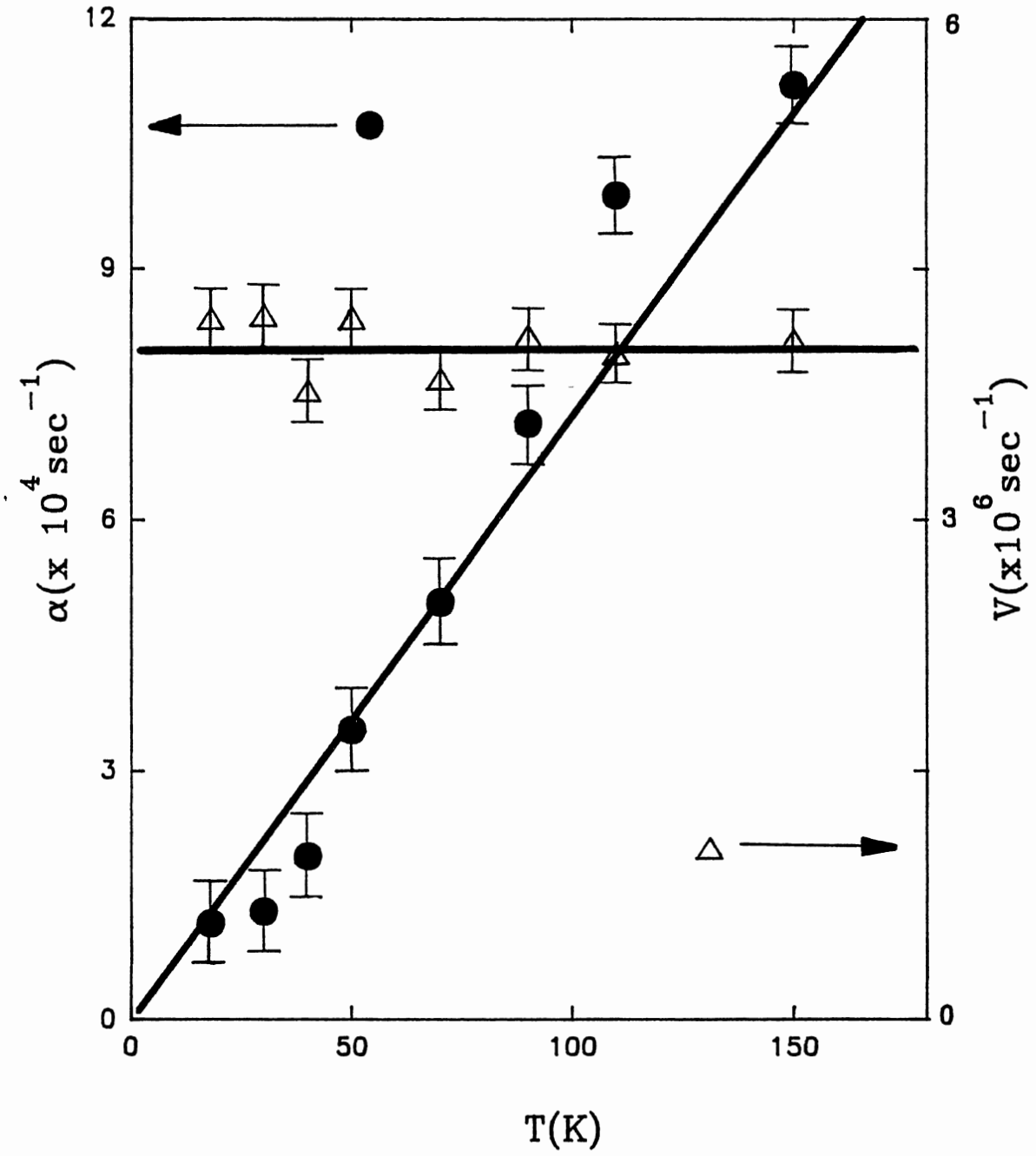

Figure 25. Temperature Dependence of Ion-Ion Interaction Rates V (△) and the Exciton-Phonon Scattering Rates α (●) for Cr:GGGM.

TABLE IV

ENERGY MIGRATION PARAMETERS FOR Cr-DOPED LASER CRYSTALS

MATERIAL AND TRANSITION	Dq (cm^{-1})	ΔE (cm^{-1})	D (cm^2/sec) $x10^{-8}$	V (sec^{-1} $x10^5$)	α (sec^{-1} $x10^3$)	T (K)	a_0 (Å)	N (cm^{-3} $x10^{18}$)	L_d (μm)
Alexandrite (inversion) $^4T_2$ (Ref. 1,2,50)	2200	6400	0	NA*	NA	ALL	41	2.5	NA
Ruby ^2E (Ref. 51)	1820	2300	0	NA	NA	ALL	59-108	79-490	3
Alexandrite (mirror) ^2E (Ref. 2,50)	1680	800	3	12	200	25	27	8.9	12
Emerald $^4T_2$ (Ref. 50-52)	1620	400	28	1.9	2.6	12	10	177	31

TABLE IV (Continued)

MATERIAL AND TRANSITION	Dq (cm^{-1})	ΔE (cm^{-1})	D (cm^2/sec) $x10^{-8}$	V (sec^{-1} $x10^5$)	α (sec^{-1} $x10^3$)	T (K)	a_0 (Å)	N (cm^{-3} $x10^{18}$)	L_d (μm)
GGG $^4T_1$ (Ref. 4,8)	1597	298	1	NA	NA	18	NA	140	NA
GGGM (Ref. 12)	1567	100	6410	42	12	18	15	54	16
GSGG $^4T_1$ (Ref. 4,8)	1565	50	10	NA	NA	230	NA	NA	NA
LLGG $^4T_1$	1480	-1000	0	NA	NA	ALL	15	50	NA

* Not Available

sites of the lattice on which the random walk is occurring. In this case a_0 is the average separation between Cr^{3+} ions. This appears explicitly in the expression for both the ion-ion interaction rate V and the energy diffusion coefficient D. This separation is influenced by the Cr^{3+} ion concentration in the sample, the host lattice spacings, and the distribution properties of the Cr^{3+} ions in the host. For mirror site ions in alexandrite crystals, it is well known that the Cr^{3+} ions are not distributed randomly and the value of a_0 used in *Table IV* was estimated from previous measurements on this sample. For other samples, the values listed for a_0 are the average Cr^{3+} ions separation assuming a uniform distribution of ions. This of course is a rough approximation to the true situation of random distribution of impurity ions. Note that for the two high crystal field cases of ruby and alexandrite inversion sites ions, the values of a_0 are extremely large. This results in a very small value for V and thus explains the lack of long range energy migration in these cases.

The samples in *Table IV* are listed in order of decreasing crystal field. As the crystal field decreases, the population distribution of the excited state of the Cr^{3+} ions changes from being primarily in the ^2E level to being primarily in the $^4T_2$ level. The latter level has a shorter lifetime and larger Stokes shift compared to the former level. The lifetime decrease results in an increase in the value of V while an increased Stokes shift decreases

the spectral overlap integral thus decreasing the number density of ions, N and V. The value of the ion-ion interaction rate decreases by an order of magnitude between alexandrite(M) and emerald and then increases by an order of magnitude between emerald and GGGM. The fluorescence lifetime is not significantly different for alexandrite(M) and emerald samples so the observed decrease in V is associated with the decreased spectral overlap. The increase in case of GGGM may however be associated with the smaller fluorescence lifetime in this sample. The increase in the value of D for these three samples is associated with the decreased values of α as well as changes in the number density of ions, N. At low temperatures, the value of V was found to be essentially independent of temperature for alexandrite(M) and the GGGM sample indicating that α and N do not change with T in this range. However in emerald, V was found to increase with temperature because N increases.[52] The temperature dependence of V was not determined for other samples.

The values of the exciton-phonon scattering rate α which limits the mean free path of the migrating energy, varies from alexandrite(M) to GGGM and is found to increase with temperature. Since the details of the exciton-phonon coupling are not known, it is not possible to predict the sample-to-sample variation in α.

From the discussion above, it is possible to understand the observed differences in the energy diffusion

coefficient D from sample to sample in Cr-doped materials. The value of D increases with increasing ion-ion interaction rate and decreases with increasing excitation scattering rate. The diffusion coefficient increases with temperature in emerald where V is phonon assisted but decreases with temperature for alexandrite mirror sites and GGGM where V is constant and α increases with temperature. Recently Basun et al.[54] have combined the techniques of site-selection spectroscopy and Stark shifting of spectral lines to distinguish between resonant and nonresonant energy transfer among Cr^{3+} ions at low temperature. They observed anomalously fast and effective resonant energy transfer among the Cr^{3+} ions in mirror sites of alexandrite crystals but not in ruby crystals. Their results are consistent with the results of *FWM* studies of energy migration in these samples.

The energy diffusion coefficient is directly proportional to the ion-ion interaction rate which is strongly affected by the fluorescence lifetime and the average spacings between active ions and therefore, on the concentration. In order to elucidate the concentration dependence of the excitation diffusion coefficient with an exchange mechanism for the ion-ion interaction, the integral in *Eq. (IV-2)* can be evaluated to give[55]

$$D(\lambda) \propto \exp(-2a_0/r_0), \qquad \text{(IV-8)}$$

where

$$a_0 = (4\pi N_d/3)^{-1/3}.$$

Table V shows the values of the measured excitation diffusion coefficients $D_{meas.}$, the concentration of active ions N_d, and $D_{norm.}$ defined as,

$$D_{norm.} = D_{meas.}\exp(2a_0/r_0). \qquad \text{(IV-9)}$$

Therefore, assuming a uniform distribution, the modified excitation diffusion coefficient, $D_{norm.}$ should be independent of the active ion concentration. A comparison of the values of $D_{norm.}$ shows that the variation in the measured values of D in the case of Emerald, GGG, and GSGG is primarily due to changes in concentration of the Cr^{3+} ions. The residual differences in the values of $D_{norm.}$ are within the error limits of these calculations. In GGGM, the large segregation coefficient may leave clusters of Cr^{3+} ions which may have decreased the separation between these ions much smaller than the one expected due to a uniform distribution. This increases the ion-ion interaction rate and hence the energy diffusion coefficient. This explanation is strengthened due to the fact that the difference between the diffusion coefficient for excitation migration among the Cr^{3+} ions in Cr:GGGM and Cr,Nd:GGGM can be explained to be entirely due to the difference in the concentration of the Cr^{3+} ions in these two samples. The grating decay for excited state population grating of the Nd^{3+} ions in Nd:GGGM were single exponentials. *Figure 26* shows the crossing angle dependence of the

TABLE V

MEASURED AND NORMALIZED ENERGY DIFFUSION COEFFICIENT AT 25 K

Material	Crystal field splitting (cm^{-1})	N ($x10^{18}$ cm^{-3})	a_0 (Å)	$D_{meas.}$ ($x10^{-8}$ cm^2/sec)	$D_{norm.}$ (cm^2/sec)
Ruby	2300	79 - 490	8 - 14	-	-
Alexandrite (Mirror)	800	8.9	30	3.0	6.38×10^{35}
Emerald	400	177.0	11	28.0	2.11×10^{20}
GGG	298	100.0	13	1.0	7.04×10^{20}
Cr:GGGM	100	54.0	16	6410.0	5.06×10^{29}
Cr,Nd:GGGM	100	36.0	19	48.0	9.85×10^{29}
GSGG	50	140.0	12	10.0	4.02×10^{20}

grating decay rates for excited state population grating of Nd^{3+} ions in Nd:GGGM sample at 30 K. The intercept of the plot at $\theta = 0$ is equal to twice the fluorescence decay rate of Nd^{3+} ions in Nd:GGGM and the slope of the curve yields an energy diffusion coefficient of 2.48×10^{-7} cm^2/sec.

A theoretical estimate of the diffusion coefficient for excitation migration among the Nd^{3+} ions was obtained using dipole-dipole interaction between Nd^{3+} ions.[46] Using *Eq. (IV-5)*, the value of energy diffusion coefficient was calculated to be 8.9×10^{-8} cm^2/sec which is slightly lower than the experimental value. The difference could be explained as due to cluster formation resulting in a high local concentration and thus smaller inter-ionic separation. This value of the diffusion coefficient is compared with similar measurements of the energy diffusion coefficient in other Nd-doped garnet crystals[61,62] and the results are presented in *Table VI*.

In an attempt to understand the sample to sample variation in values of D, a modified diffusion coefficient is defined as

$$D_{free}(cm^6/sec) = D_{meas.}(cm^2/sec)/[n_{Nd}(cm^{-3})]^{4/3}. \quad \text{(IV-12)}$$

The denominator on the right hand side of the above equation shows the concentration dependence of D for dipole-dipole interaction mechanism between dopant ions. A comparison of D_{free} values as shown in *Table VI*, suggests that in the limit of dipole-dipole interaction, the

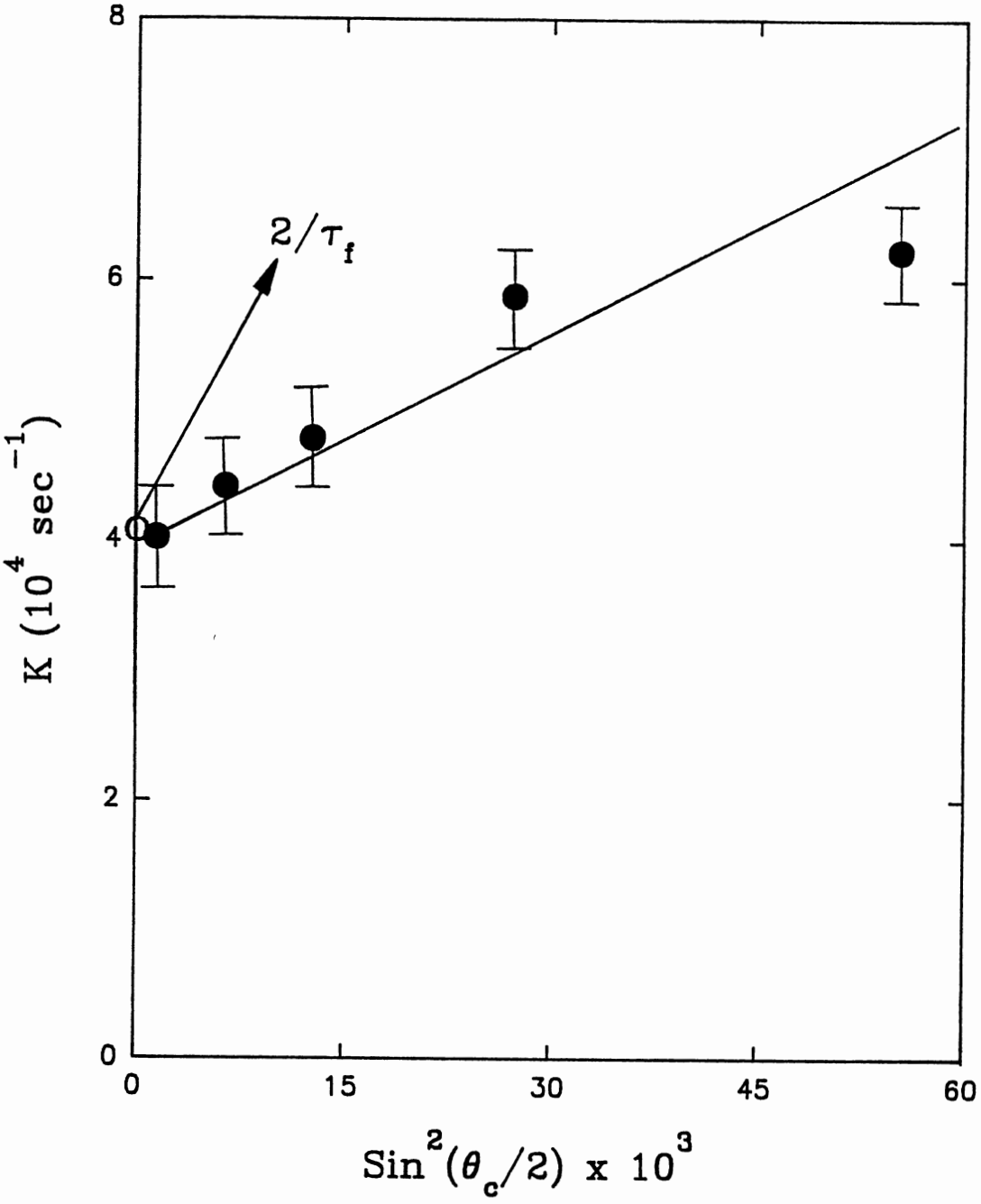

Figure 26. FWM Signal Decay Rate as a Function of $Sin^2(\theta/2)$ for Nd:GGGM. The Point at θ = 0 is Twice the Measured Fluorescence Decay Rate for Nd^{3+} Ions in Nd:GGGM.

TABLE VI

ENERGY DIFFUSION COEFFICIENT FOR Nd-DOPED GARNET CRYSTALS

Material	Concentration of Nd^{3+} ions n_{Nd}($x10^{20}$ cm^{-3})	$D_{meas.}$ ($x10^{-10}$ cm^2/sec)	D_{free} ($x10^{-37}$ cm^6/sec)
$Y_3Al_5O_{12}$ [YAG]*	1.1	3.5	7
$Y_3(Al_{0.5},Ga_{0.5})_{52}O_{12}$ [YSGG]*	1.1	9.0	17
$Y_3Ga_5O_{12}$ [YGG]*	0.27	2.0	25
$(Gd,Ca)_3(Ga,Mg,Zr)_2Ga_3O_{12}$ [GGGM]	3.02	240.0	110

*Data taken from *Ref. 61-62*

variation observed in the measured values of excitation diffusion coefficient in different garnet crystals is not entirely due to the difference in concentration of the Nd^{3+} ions from sample to sample. The short range interactions, if considered, can influence the energy migration at higher concentrations, however it is interesting to note that the D_{free} values continuously increase from YAG to GGGM and the trend continues although the concentration of Nd^{3+} ions in YGG is a factor of 5 lower than in YAG and Y(Al,Ga)G. We suggest that it may be due to the fact that Nd^{3+} ions in these mixed crystals see different environments due to the substitution of Ga^{3+},Ca^{2+}, Mg^{2+}, Zr^{4+}, and Gd^{3+} for Y^{3+} and Al^{3+}. Therefore when Al^{3+} (ionic radius = 0.558 Å) is substituted by Ga^{3+} (ionic radius = 0.613 Å), Mg^{2+} (ionic radius = 0.65 Å), or Zr^{4+} (ionic radius = 0.80 Å), the lattice parameter is increased and the much larger substitutional Nd^{3+} ions (ionic radius = 1.15 Å) can be easily accommodated. As a result, the segregation coefficient changes from 0.2 in Nd:YAG to 0.75 in Nd:GGGM. We believe this also helps in excitation migration and therefore the excitation diffusion coefficient continuously increases from YAG to GGGM. This argument however, may not be valid for other crystal structures.

The grating decay in Nd:GGGM was measured as a function of temperature from 10 K to 300 K and the data was analysed using Kenkre's theory outlined in *Chapter III* and the results are given in *Table VII*. No Energy migration is

observed beyond 150 K. The energy diffusion coefficient *D*, is plotted in *Fig. 27* as a function of temperature. Experimental data (circles) can be fit by a straight line corresponding to *Eq. (IV-6)*. The $T^{-1/2}$ temperature dependence is consistent with energy migration in this sample being limited by scattering from the acoustic phonons. *Figure 28* shows the ion-ion interaction rate V, (triangles) and the exciton-phonon scattering rates α, (circles) as a function of temperature. In this sample V is independent of temperature and α increases linearly with temperature. The value of D increases with increasing V and decreases with increasing α. The magnitude of both V and α are smaller for Nd:GGGM than in Cr:GGGM which is consistent with the smaller value of *D* in this sample.

Optical Dephasing Measurements

In a *FWM* experiment, the laser beams drive the system of ions coherently and the time it takes the system of ions to lose phase coherence affects the strength of the *FWM* signal. Dephasing can occur when the ions interact with the phonons of the system or with other ions in the ensemble or when decay to another energy level occurs. In *Ref. 1*, it was shown that the angular dependence of the scattering efficiency of the *FWM* signal can be used to calculate the T_2-dephasing time. A two level system model was developed in *Refs. 23-31*, and extended for our experimental conditions in *Ref. 1* to describe the effects

TABLE VII

ENERGY MIGRATION PARAMETERS FOR Nd:GGGM

T(K)	$\alpha(sec^{-1})$ $(x10^4)$	$V(sec^{-1})$ $(x10^5)$	$D(cm^2/sec)$ $(x10^{-7})$
10	1.49	7.03	4.52
30	2.36	7.31	2.88
50	2.76	7.18	2.48
70	5.47	6.89	1.20
90	9.11	7.41	0.98
120	12.87	7.24	0.60
150	15.13	6.90	0.03

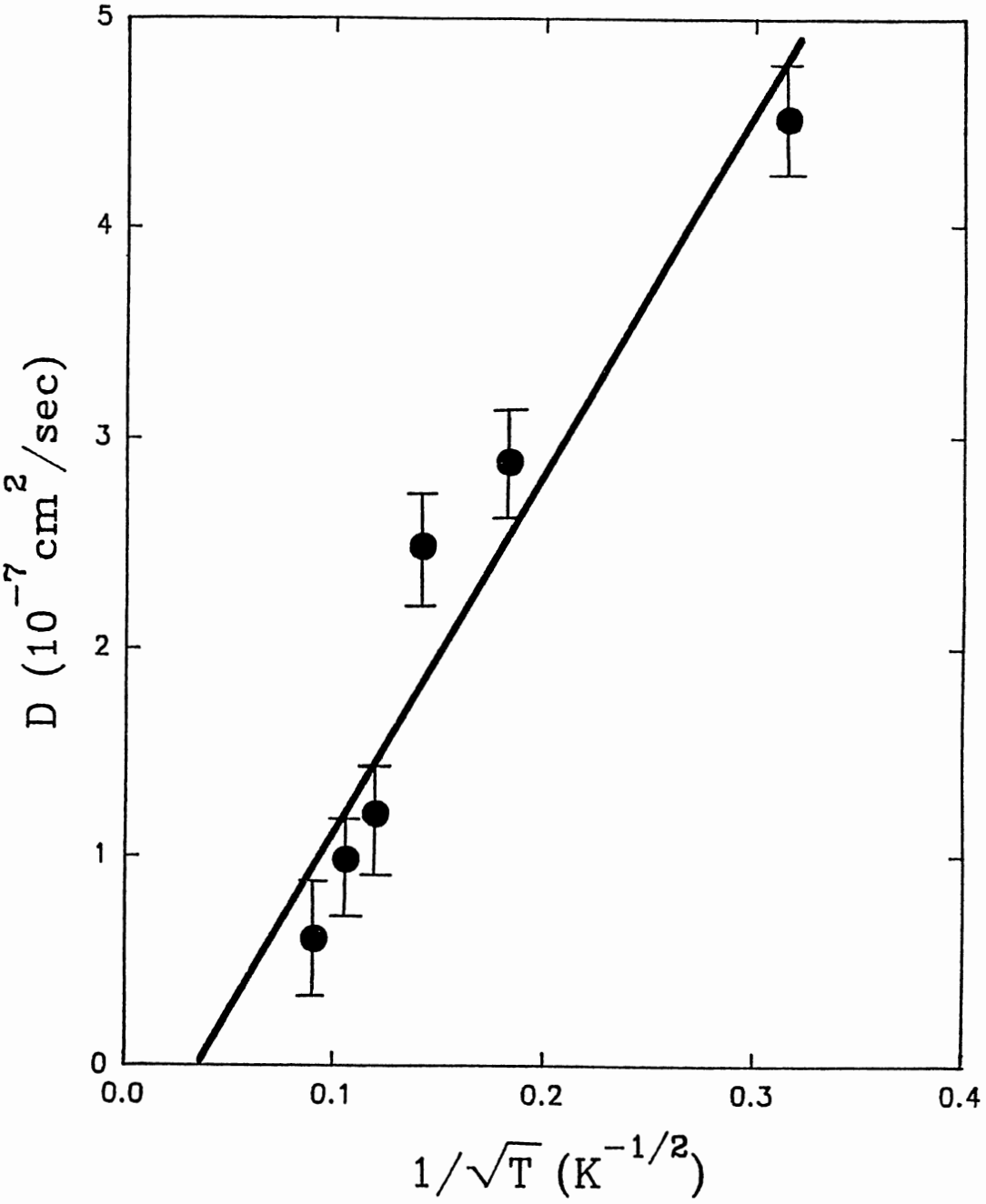

Figure 27. Temperature Dependence of Diffusion Coefficient for Energy Migration Among Nd^{3+} Ions in Nd:GGGM.

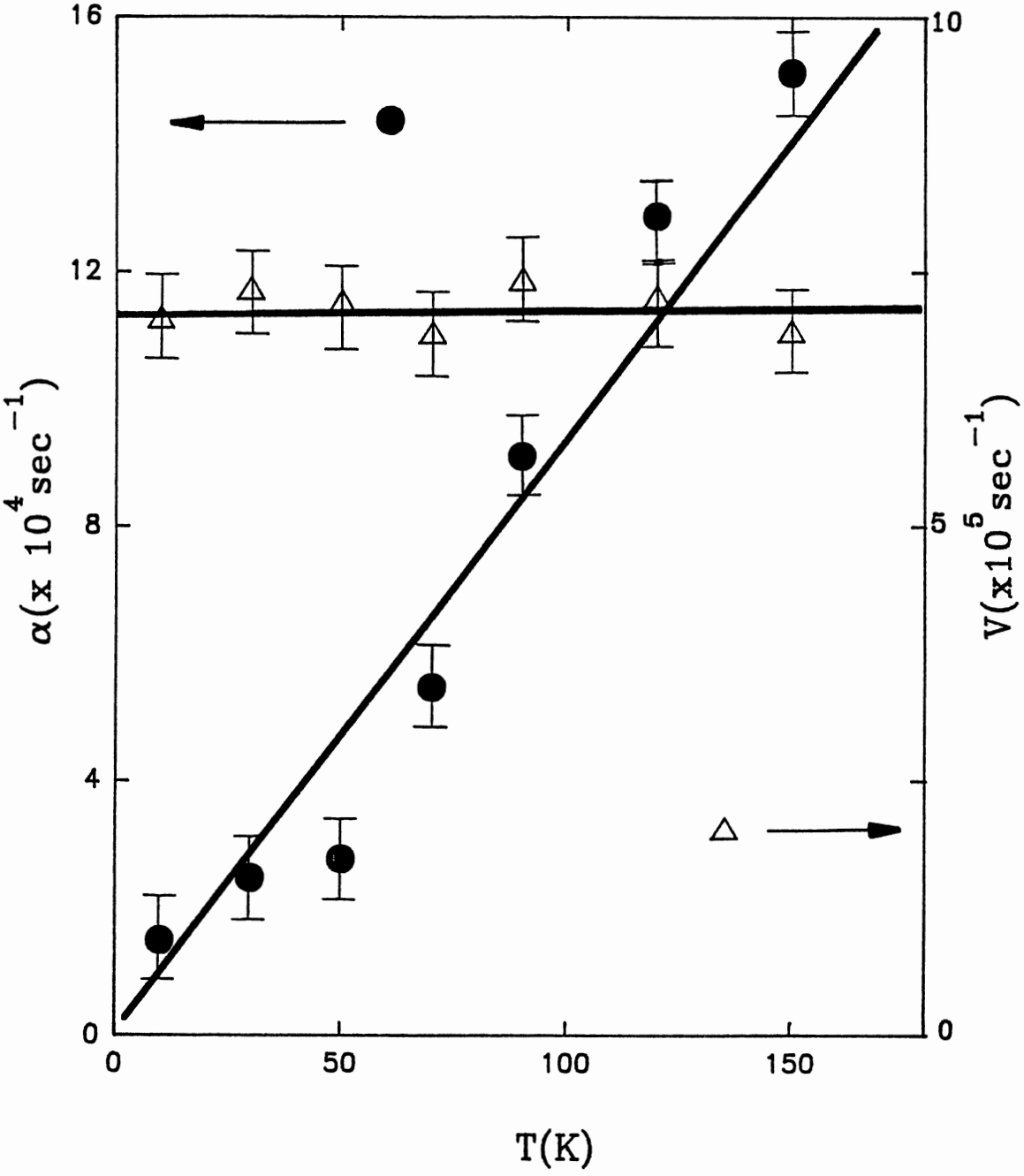

Figure 28. Temperature Dependence of Ion-Ion Interaction Rates V (△) and Exciton-Phonon Scattering Rate α (●) for Nd:GGGM.

of dephasing on the *FWM* signal. The main assumption of this model is the approximation of the ensemble of ions as a two-level system. The model describes the interaction of an ensemble of two-level systems with the four laser beams through four coupled differential equations. These equations have been solved numerically treating D_1^r, D_1^i, D_2^r, and D_2^i as adjustable parameters. These parameters are defined in *Eq. (III-13)* and *Eq. (III-14)*.

The scattering efficiency of the *FWM* signal was measured as a function of crossing angle of the write beams and the results for excitation into the $^4T_1$ band of Cr^{3+} ions in Cr:GGGM are plotted in *Fig. 29*. The values of *D* parameters for the best fit (line) to the experimental data (circles) are given in *Table-VIII*. Good agreement between theory and experiment, justifies our assumption that for write beam powers well below saturation, the two-level system model gives a reasonable description of our sample. The T_2-dephasing times, the laser induced modulation in the absorption coefficient $\Delta\alpha$, and in the refractive index Δn, were calculated using *Eq. (III-15)*, *Eq. (III-16)*, and *Eq. (III-17)* respectively. The values of the parameters used to obtain the best fit alongwith the calculated dephasing times for different materials used in this survey are given in *Table VIII* and the values of the laser induced modulations $\Delta\alpha$ and Δn are given in *Table IX*.

Figures 30 - 32 give the experimental data (circles) and theoretical fit (line) for the scattering efficiency

TABLE VIII

PARAMETERS FOR BEST FIT TO THE FWM SCATTERING EFFICIENCY VERSUS CROSSING ANGLE PLOT AND THE T_2-DEPHASING TIME FOR Cr-DOPED LASER MATERIALS

MATERIAL AND TRANSITION	D_1^r	D_1^i	D_2^r	D_2^i	T_2 (ps)
Alexandrite[1] (inversion) $^4T_2$	0.006	0.015	0.135	0.00002	80±5
Ruby[1] $^4T_2$	NA*	NA	NA	NA	4.5±3
Alexandrite[1] (mirror) $^4T_2$	NA	NA	NA	NA	2.2±4
Alexandrite[2] (mirror) ^2E	0.250	0.650	0.350	0.0015	55.3
Emerald[52] $^4T_2$	5.0×10^{-7}	4.0×10^{-7}	2.0×10^{-6}	8.0×10^{-9}	1.2

TABLE VIII (Continued)

MATERIAL AND TRANSITION	D_1^r	D_1^i	D_2^r	D_2^i	T_2 (ps)
GGG $^4T_2$	0.205	0.20	0.230	0.0007	1.35±0.5
GGG $^4T_1$	0.20-0.45	0.09-0.20	0.27-0.31	0.01-0.05	0.008-0.033
GSGG $^4T_2$	0.210	0.18	0.240	0.001	0.77±0.5
GSGG $^4T_1$	0.30	0.30	0.31	0.01	0.033
GGGM $^4T_1$	0.92	0.01	0.100	0.05	0.0028±0.5
GGGM $^4T_2$	0.200	0.22	0.235	0.001	0.92±0.5
LLGG $^4T_1$	0.400	0.280	0.303	0.015	0.74±1.0

* Not Available

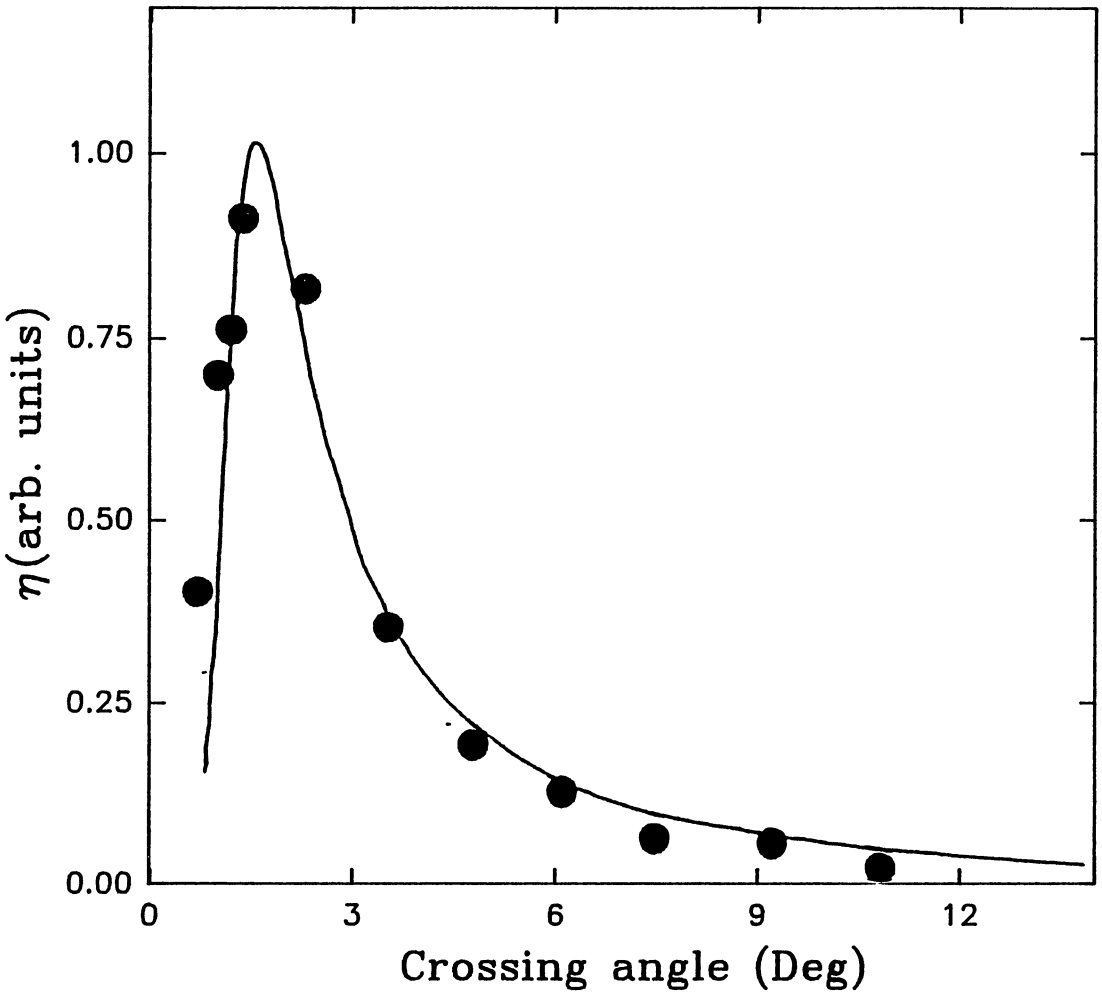

Figure 29. FWM Scattering Efficiency as a Function of Crossing Angle of the Write Beams for Excitation Into $^4T_1$ Band of Cr:GGGM. The Circles Denote the Experimental Data and the Line Represents Theoretical Fit Using a Two Level System Approximation.

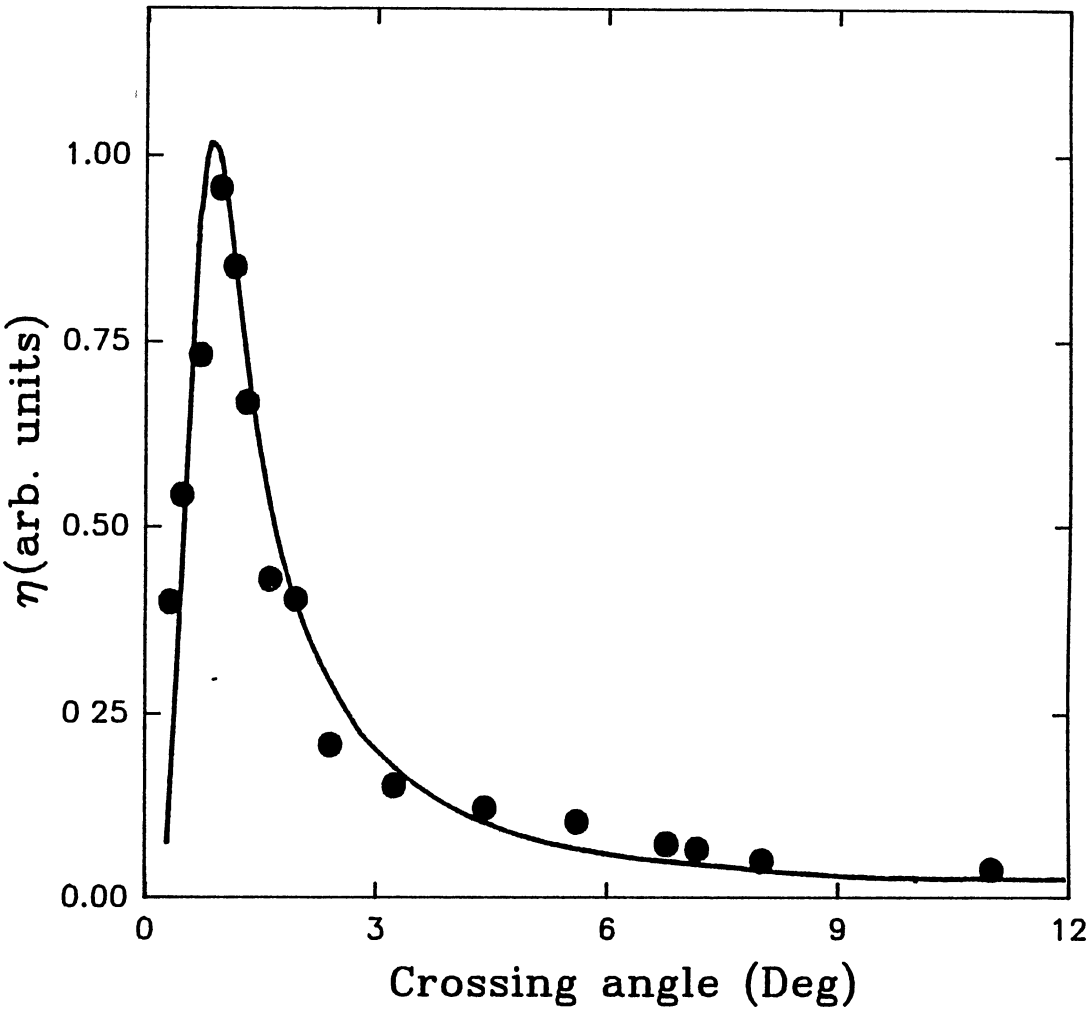

Figure 30. FWM Scattering Efficiency as a Function of Crossing Angle of the Write Beams for Excitation Into $^4T_2$ Band of Cr:GGGM. The Circles Denote the Experimental Data and the Line Represents Theoretical Fit Using the Two Level System Approximation.

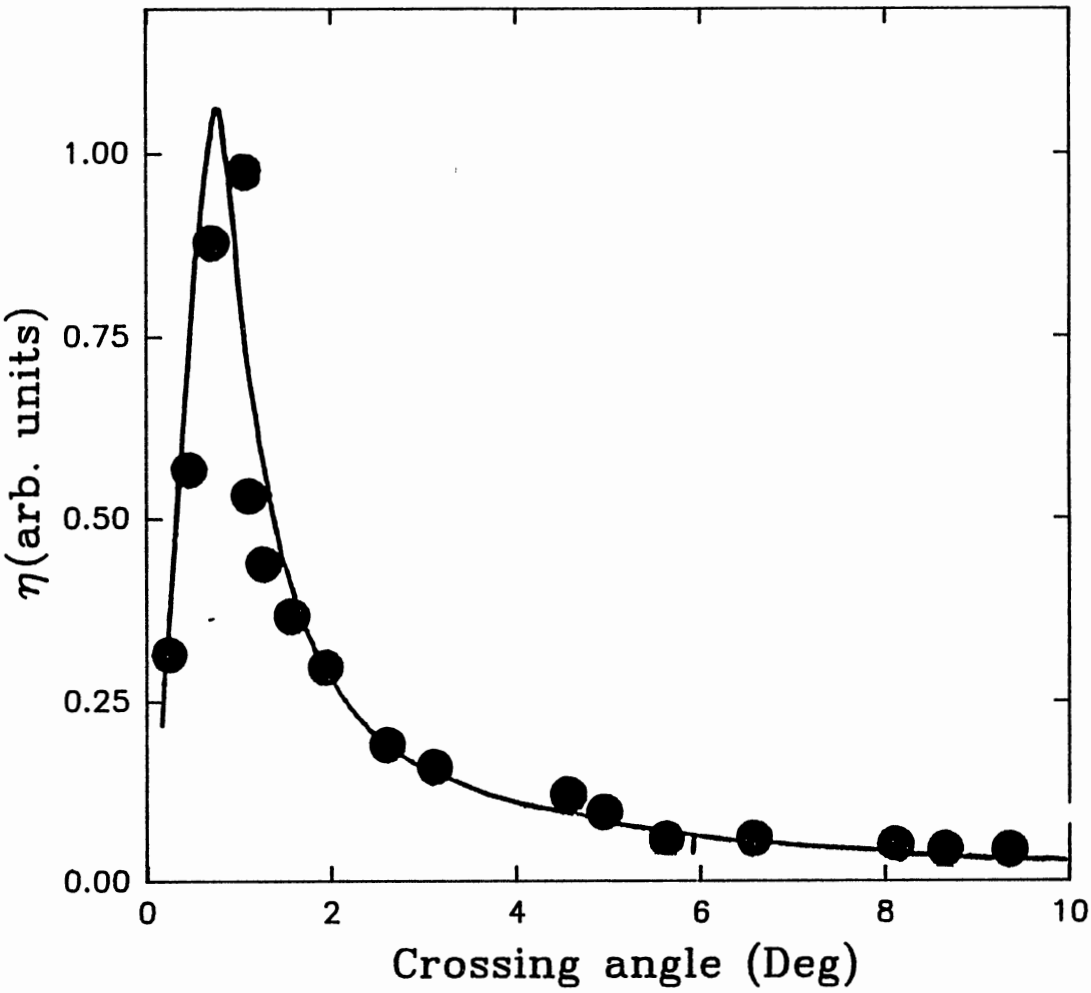

Figure 31. FWM Scattering Efficiency as a Function of Crossing Angle of the Write Beams for Excitation Into $^4T_2$ Band of Cr:GGG. The Circles Denote the Experimental Data and the Line Represents Theoretical Fit Using the Two Level System Approximation.

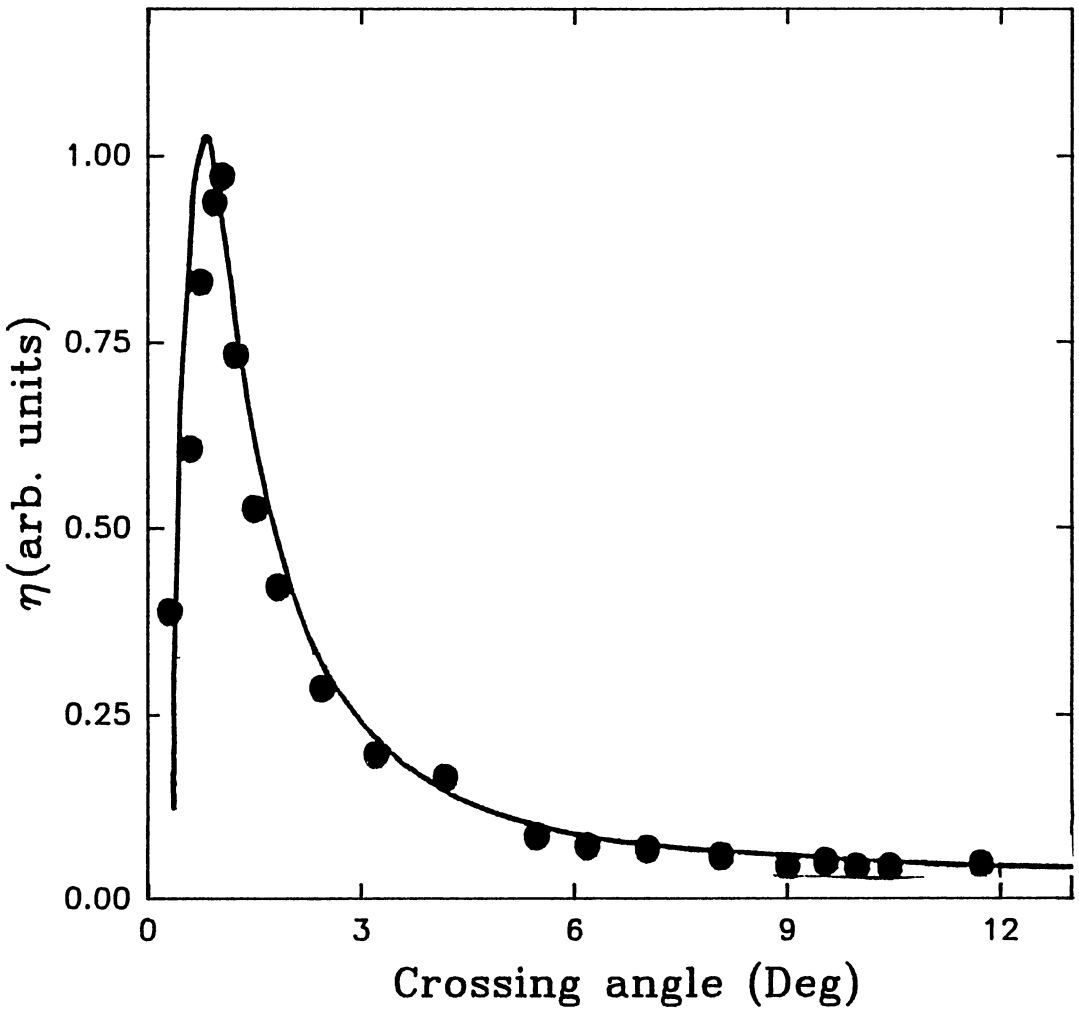

Figure 32. FWM Scattering Efficiency as a Function of Crossing Angle of the Write Beams for Excitation Into $^4T_2$ Band of Cr:GSGG. The Circles Denote the Experimental Data and the Line Represent Theoretical Fit Using the Two Level System Approximation.

TABLE IX

RESULTS OF DEPHASING TIME MEASUREMENTS ON Cr-DOPED LASER MATERIALS

Material	ΔE (cm^{-1})	$K_{n.r}(ISC)/K_{n.r.}(IC)$	$\Delta\alpha$ (cm^{-1})	Δn (10^{-5})
Ruby[1]	3850	31	.00106	8.16
Alexandrite[1] (Mirror)	1950	13	.0019	1.83
Emerald[52]	1800	4.0	.22	13
GGG	1650	2.6	.0013	
GGGM	1250	2.3	.0029	.0563
GSGG	1150	2.2	.0013	.0513

as a function of write beam crossing angle for excitation into the $^4T_2$ band of Cr^{3+} ions in GGGM, GGG, and GSGG respectively. The values of the parameters used to obtain the best fit and the corresponding dephasing times are given in *Table VIII* and the values of laser induced modulations $\Delta\alpha$ and Δn, are given in *Table IX*.

The two level system model used in the analysis for determining the dephasing time, change in the refractive index (Δn), and change in the absorption coefficient ($\Delta\alpha$), despite its unrealistic simplicity, has been justified on the basis of its ability to predict the values of $\Delta\alpha$ which are consistent with the values measured independently by excited state absorption measurements. Such checks have been made when values of the excited state absorption cross section, σ_f, are available such as for alexandrite[50], emerald[51,53], ruby[63], and GSGG.[64] It should however be approached with caution. *Equation (III-15)* shows how $\Delta\alpha$ depends on the fitting parameter D_2^i, however, the computor fit to the crossing angle dependence of the *FWM* scattering efficiency can be relatively insensitive to the parameter D_2^i. This may result in large error bars for $\Delta\alpha$ and since the T_2-dephasing time depends on $\Delta\alpha$ through *Eq. (III-17)*, it will also have large error bars.

As pointed out in *Chapter III*, while the effective two level model can adequately describe the systems like atomic vapors, it is a very poor approximation for ions in solids where more than two states are effectively involved.

Recently, the results of *FWM* measurements on Nd-doped materials has been analyzed using a model based on an effective four-level system.[33] In this model, the laser beams interact with ions both in the ground state and the metastable state. The transitions from the ground and the metastable states to higher energy states are accounted for by combining the upper states into two effective states. A density matrix formalism yields the change in real and imaginary parts of the susceptibility between ions in the peak and valley region of a population grating. By measuring the absolute magnitude of the *FWM* signal in a variety of samples, it was concluded that dominant contribution to the signal comes from the real part of nonlinear susceptibility associated with the off-resonant, allowed transitions to the levels of different configuration in the ultraviolet spectral region. In this case the weak contribution to the signal associated with the imaginary part of the nonlinear susceptibility comes from the resonant interaction with the pump transition.

The scattering efficiency η of the *FWM* signal for a population grating in a sample described as an ensemble of effective four level systems was calculated in *Ref. 33*. The levels representing the system are the ground state $|g\rangle$, the metastable state $|m\rangle$, the pump band $|a\rangle$, and the charge transfer band $|b\rangle$. Their results assumed a specific small write beam crossing angle. We have extended these results to include the effects of changing the crossing angle of

the write beams changing the interaction length and the density of the grating fringes. For excitation levels much below the saturation levels, the scattering efficiency of the *FWM* signal is given by *Eq. (III-45)*. This equation shows that *FWM* scattering efficiency depends upon the laser induced changes in the absorption cross section σ, and the polarizability α_p, defined by the following expressions.

$$\sigma(ij) = (8\pi^2/n\hbar\lambda)[|\mu_{ij}|^2 T_{2,j}^{-1}/\{(\omega_{ij}-\omega_0)^2+T_{2,j}^{-2}\}], \quad \text{(IV-13a)}$$

and

$$\alpha_p(ij) = (2\omega_{ij}/\hbar)|\mu_{ij}|/(\omega_{ij}^2-\omega_0^2). \quad \text{(IV-13b)}$$

Where ω is the frequency of the laser beams, ω_{ij} is the transition frequency connecting the levels $|i>$ and $|j>$, μ_{ij} is the corresponding dipole moment and $T_{2,i}$ is the T_2-dephasing time defined in terms of the rates β_{ij} and $\beta_{dephase}$ as

$$T_{2,i}^{-1} = \beta_{ij}/2+\beta_{dephase}. \quad \text{(IV-14)}$$

We will now attempt to demonstrate that the effective four level system model provides similar results as derived using a much simpler two level system model with a few constraints. However the effective four level model, being closer to the real system than the two level model, provides increased understanding of the physical processes responsible for the creation of grating.

Figure 33 shows a typical fit for scattering efficiency versus the crossing angle curve for the $^4T_2$

pumping in Cr-doped GGGM. The initial rise is due to the presence of the term $(\rho_0/\Lambda)^2$ whereas the fast decay is predominantly due to the exponential term inside the integral sign. The competition between these two terms determines the maximum of the scattering efficiency. The angular dependence due to the terms $\{1-\exp(-a_w L\sec\theta)\}^2$ and $\exp(a_p L\sec\theta)$ are not significant for the crossing angle values used in these experiments.

The T_2-dephasing time can be written in terms of the laser induced changes in the real and imaginary parts of the complex succeptibility as

$$T_2 = 1/(\omega-\omega_{ga})\{\Delta\chi_R/\Delta\chi_I\}, \qquad \text{(IV-15)}$$

where $\Delta\chi_R$ and $\Delta\chi_I$, the real and the imaginary parts of the change in susceptibility of the sample, are related to $\Delta\alpha_p$ and $\Delta\sigma$ by the following expressions.

$$\Delta\chi_R = 2\pi f_L{}^2 N_m \Delta\alpha_p,$$

and

$$\Delta\chi_I = n\lambda N_m \Delta\sigma/4\pi,$$

where N_m is the population of the metastable state. For our system, $\Delta\sigma$ and $\Delta\alpha_p$ can be given by,

$$\Delta\sigma = \sigma(^4A_2 - {}^4T_2) - \sigma(^2E - C.T.), \qquad \text{(IV-16a)}$$

and

$$\Delta\alpha_p = \alpha_p(^4A_2 - {}^4T_2) - \alpha_p(^2E - C.T.). \qquad \text{(IV-16b)}$$

Where *C.T.* stands for charge transfer band. It should however be noted that in the samples used in these studies

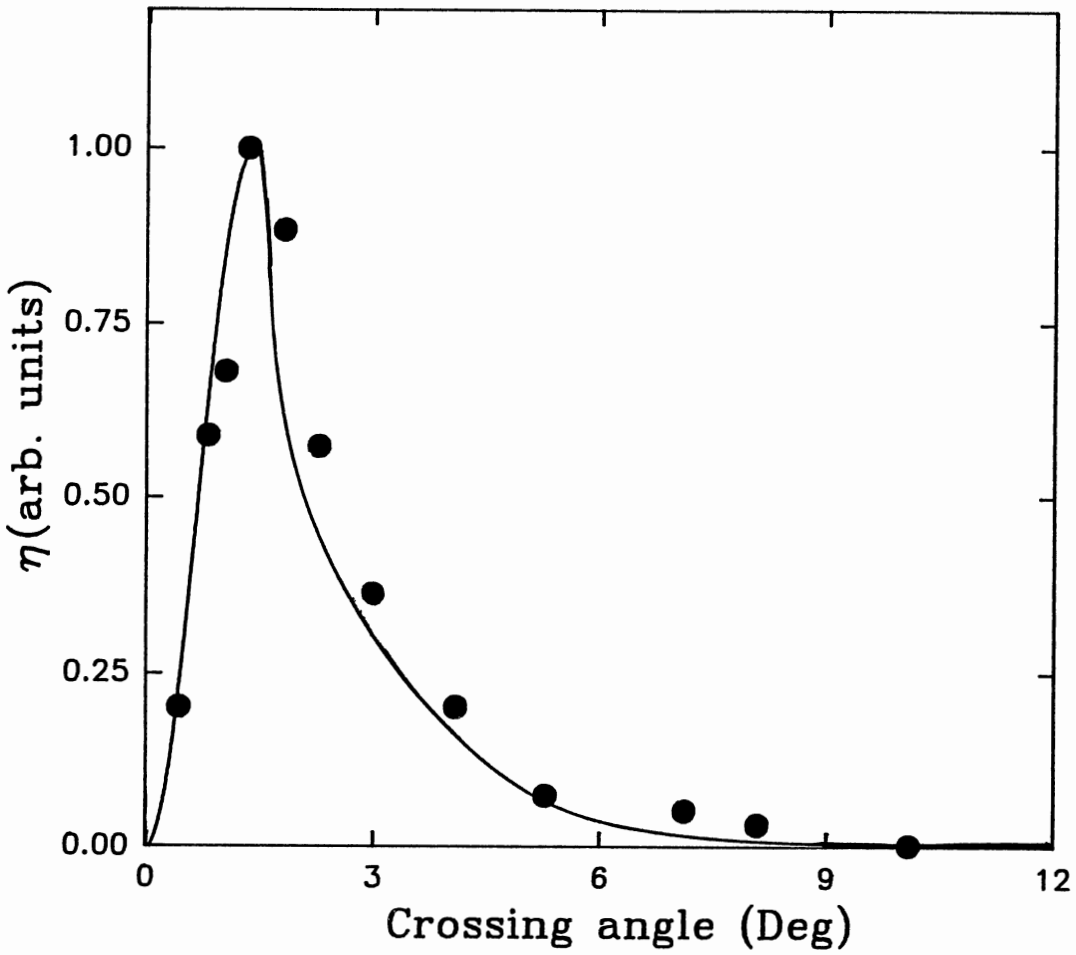

Figure 33. FWM Scattering Efficiency as a Function of Crossing Angle of the Write Beams for Excitation Into $^4T_2$ Band of Cr:GGGM. The Circles Denote the Experimental Data and the Line Represents Theoretical Fit Using the Effective Four Level System Model.

$$\sigma(^4A_2 - {}^4T_2) >> \sigma(^2E - C.T.), \quad \text{and}$$

$$\alpha_p(^2E - C.T.) >> \alpha_p(^4A_2 - {}^4T_2).$$

Therefore,

$$\Delta\sigma/\Delta\alpha_p \simeq \sigma(^4A_2 - {}^4T_2)/\alpha_p(^2E - C.T.).$$

Thus, by pumping into the $^4T_2$ band of the Cr-doped samples, $\Delta\sigma/\Delta\alpha_p$ gives a measure of the T_2-dephasing time of the $^4T_2$ level.

The data for the scattering efficiency of the *FWM* signals as a function of the write beam crossing angle were fitted to *Eq. (III-45)* for Cr-doped GGGM, GSGG, and GGG using $\Delta\sigma$ as the adjustable parameters. The value of $\Delta\alpha_p$ was calculated by the procedure outlined by Weaver and Payne[65] using the polarizability changes α_E and α_T for ^2E and $^4T_2$ levels weighted by the corresponding Boltzmann factors for the ^2E and $^4T_2$ levels as

$$\Delta\alpha_p = \alpha_E f_E + \alpha_T f_T \qquad \text{(IV-17)}$$

where $\alpha_E = 0.017$ Å^3, $\alpha_T = 0.155$ Å^3 and f_E and f_T are given by

$$f_i = \{g_i \exp(-\Delta E_i/KT)\}/\{\sum_{j=1}^{2} g_j \exp(-\Delta E_j/KT)\}. \qquad \text{(IV-18)}$$

Here i and $j = E$ or T corresponding to ^2E and $^4T_2$ levels, the degeneracy g is 4 for ^2E and 12 for $^4T_2$ levels, and ΔE_i is zero for ^2E and it is equal to ΔE (the crystal field splitting of the ^2E and $^4T_2$ levels in Cr-doped samples) for $^4T_2$ level. The values of ρ_0 were calculated using the

laser beam radius corrected for the changes caused by the refractive index of the sample for the value of crossing angle corresponding to the maximum of scattering efficiency and slight variation was allowed due to its dependence on the crossing angle. The ratio ($\Delta\sigma/\Delta\alpha_p$) corresponding to the values obtained by the best fit, was used to calculate the T_2-dephasing time. The values of 2.03 *psec*, 2.51 *psec* and 3.01 *psec* were obtained for the T_2-dephasing time in GSGG, GGGM and GGG respectively. These values are somewhat higher than the corresponding values obtained by using the two level model however the sample to sample variation is the same. The experimental data for alexandrite and emerald had large error bars, therefore, the corresponding values of the T_2-dephasing time also had large uncertainties. It is important to note that exciting higher in the high energy side of the transition increases the T_2 values. This can be understood as due to the fact that from *Eq. (IV-13)*, for a fixed value of ω_{ij}, increasing ω_0 (*the excitation frequency*) decreases $\Delta\alpha_p$ but it decreases $\Delta\sigma$ even more and as a result T_2 which is proportional to the ratio $\Delta\alpha_p/\Delta\sigma$, increases.

In order to understand why a very simple two level system model can explain some of the experimental results to a reasonable accuracy, we substitute the values of $\Delta\chi_R$ and $\Delta\chi_I$ in *Eq. (IV-15)* to obtain the explicit expression for T_2 as

$$T_2=\{\hbar/2n(\omega-\omega_{ga})\}(T_{2,b}^{-1}|\mu_{mb}|^2/\{(\omega_{mb}-\omega)^2-T_{2,b}^{-2}\}$$
$$-T_{2,a}^{-1}|\mu_{ga}|^2/\{(\omega_{ga}-\omega)^2-T_{2,a}^{-2}\})$$
$$*(\omega_{mb}|\mu_{mb}|^2/\{\omega_{mb}^2-\omega^2\}-\omega_{ga}|\mu_{ga}|^2/\{\omega_{ga}^2-\omega^2\}), \qquad \text{(IV-19)}$$

For chromium doped laser crystals $\mu_{mb} > \mu_{ga}$, however if $T_{2,b} >> T_{2,a}$ then near-resonant pumping in $^4T_2$ level enhances the terms corresponding to the level $|a\rangle$ such that the terms corresponding to the level $|b\rangle$ can be considered negligible and the above result reduces to that derived using the familiar two level system approximation. It should however be emphasized that only a multilevel system model can completely and accurately describe the processes involving ions in solid and the two level system model can only provide approximate results.

Accurate confirmation of the values of T_2-dephasing time should come from a direct measurement of the dephasing time. Independent measurements like photon echo could be used to directly measure the T_2-dephasing times in these Cr-doped materials.

For excitation into the $^4T_2$ band of chromium ions, the dephasing is dominated by the time an ion takes to relax to the metastable ^2E level. This relaxation can follow two possible paths. *Figure 34* (adopted from *Ref. 2*) shows the energy level parabolas for Cr^{3+} ions. The laser excites an ion into an excited vibrational level of the $^4T_2$ band at point *A*. It can then relax within the $^4T_2$ band following the path through point *B* (where the two parabolas cross).

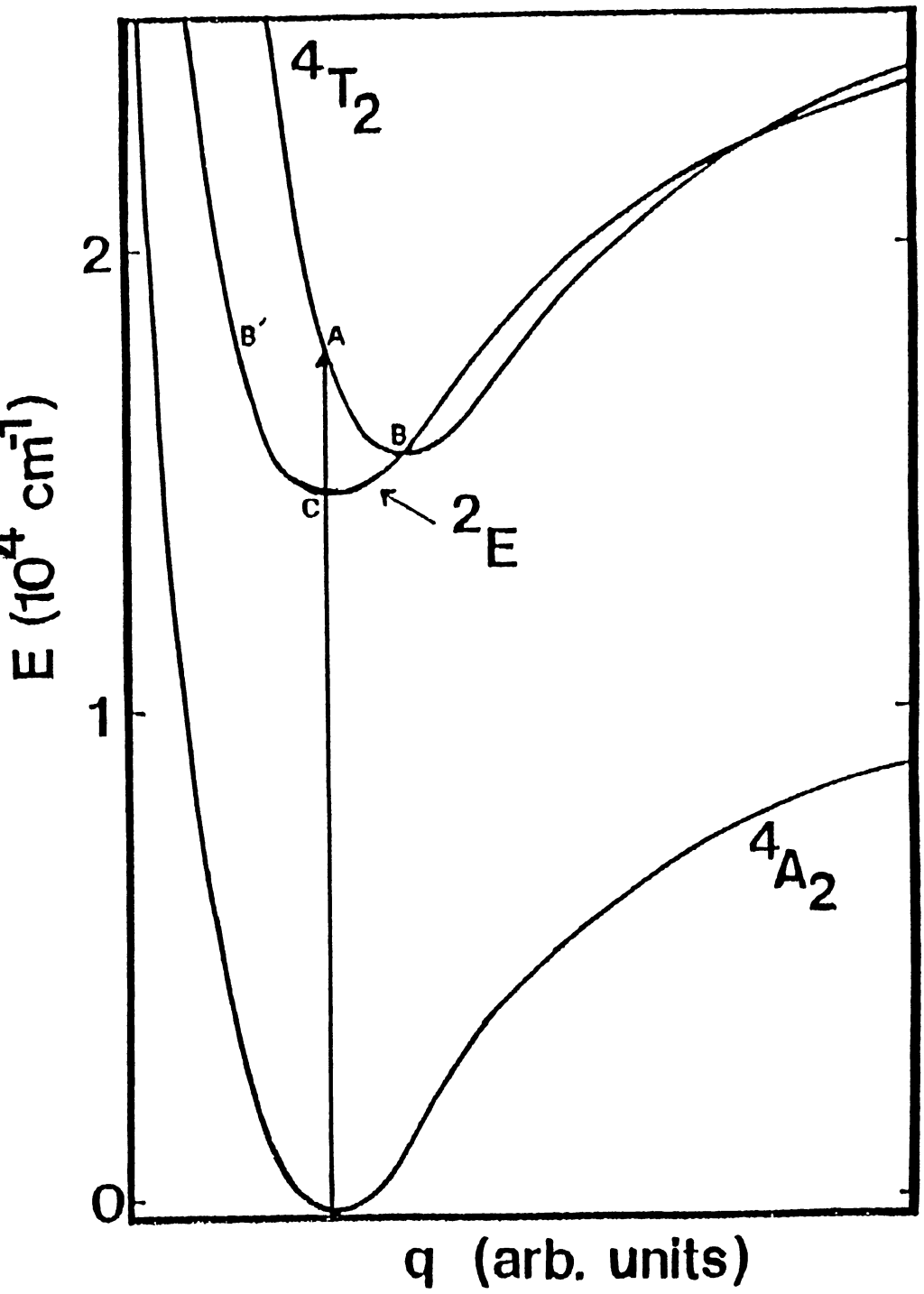

Figure 34. The Model Used to Analyze the Dynamics of Nonradiative Decay From $^4T_2$ Level to ^2E Level of the Cr^{3+} Ions in Alexandrite. The Vertical Line Represents the Optical Absorption (Adopted From Ref. 2). This Model Uses the Anharmonic Morse Potential.

The excitation then crosses over to the ^2E state and emits phonons until it reaches the bottom of the ^2E potential well. This process is called internal conversion (IC) and the corresponding nonradiative decay rate is denoted by $K_{nr}(IC)$. Alternatively, the excited ion can relax by immediately crossing over to the ^2E band at point B' and then emitting phonons to reach the bottom of the potential well. This process is called intersystem crossing (ISC) and the corresponding nonradiative decay rate is denoted by $K_{nr}(ISC)$. As noticed in *Ref. 2*, after the first step is taken, the entire path for the dephasing is determined. The dephasing time T_2 is directly affected by whether IC or ISC path is the preferred channel for the nonradiative relaxation. Since the details of this process are described in *Ref. 2*, we will only mention the important points.

The nonradiative decay rates are calculated using the standard perturbation theory techniques.[36] The vibrational matrix elements are calculated using a single effective phonon frequency and Morse potential wave functions to account for the anharmonicity.[37,66-72] The multi-electron reduced matrix elements involved here, are expressed in terms of the single-electron reduced matrix elements which have already been tabulated by Sugano et al.[21] Due to the difficulties involved in calculating the exact electronic wavefunctions needed for the evaluation of single electron matrix elements, only the ratio $K_{n.r.}(ISC)/K_{n.r.}(IC)$ of the two rates, is considered.

Calculations were performed for the Cr-doped laser materials, ruby, alexandrite, emerald, GGG, GGGM, and GSGG, which have been investigated by *FWM* spectroscopy. The results can be used to determine the relationship between the dephasing process and the energy difference between the peaks of the $^4A_2$ - $^4T_2$ and the $^4A_2$ - ^2E bands in the absorption spectrum denoted by ΔE_{pp}. Nonradiative decay rates were calculated for two possible dephasing paths and the results of calculations are given in *Table IX*.

It is interesting to note that for all the materials considered, the ratio $K_{n.r.}(ISC)/K_{n.r.}(IC)$ is greater than 1. This generalizes the conclusion drawn in *Ref. 2*, that in Cr-doped laser materials, after pumping into the $^4T_2$ level, the dominant relaxation path for the excitation is *ISC* and not *IC*.

In *Fig. 35*, the ratio $K_{n.r.}(ISC)/K_{n.r.}(IC)$ and the T_2-dephasing time are plotted as a functions of the energy splitting ΔE_{pp}, for excitation in the Cr-doped materials. The two quantities have the same dependence on ΔE_{pp}. To further demonstrate this relationship, the dephasing time T_2 is plotted as a function of $K_{n.r.}(ISC)/K_{n.r.}(IC)$ in *Fig. 36* and the result is a straight line.

Comparing the above results for the dephasing mechanism in Cr-doped materials, we conclude that internal conversion is the dominant relaxation path when the chromium ions are excited in the $^4T_1$ level. This is due to the fast relaxation of the excitation to the bottom of $^4T_1$

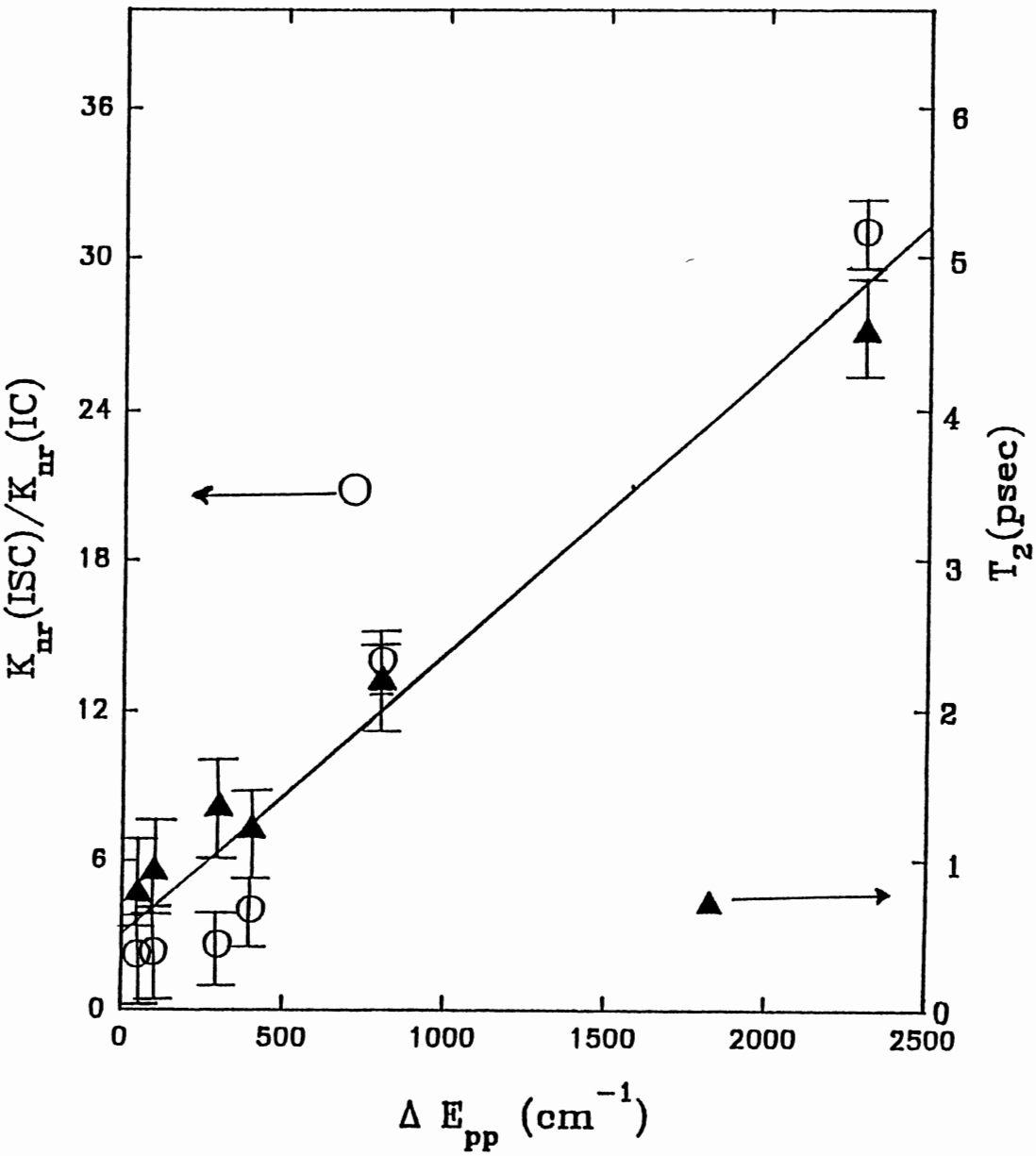

Figure 35. T_2-Dephasing Time and Ratio of the Decay Rates $K_{n.r.}(ISC)/K_{n.r.}(IC)$ as a Function of ΔE_{pp} (Energy Difference Between the Peak of ^2E Band and the peak of $^4T_2$ Bands in the Absorption Spectrum of Cr-Doped Crystals). This Model Uses Anharmonic Morse Potential.

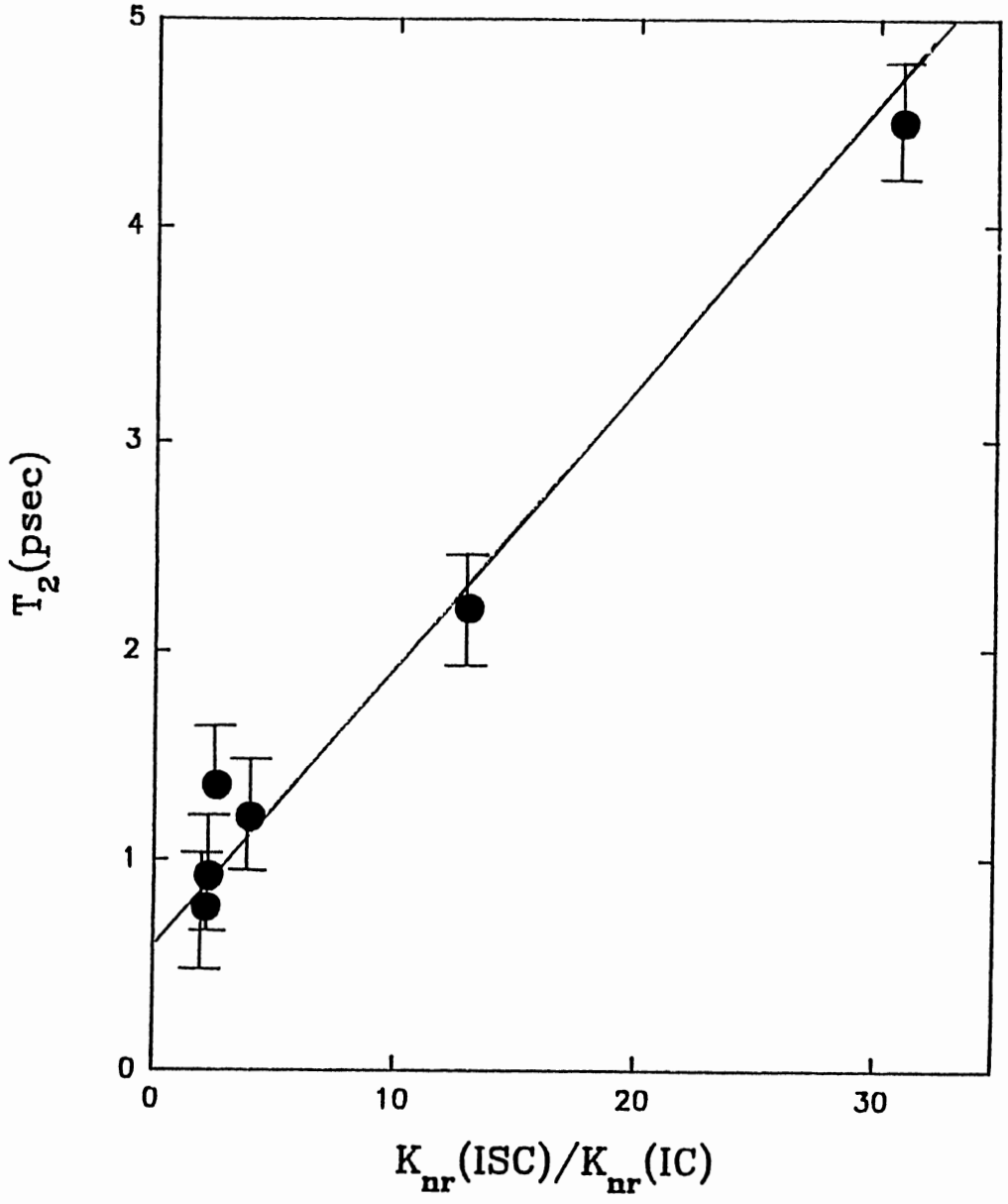

Figure 36. T_2-Dephasing Time as a Function of the Ratio $K_{n.r.}(ISC)/K_{n.r.}(IC)$. This Model Uses Anharmonic Morse Potential.

parabola. The information on optical dephasing obtained from *FWM* measurements after pumping into the $^4T_2$ level shows that radiationless relaxation to the ^2E level through intersystem crossing is the dominant dephasing process in these Cr-doped laser crystals and the relative importance of dephasing through internal conversion within the $^4T_2$ level becomes more important as the crystal field of the host decreases.

In order to check whether the anharmonic effects are necessary to explain the experimentally observed dephasing times, an alternative model of Donnelly et al.[38] was used. This model treats the vibrational potential corresponding to each electronic level as completely harmonic and the spin-orbit interaction couples the $^4T_2$ and ^2E levels. The wavefunctions for the ^2E and $^4T_2$ levels in this model are given by *Eq. (III-54)* and *Eq. (III-55)* respectively. The vibrational levels corresponding to each electronic level are shown in *Fig. 37* where the vibrational quantum numbers corresponding to different vibrational levels are shown besides the levels.

Using these wavefunctions, the rate for nonradiative decay from an excited vibrational level (where the ions are initially excited) to the bottom of the ^2E potential well can be written as

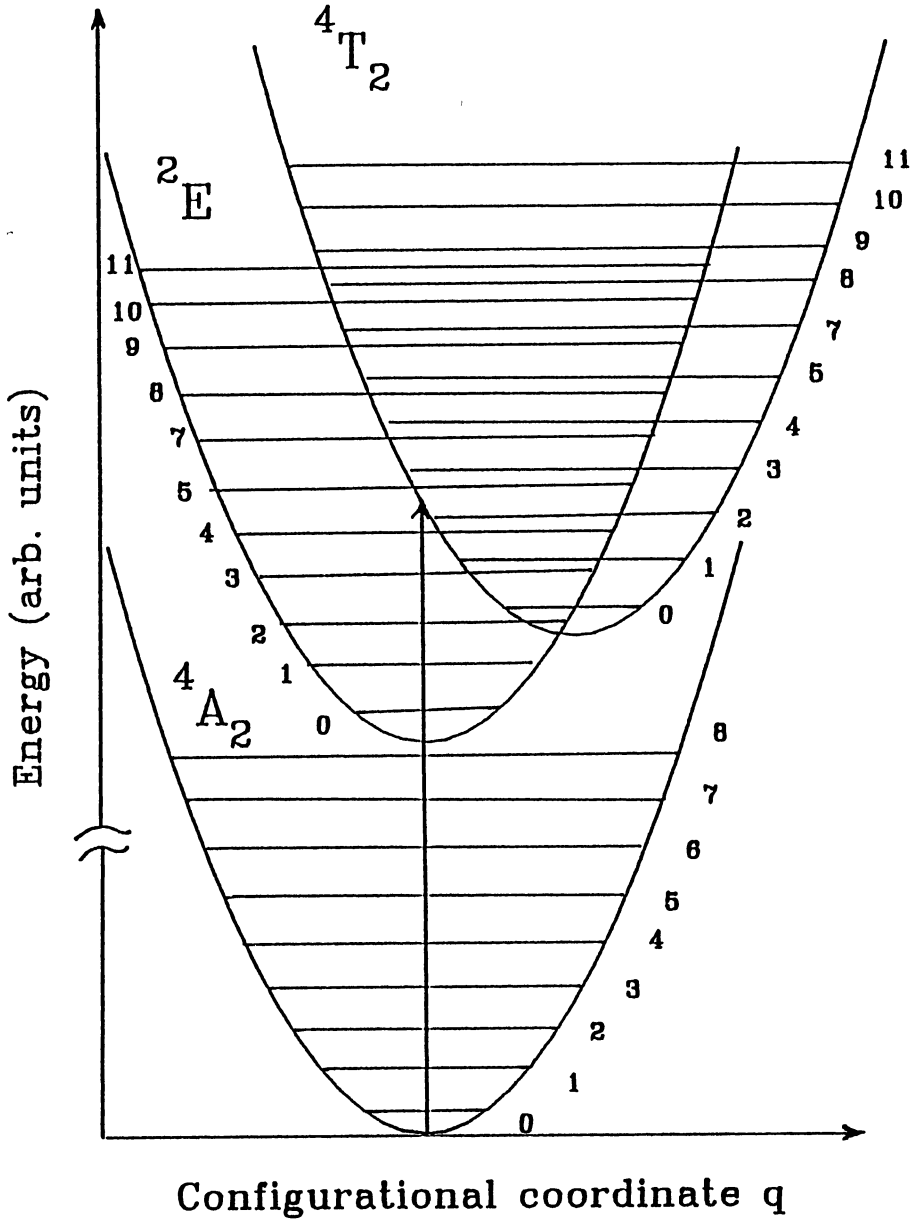

Figure 37. Configurational Coordinate Diagram for Ruby. The Horizontal Lines are the Harmonic Vibrational Levels Corresponding to ^2E, $^4T_2$ and $^4A_2$ Electronic Levels. The Numbers Shown Besides the Levels are Vibrational Quantum Numbers and the Vertical Line Represents the Optical Absorption.

$$K_{nr} = (4\pi^2/h)|\Sigma_m\Sigma_{M,\gamma}([1+\Sigma_\mu S^2(\alpha_\mu,\beta_m)][1+\Sigma_\nu S^2(\beta_m,\alpha_\mu)])^{-1/2}$$

$$x\ \rho(E_f)\{<^2E,\gamma,M|H_{s.o}|^4T_2,\gamma^*,M^*><\alpha_0|\beta_\nu>$$

$$+\ <^2E\gamma,M|V|^4T_2,\gamma^*,M^*><\alpha_0|q|\beta_\nu>$$

$$x\ \Sigma_\nu S(\beta_\nu,\alpha_0)[<^4T_2,\gamma,N|H_{s.o.}|^4T_2,\gamma^*,M^*><\beta_\nu|\beta_m>$$

$$+\ <^4T_2,\gamma,N|V|^4T_2,\gamma^*,M^*><\beta_\nu|\beta_m>]$$

$$x\ \Sigma_\nu S(\alpha_\mu,\beta_m)[<^2E\gamma^*M^*E|H_{s.o}|^2E\gamma^*,M^*><\alpha_0|\alpha_\mu>$$

$$+\ <^2E,\gamma^*,M^*|V|^2E,\gamma,M><\alpha_0|q|\alpha_\mu>]$$

$$x\ \Sigma_\mu\Sigma_\nu S(\beta_\nu,\alpha_0)S(\alpha_\mu,\beta_m)$$

$$x\ [<^4T_2,\gamma^*,M^*|H_{s.o.}|^2E,\gamma,M><\beta_\nu|\alpha_\mu>$$

$$+\ <^4T_2,\gamma^*,M^*|V|^2E,\gamma,M><\beta_\nu|q|\alpha_\mu>]\}|^2. \qquad \text{(IV-20)}$$

Here γ and γ^* represent the components of the respective group theoretical representations and M and M^* represent the z-component of the corresponding spin quantum number.

Phonons of different symmetries are involved in connecting the two levels and they are divided into promoting modes which mix the initial and the final electronic states and accepting modes which absorb the difference in the electronic energies. The vibrational wave function can therefore be written as,

$$|\alpha_\mu(\xi)> = \Pi_{1p}|\alpha_{\mu p}(\xi_p)>\Pi_{\mu\alpha}|\alpha_{\mu a}(\xi_a)>, \qquad \text{(IV-21)}$$

where ξ_a and ξ_p are the values of the harmonic oscillator

parameter ξ corresponding to the accepting and promoting modes respectively.

Calculations for several Cr-doped laser crystals were performed and the normalized results are shown in *Table X*. The values of the single electron reduced matrix elements are available in terms of the parameter ζ which is related to the physically measurable parameter *Dq*, and the energy shifts of the $|^2EM_\gamma>$ states, ΔE by the following relation[21]

$$\zeta = \sqrt{20}(\Delta E)Dq/3. \qquad \text{(IV-22)}$$

The normalized values calculated for the nonradiative decay rates are plotted in *Fig. 38* as a function of the crystal field splitting, ΔE_{pp}. In order to explore any correlation with the dephasing times, the nonradiative decay rates and the T_2-dephasing times are plotted side by side in *Fig. 39*. However, unlike the earlier model using anharmonic effects, no direct relationship between $K_{n.r.}$ and ΔE_{pp} is observed in this case. Comparing the results in *Fig. 35* and *Fig. 39*, we conclude that anharmonic effects are essential in order to explain the optical dephasing in Cr-doped materials and thus the model of Gilliland et al.[2] using the anharmonic potential appears to be a better method for describing the $^4T_2$ - ^2E radiationless decay processes in Cr-doped crystals. It should not be surprising however, because the pure harmonic vibrational potential is only a good approximation for very low energies so that the system is unaware of the anharmonicity.

TABLE X

NORMALIZED NONRADIATIVE DECAY RATES FOR OPTICAL DEPHASING AFTER $^4T_2$ EXCITATION IN Cr-DOPED LASER CRYSTALS.

Material	ΔE_{pp} (cm^{-1})	$K_{norm.}$	T_2 (psec)
Ruby	3850	19	4.5 ± 5
Alexandrite(M)	1950	34	2.2 ± 4
Emerald	1800	13	1.2
GGG	1650	11	1.35 ± 0.5
GGGM	1250	17	0.92 ± 0.5
GSGG	1150	7	0.77 ± 0.5

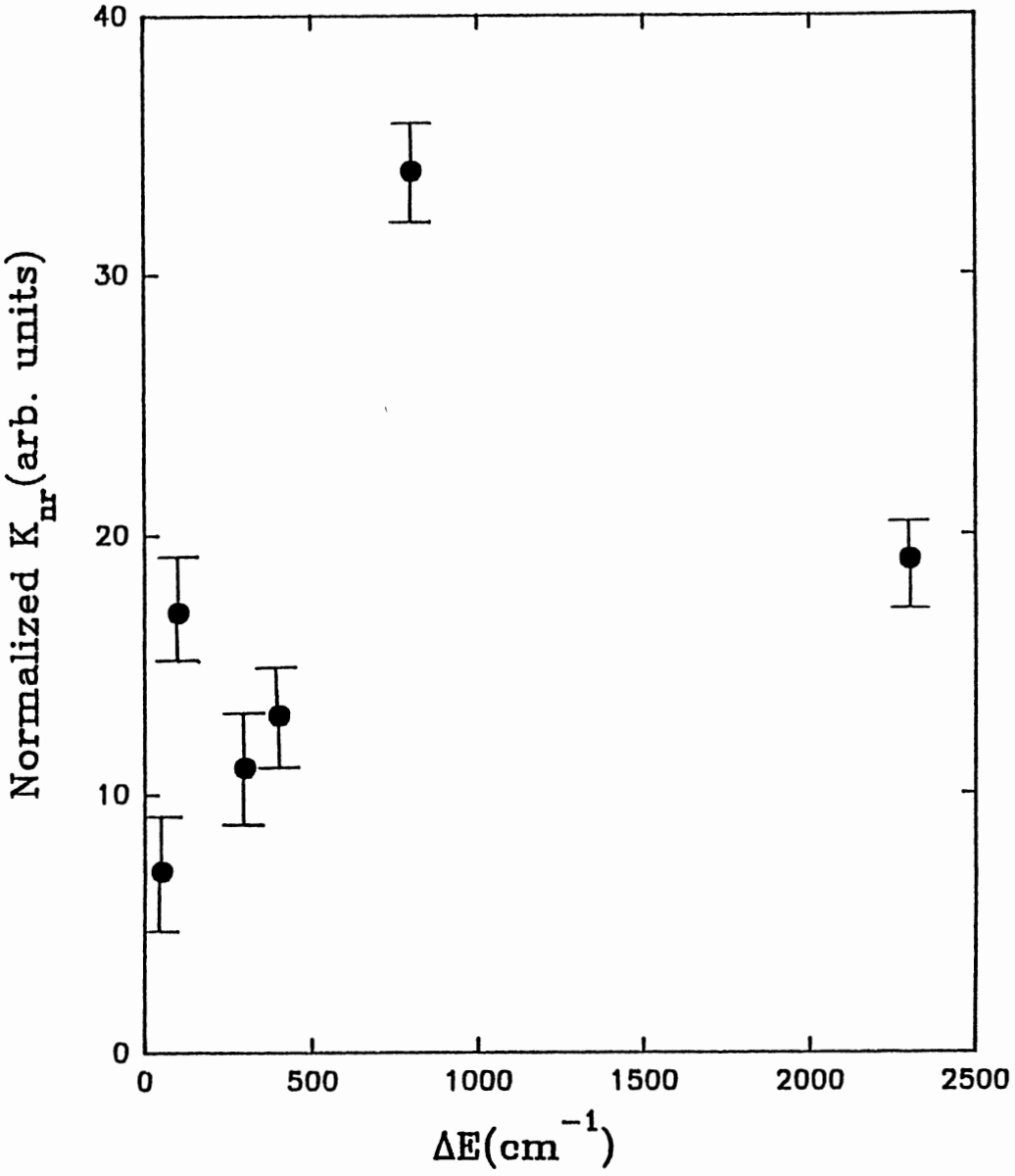

Figure 38. The Normalized Nonradiative Decay Rates as a Function of the Crystal Field Energy, ΔE_{pp}. This Model Uses the Harmonic Vibrational Potential.

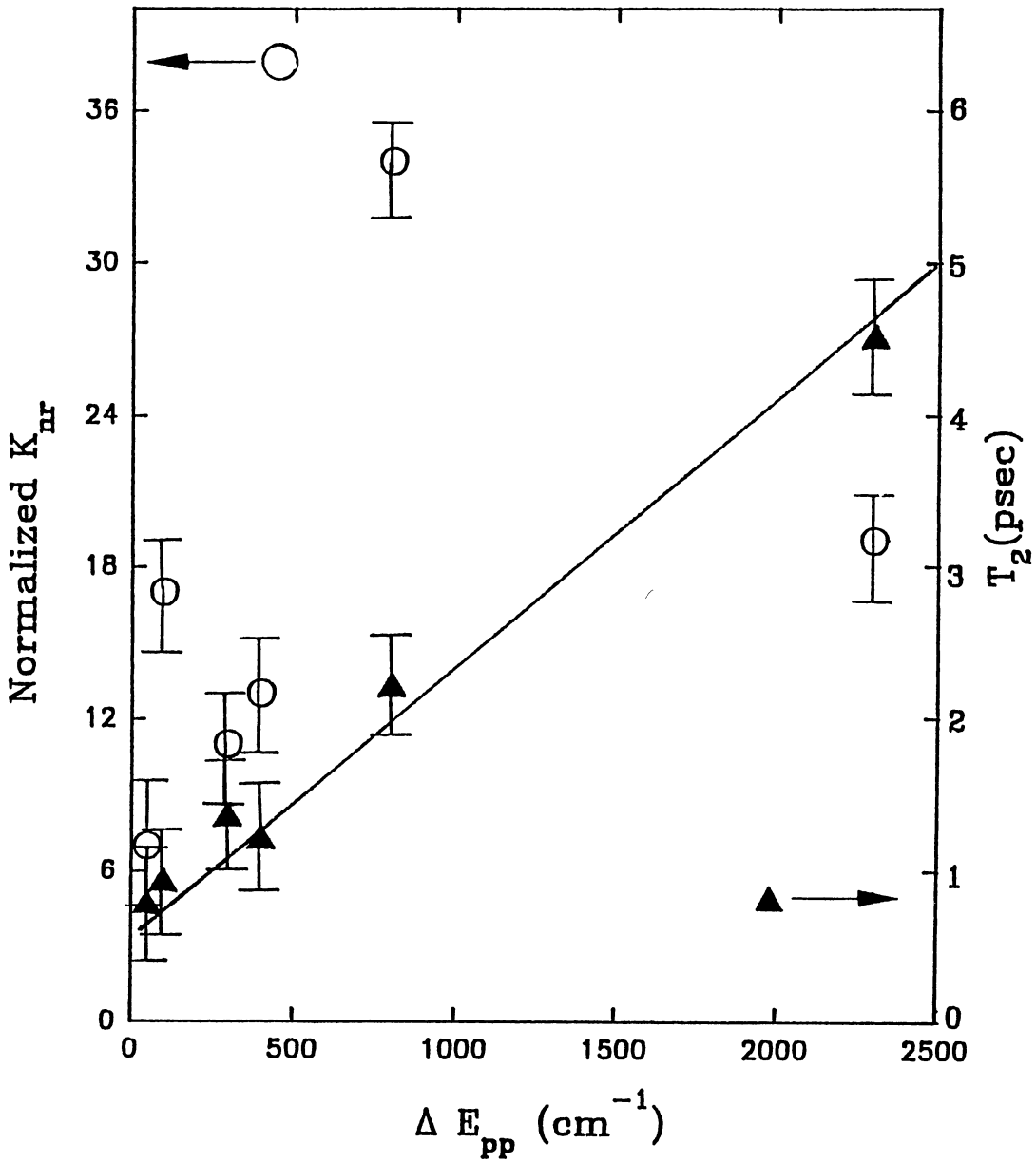

Figure 39. T_2-Dephasing Time and the Normalized Nonradiative Decay Rates $K_{n.r.}$ as a Function of ΔE_{pp} (Energy Difference Between the Peak of ^2E Band and the Peak of $^4T_2$ Band in the Absorption Spectrum of Cr-Doped Crystals). This Model Uses Harmonic Vibrational Potential.

Fluorescence Decay Properties of the Sensitizers

The success of flashlamp-pumped Nd^{3+} doped $Y_3Al_5O_{12}$ (Nd:YAG) crystals as a high power laser material despite the poor coupling of the pump light into Nd^{3+} absorption bands has prompted an interest in trying to find alternate ways to improve the pump efficiency. Introducing disorder in the garnet host lattice to produce inhomogeneous broadening of the spectral lines, and sensitized luminescence are two ways to achieve this goal. In Nd-doped materials using sensitized luminescence, the initially excited ions called sensitizers, transfer their energy to neodymium ions. By appropriately choosing the sensitizer ions, overall pump efficiency can be increased appreciably. For sensitized luminescence to be successful in Nd-doped laser crystals, the sensitizers must have broad absorption bands suitable for the available pump sources and their emission spectrum must overlap the absorption spectrum of the Nd^{3+} ions. The spectral location of the broad absorption and emission bands due to Cr^{3+} ions in low crystal field sites make it an ideal candidate for sensitized pumping of the Nd^{3+} in some codoped materials. However in Nd:YAG co-doped with Cr^{3+}, the spectral overlap between the Cr^{3+} emission and Nd^{3+} absorption is poor, so sensitized pumping is not effective.[73-75] In the mixed garnet crystal, due to the spectral location of absorption and emission band of Cr^{3+} and Nd^{3+}, the efficiency of energy transfer is expected to be greatly improved in the co-doped

sample.

The room temperature absorption spectrum, the energy levels of Cr^{3+} ions, and the energy levels of Nd^{3+} ions in GGGM are shown in *Fig. 40*. While the broad absorption bands of the Cr^{3+} ions allow effective coupling of the pump light into the chromium ions, the energy levels of Cr^{3+} and Nd^{3+} in this sample allow the possibility of very efficient nonradiative energy transfer from Cr^{3+} ions to Nd^{3+} ions. Therefore in the codoped sample, the excitation can migrate along the Cr^{3+} ions or it can transfer its energy to the Nd^{3+} ions via single-step transfer. The *FWM* techniques described above can only measure long-range energy migration that contributes to the decay of the laser induced population gratings. Therefore, in order to calculate the total nonradiative energy transfer from Cr^{3+} to Nd^{3+} in Cr,Nd:GGGM, it is necessary to study the fluorescence decay properties of chromium ions.

The decay of a sensitizer strongly depends upon the activator distribution in its surroundings. Many different energy transfer models have been developed, each applying to certain specific cases.[42,43,49,56-60,76-83] The Yokota-Tanimoto model[79] was used to describe the fluorescence decay of Cr^{3+} ions in the codoped sample. This model treats diffusion as a weak perturbation to the single-step transfer process. The interaction between chromium and neodymium ions in co-doped garnet crystals has been identified to be predominantly a dipole-dipole mechanism.[83] The

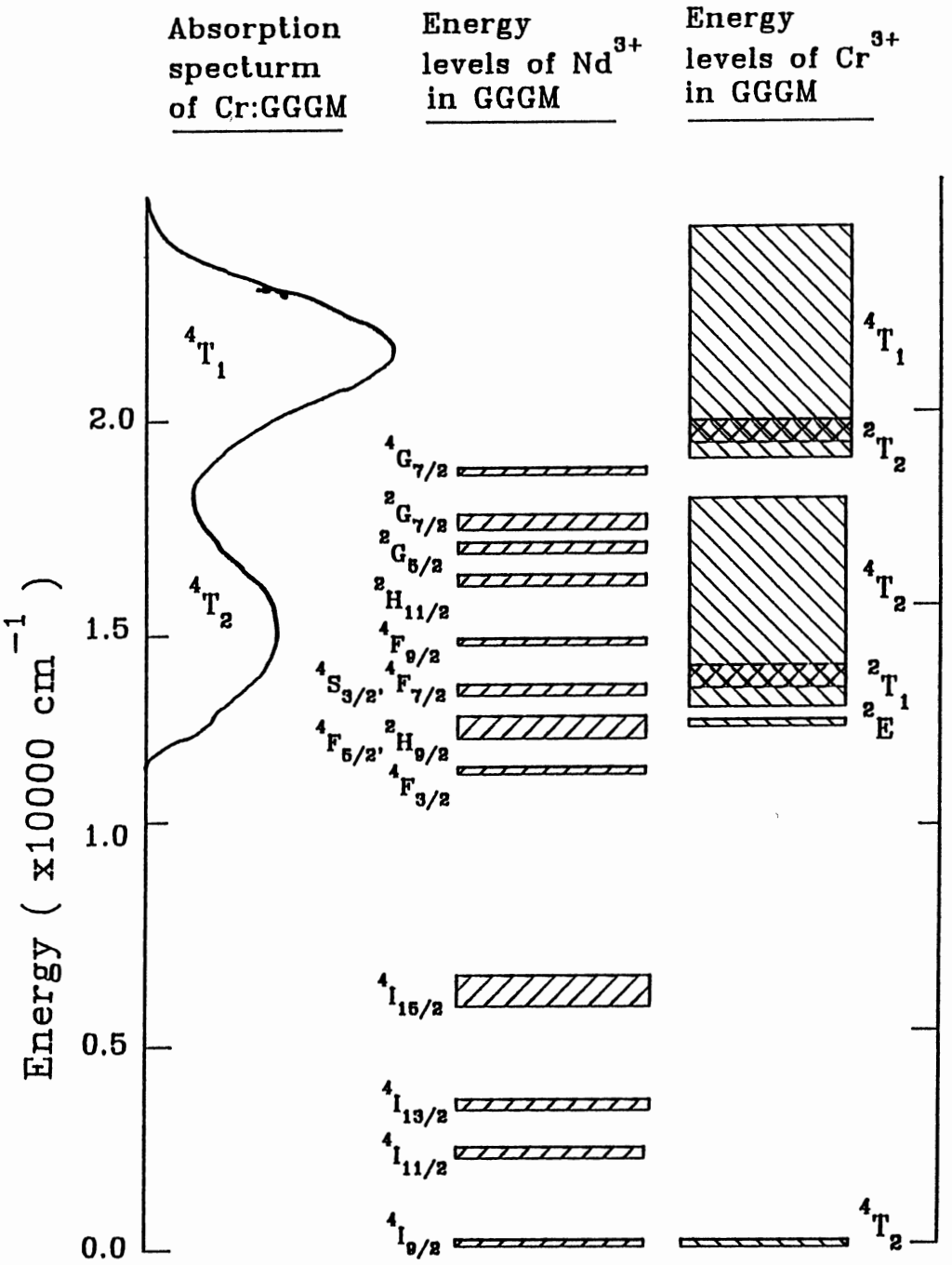

Figure 40. The Room Temperature Absorption Spectrum, The Energy Levels of Cr^{3+} Ions, and the Energy Levels of the Nd^{3+} Ions in GGGM.

normalized fluorescence intensity of the Cr^{3+} ions in Cr,Nd:GGGM can therefore be described by the following expression[79]

$$I(t)=\exp[-t/\tau_d-4/3\sqrt{\pi t/\tau_d}\pi R_0^3 n_{Nd}(1+10.87x+15.5x^2)/(1+8.74x)] \quad \text{(IV-23)}$$

where

$$x=[D/R_0^2](t^2\tau_d)^{1/3} \quad \text{(IV-24)}$$

and R_0 is the critical interaction distance given by,

$$R_0=\{3e^2f_sf_a\Omega\tau_s/8\pi^2m^2c^3\bar{\nu}^2\}^{1/6}, \quad \text{(IV-25)}$$

where f_s and f_a are the oscillator strengths corresponding to the sensitizers and activators respectively, Ω is the overlap integral and $\bar{\nu}$ is the average wavenumber in the region of spectral overlap.

The fluorescence decay of the Cr^{3+} ions at 30K is plotted in *Fig. 41*. The circles are the experimental points and the solid curve shows the best theoretical fit obtained using the above equation with R_0 as adjustable parameter and the value of D as determined from the *FWM* measurements. The best theoretical fit to the data yields a value of 9.2 Å for the critical interaction distance. A theoretical estimate of 5.9 Å for R_0 was obtained by using $f_s = 3.5 \times 10^{-5}$ (*Ref. 3*) and $f_a = 0.262$ (*Ref. 83*) in *Eq. (IV-25)*. This value is somewhat smaller than the one obtained by fitting the experimental data and the difference could be due to non-uniform distribution of ions

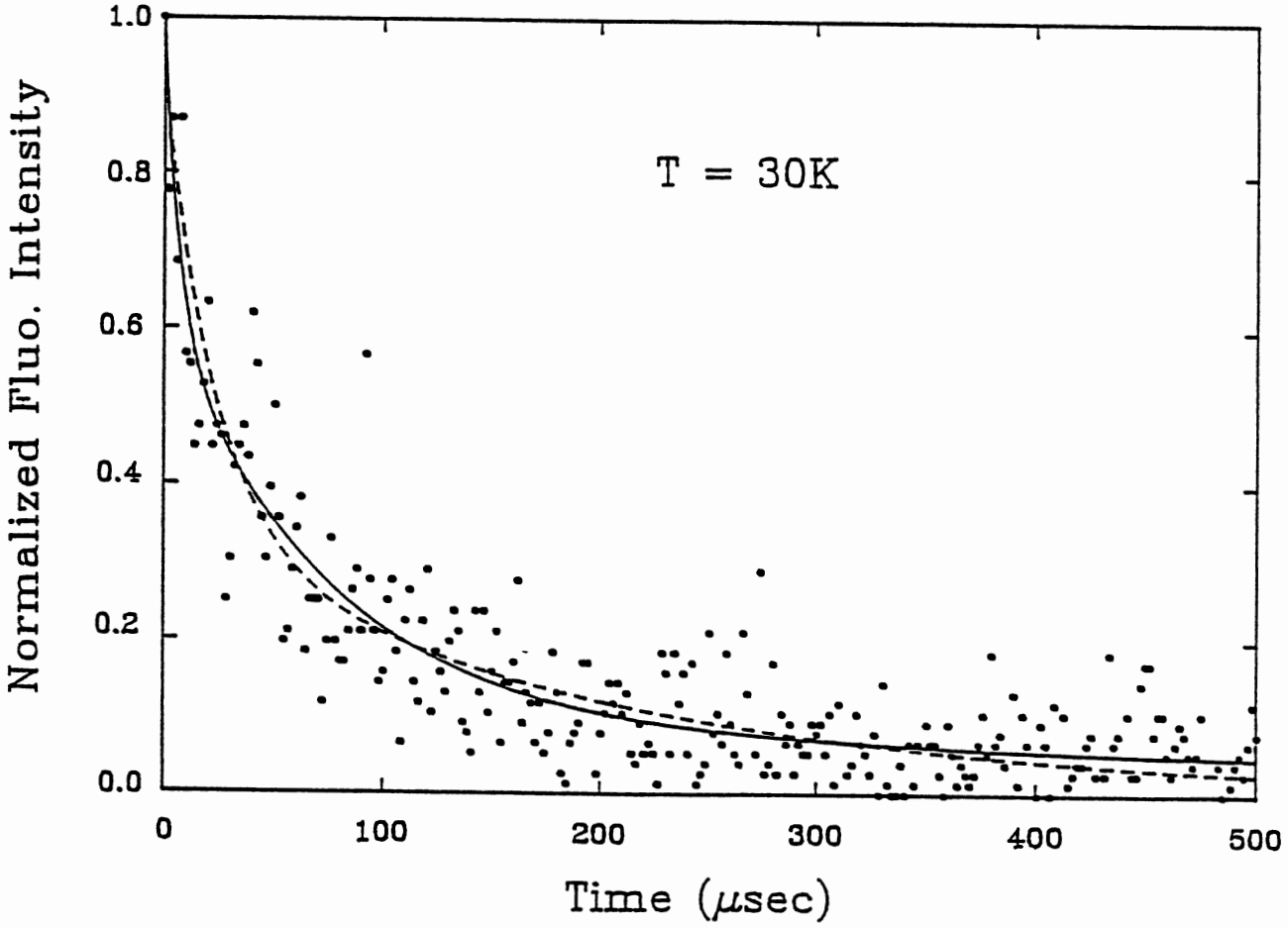

Figure 41. The Fluorescence Decay due to Cr^{3+} in Cr, Nd:GGGM. The Dots Represent the Experimental Data Points and Solid and Broken Curves Shows Theoretical Fits Using Yokota-Tanimoto and Huber Models for Energy Transfer Respectively.

resulting in a high local concentration. This value of R_0 corresponds to a Cr-Nd transfer rate of 2.1 x 10^4 sec^{-1} which agrees within the experimental limits to the Cr-Nd transfer rate calculated using the Huber model (to be discussed later). The experimental value of R_0 corresponds to 3.6 x 10^{-39} cm^6/sec for the microparameter, $C_{DA}(Cr\text{-}Nd)$ and this is compared to the similar values in other codoped garnet crystals in *Table. XI.* Although this value is much smaller than the corresponding values in most other garnet crystals, the large inhomogeneous broadening introduces the disorder which pushes the concentration quenching limit to much higher values and allows more flexibility to search for the optimum concentration and the larger transfer rate in Cr,Nd:GGGM, suggests that it could be an interesting material for pulsed lasers. The reduced value of the stimulated emission cross-section suggests that it might also be a good material for higher average power lasers.

The decay of the fluorescence in the codoped sample was monitored at 1.06 μm which corresponds to the $^4F_{3/2}$ - $^4I_{11/2}$ emission transition of the Nd^{3+} ions and the results are shown as the solid circles in *Fig. 42.* The maximum of the fluorescence observed at about 37 μsec is consistent with earlier results.[12] The curve is the theoretical fit to the data (circles) using the following expression for the activator decay derived using Yokota-Tanimoto diffusion model.[84,85]

TABLE XI

MICROPARAMETER C_{DA} FOR Cr-Nd ENERGY TRANSFER IN CO-DOPED GARNET CRYSTALS

Material	C_{DA}[Cr-Nd] (x 10^{-40} cm^6/sec)
$Y_3Al_5O_{12}$ [YAG]*	9
$(Gd,Ca)_3(Ga,Mg,Zr)_2Ga_3O_{12}$ GGGM	36
$Gd_3Ga_5O_{12}$ [GGG]*	110
$Y_3(Sc,Ga)_2Ga_3O_{12}$ [YSGG]*	140
$(La_{1-x},Lu_x)_3(Lu_{1-y},Ga_y)_2Ga_3O_{12}$ [LLGG]* [LLGG]	36
$Gd_3(Sc,Ga)_2Ga_3O_{12}$ [GSGG]*	220

*Data taken from *Ref. 46*

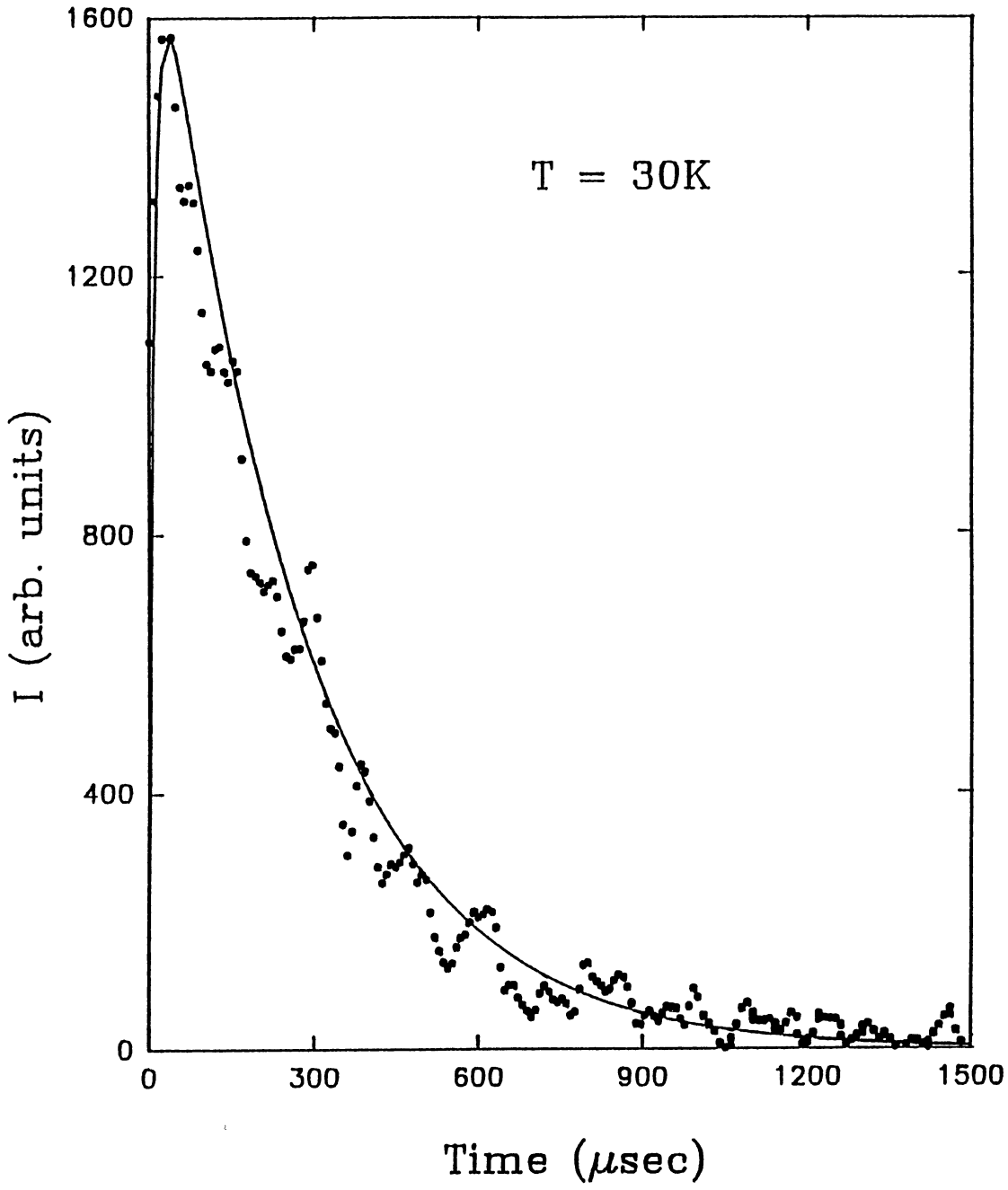

Figure 42. The Nd^{3+} Fluorescence Decay in Cr,Nd:GGGM. The Dots Shows the Experimental Data Points and the Solid Curve Represents Theoretical Fit Using Yokota-Tanimoto Model for Energy Transfer.

$$I_A(t)=\exp(-t/\tau_A)\int_0^t (2/3\pi^{3/2}/\sqrt{\tau_S}\exp(\xi/\tau_A)\xi^{-1/2}n_S(\xi)$$
$$+I_S(0)\exp\{91/\tau_A-1/\tau_S)\xi\}_n{}^{-1/2}[\exp(-4/3\pi^{3/2}\sqrt{\xi/\tau_S})$$
$$-\exp(-4/3\pi\sqrt{\pi\xi}/\tau_S Q(\xi))]\}d\xi, \qquad \text{(IV-26)}$$

where

$$Q(\xi)=\{(1+14.05Y\xi^{2/3}+23.02Y^2\xi^{4/3})/(1+11.55Y\xi^{2/3}, \qquad \text{(IV-27)}$$

and

$$Y = D\tau_S^{1/3}R_0^{-2}. \qquad \text{(IV-28)}$$

The value of the diffusion coefficient used in theoretical calculations is the same as found in *FWM* experiments. R_0 is treated as an adjustable parameter and its value for the best fit was found to be 7.9 Å. This is intermediate between the theoretical estimate of 5.9 Å and the value of 9.2 Å obtained by the best theoretical fit to the chromium fluorescence.

Huber and his coworkers[56-60] using the average T-matrix approximation (*ATA*), have developed a different model for energy migration among ions in solids that is useful when both energy migration as well as single-step transfer are present. The fluorescence response of the material is modeled through a survival function *f(t)* which is proportional to the probability that an ion excited at time $t = 0$, is still excited at time t. This survival function however does not include the removal of the

excitation by the trivial radiative decay. The effects of the distribution of active ions are accounted for by taking an average over all possible configurations. The Laplace transform *f(s)*, of the survival function can be written as

$$f(s) = [\ s + 4\pi c_A \int dr r^2 h(r,s)\ ]^{-1}, \qquad \text{(IV-10)}$$

where h(r,s) is the solution of the following integral equation,

$$h(r,s)=V(r)\{\sqrt{4\pi}-1/\sqrt{sD} * \int dx[\exp(-|r-x|)-\exp(-|r+x|)]h(x,s)x/r. \qquad \text{(IV-11)}$$

Where *D* is the energy diffusion coefficient and *V(r)* is the Cr-Nd interaction rate.

Equation (IV-10) and *Eq. (IV-11)* were numerically solved using *D* and the Cr-Nd transfer rate as adjustable parameters in the codoped sample and the best fit to the experimental data (dots) is shown as the broken curve in Fig. 41. The values of the parameters for the best fit were 2.57×10^{-7} cm^2/sec for energy diffusion coefficient and 3.57×10^3 sec^{-1} for Cr-Nd transfer rate. Within the limits of experimental errors, these values agree with the energy diffusion coefficient value obtained using the *FWM* experiments and the Cr-Nd transfer rate as measured using the fluorescence dynamics of the Cr^{3+} ions.

CHAPTER V

CONCLUSIONS

Investigation of the energy migration characteristics in mixed garnet crystals show a long-range excitation diffusion in all three samples. The diffusion coefficient for excitation migration in these samples has been measured as a function of temperature and its value at 30 K is 5.7 x 10^{-5} cm^2/sec in Cr:GGGM, 2.48 x 10^{-7} cm^2/sec in Nd:GGGM, 4.8 x 10^{-7} cm^2/sec for Cr^{3+} ions grating and 1.7 x 10^{-7} cm^2/sec for the Nd^{3+} ions grating in Cr,Nd:GGGM. The difference in the value of D in Cr:GGGM and Cr,Nd:GGGM under similar conditions can be explained as primarily due only to the difference in the concentration of Cr^{3+} ions in the two samples. The temperature dependence of the excitation diffusion coefficient in these samples show that the migration of the excitation in these samples is limited by scattering by acoustic phonons. A comparison of the D_{free} values for Nd-Doped crystals, shows that sample to sample variation in the values of $D_{meas.}$ is due to the change in the size of the lattice parameter. The larger lattice parameter helps in random distribution of the larger substitutional Nd^{3+} ions, making the excitation migration in these samples easier.

A comparison of the long-range energy migration in several Cr-doped laser crystals shows that the characteristics of the energy transfer vary significantly from host to host depending on the parameters such as the distance between the Cr^{3+} ions, the lifetime of the metastable state, the spectral overlap between the absorption and emission, and the electron-phonon interactions. The variation of each of these parameters from host to host makes it difficult to establish a simple trend for energy migration in *Cr*-doped crystals. The spacing a_0, between the sites of the lattice occupied by the optically active ions plays an important role in the energy migration. The absence of energy migration in ruby and the inversion site ions in alexandrite is primarily associated with the large values of a_0 in these samples. The decrease in the value of the ion-ion interaction rate V, from Alexandrite (M) to Emerald is associated with the decreased spectral overlap and, the increase in the case of GGGM is associated with the shorter fluorescence lifetime in this sample. The exciton-phonon scattering rate α, which limits the mean free path of the migrating energy varies from alexandrite (M) to GGGM and is found to increase with temperature. This increase in the exciton-phonon scattering rates is associated with the extra phonons available at higher temperatures. At low temperatures, the ion-ion interaction rates in alexandrite (M) and GGGM are independent of temperature. The value of D increases with temperature in

Emerald where V is phonon assisted but decreases with temperature in alexandrite (M) and GGGM where V is constant and α increases with temperature.

Efficient energy transfer from initially excited Cr^{3+} to Nd^{3+} ions in Cr,Nd:GGGM crystal is observed. The energy transfer in this sample takes place both radiatively and non-radiatively. The total non-radiative energy transfer Cr,Nd:GGGM is found to be due to weak diffusion among the Cr^{3+} ions accompanied by a strong single-step transfer from Cr^{3+} ions to Nd^{3+} ions. The large concentration of activators in this sample makes the single-step transfer much more probable than the long range diffusion.

The optical dephasing studies reported here indicate that anharmonicity of the vibronic potentials is required to explain the relationship between the T_2-dephasing time of the $^4T_2$ level and the crystal field splitting. It is also observed that for the dephasing mechanism in Cr-doped materials, the internal conversion is the dominant relaxation path when the chromium ions are excited to the $^4T_1$ level. This is due to the fast relaxation of the excitation to the bottom of the $^4T_1$ configuration potential well. The information on the optical dephasing process obtained from the *FWM* measurements pumping into the $^4T_2$ level, shows that radiationless relaxation to the ^2E level through intersystem crossing is the dominant dephasing process in these *Cr*-doped laser crystals. The relative importance of dephasing through internal conversion within

the $^4T_2$ level becomes more important as the crystal field of the host decreases.

Although the model using two level system approximation provides acceptable values of $\Delta\alpha$ and $\Delta\sigma$ in low excitation limit, it should however be approached with caution. This model is a very crude approximation of ions in solids which is a multilevel level system. The effective four level system model discussed here is a much better approximation and provides much more insight into the processes responsible for the creation of the grating.

The results obtained by the fluorescence decay of Cr^{3+} ions and Nd^{3+} ions, show an efficient sensitization of the neodymium ions by chromium ions in this host. The larger transfer rate suggests that this could be an interesting material for pulsed lasers.

The optical dephasing results obtained by the analysis of the excited state population grating can be used as a good first approximation. However, these results should be confirmed by direct measurement of the T_2-dephasing time using experiments like photon echo. The origin and the behavior of permanent gratings observed in these samples could provide interesting results about these mixed garnet samples and should be investigated in detail.

REFERENCES

1. A. Suchocki, G. D. Gilliland, and R. C. Powell, Phys. Rev. B 35, 5830 (1987).

2. G. D. Gilliland, A. Suchocki, K. W. Ver Steeg, R. C. Powell, and D. F. Heller, Phys. Rev. B 38, 6227 (1988).

3. F. M. Hashmi, K. W. Ver Steeg, F. Durville, R. C. Powell and G. Boulon, Phys. Rev. B 42, 3818 (1990).

4. A. Suchocki and R. C. Powell, Chem. Phys. 128, 59-71 (1988).

5. B. Struve, G. Huber, V. V. Laptev, I. A. Scherbakov and Y. V. Zharikov, Appl. Phys. B 28, 235 (1928).

6. B. Struve and G. Huber, J. Appl. Phys. 57 (1), 45 (1985).

7. E. V. Zharikov, N. N. Il'ichev, V. V. Laptev, A. A. Malyutin, V. G. Ostroumov, P. P. Pashinin and I. A. Shcherbakov, Sov. J. Quantum Electron. QE-12 338 (1982).

8. B. Struve, G. Huber, Appl. Phys. B 36, 195 (1985).

9. E. V. Zharikov, V. V. Laptev, E. I. Sidorova, Yu. P. Timofeev and I.A. Shcherbakov, Sov. J. Quantum Electon. QE-12, 1124 (1982).

10. G. Huber and K. Petermann, Tunable Solid State Lasers Vol. 47 eds. P. Hammerling, A. B. Budgore and A. Pinto (Springer, Berlin, 1985) p.11.

11. E. V. Zharikov, V. V. Osiko, A. M. Prokhorov and I. A. Shcherbakov, Izv. Akad. Nauk SSSR Ser. Fiz.48 1330 (1984).

12. G. Boulon, C. Garapon and A. Monteil, Advances in Laser Sciences II, eds. M. Lapp., W. C. Stwalley and G. A. Kenney-Wallace (A.I.P., New York, 1987) p.87.

13. A. Monteil, C. Garapon and G. Boulon, J. Lumin. 39,

167 (1988).

14. F. Durville, R. C. Powell, and G. Boulon, J. Phys. (Paris) Colloq. 48, C7-517 (1987).

15. C. Garapon, A. Monteil, and G. Boulon, J. Phys. (Paris) Colloq. 48, C7-493 (1987).

16. T. H. Allik, S. A. Stewart, D. K. Sardar, G. J. Quarles, R. C. Powell, C. A. Morrison, G. A. Turner, M. R. Kokta, W. W. Hovis, and A. A. Pinto, Phys. Rev. B 37, 9129 (1980).

17. G. Menzer, Z. Kristallogr. 63, 157 (1926).

18 S. Geller, J. Appl. Phys. 31, 30S, (1960).

19. S. Geller, Z. Kristallogr. 125, 1 (1967).

20. R. C. Powell, Ph. D. thesis, Air Force Cambridge Research Laboratories L.G. Hanscom field, Bedford, Massachusetts.

21. S. Sugano, Y. Tanabe, and H. Kamimura, Multiplets of Transition-Metal Ions in Crystals (Academic, New York, 1970).

22. H. J. Eichler, P.Gunter, and D. W. Pohl, Laser-Induced Dunamic Gratings (Springer-Verlag, Berlin, 1986).

23. H. Kogelnik, Bell Syst. Tech. J. 48, 2909 (1969).

24. J.R. Slcedo, A. E. Siegman, D. D. Dlott, and M. D. Fayer, Phys. Rev. Lett. 41, 131 (1978).

25. H. J. Eichler, J. knof, and Ch. Noack, Phys. Status Solidi A 52, 481 (1979).

26. D. S. Hamilton, D. Heiman, J. Feinberg, and R. W. Hellwarth, Opt. Lett. 4, 124 (1979).

27. P. F. Liao, L. M. Humphrey, D. M. Bloom, and S. Geschwind, Phys. Rev. B 20, 4145 (1979).

28. A. Yariv and D. M. Pepper, Opt. Lett. 1, 16 (1977).

29. P. F. Liao and D. M. Bloom, Opt. Lett. 3, 4 (1978).

30. R. L. Abrams and R. C. Lind, Opt. Lett. 2, 94 (1978).

31. A. E. Siegman, J. Opt. Soc. Am., 67, 545 (1977).

32. C. M. Lawson, Ph. D. Thesis, Oklahoma State University, (1981).

33. R. C. Powell, S. A. Payne, L. L. Chase, and G. D. Wilke, Phys. Rev. B 41, 8593 (1990).

34. Y. R. Shen, The Principles of Non-linear Optics (Wiley, New York, 1984).

35. M. D. Levenson, Introduction to Nonlinear Laser Spectroscopy (Academic, New York, 1982).

36. Eugen Merzbacher, Quantum Mechanics (John Wiley, New York, 1970).

37. P. M. Morse, Phys. Rev. 34, 57 (1929).

38. C. J. Donnelly, S. M. Healy, T. J. Glynn, G. F. Imbusch and G. P. Morgan, J. Lumin. 42, 119 (1988).

39. Y. M. Wong and V. M. Kenkre, Phys. Rev. A 22, 3072 (1980).

40. V. M. Kenkre and D Schmid, Phys. Rev. B 31, 2430 (1985).

41. M. Pardavi-Horwath and M. Osvay, Phys. Stat. Sol. (a) 80, K183 (1983).

42. S. Chandrasekhar, Rev. Mod. Phys. 15, 1 (1943).

43. D. L. Dexter, J. Chem. Phys. 22, 836 (1953).

44. R. J. Birgeneau, J. Chem. Phys. 50, 4282 (1969).

45. G. F. Imbusch, phys. Rev. 153, 326, (1967).

46. V. G. Ostroumov, Yu. S. Privis, V.A. Smirnov, and I. A. Scherbakov, J. Opt. Soc. Am. B 3, 81 (1986).

47. M. Kokta and M. Grasso, J. Solid State Chem. 8, 357 (1973).

48. J. C. Slater, Quantum Theory of Solids (McGraw-Hill Book Co., Nwew York, 1965).

49. V. M. Agranovich and M.D. Galanin, Electronic Excitation Energy Transfer in Condensed Matter (North-Holland, Amsterdam, 1982).

50. M. L. Shand, J.C. Walling and R.C. Morris, J. Appl. Phys. 52, 953 (1981).

51. T. F. Veremeichik, Phys. Status Solidi B 124, 719 (1984).

52. G. J. Quarles, A. Suchocki, and R. C. Powell, Phys. Rev. B 38, 9996 (1988).

53. R.C. Powell, A. Suchocki, G.D. Gilliland, G.J. Quarles, J. Lumin. 38, 250 (1987).

54. S. A. Basun, A. A. Kaplyanskii, V. N. Matrosov, S. P. Feofilov, A. A. Chernyshev, and A. P. Shkadarevich, Opt. Spektrosk. 66, 1067 (1989) [Opt. Spectros. (USSR) 66, 624 (1989)].

55. A. I. Burshtein, Sov. Phys. Usp. 27 (8), 579 (1984).

56. D. L. Huber, 20, 2307 (1979).

57. K.K. Ghosh, J. Hagarty, and D. L. Huber, Phys. Rev. B 22, 2837 (1980).

58. K. K. Ghosh, and D. L. Huber, J. Lumin. 21, 2381 (1971).

59. W. M. Yen, and P. M. Selzer, Laser Spectroscopy of Ions and Molecules in Solids, Chapter 4 (Springer Berlin, New York, 1984).

60. D. L. Huber, J. Lumin. 28, 475 (1983).

61. M. Zokai, R. C. Powell, G. F. Imbusch, and B. DiBartolo, J. Appl. Phys. 50, 5930 (1979).

62. L. D. Merkle, and R. C. Powell, Phys. Rev. B 20, 75 (1979).

63. W. M. Fairbank Jr., G. K. Klauminzer, and A. L. Schawlow, Phys. Rev. B 11, 60 (1975).

64. L. J. Andrews, S. M. Hitelman, M. Kokta, and D. Gabbe, J. Chem. Phys. 84, 5229 (1986).

65. S. C. Weaver, and S. A. Payne, Phys. Rev. B 40, 10727 (1989).

66. M. D. Sturge, Phys. Rev. B 8, 6 (1973).

67. B. I. Makshantsev, Opt. Spectrosk. 31, 355 (1977).

68. J. A. C. Gallas, Phys. Rev. A 21, 1829 (1983).

69. P. A. Fraser and W. R. Jarmain, Proc. Phys. Soc. London Sec. A 66, 1145 (1953)

70. J. A. C. Gallas, H. P. Grieneisen, and B. P. Chakarborty, J. Chem. Phys. 69, 612 (1978).

71. V.S. Vasan and R.J. Cross, J. Chem. Phys. 78, 3869 (1983).

72. R. Englman and B. Barnett, J. Lumin.3, 37 (1970).

73. A. G. Avanesov, B. I. Denker, V. V. Osiko, V. G. Ostroumov, V. P. Sakun, V. A. Smirnov, and I. A. Scherbakov, Sov. J. Quantum Electron. 12, 421 (1982) [Kvantovaya Elecktron (Moscow), 681 (1982)].

74. Z. J. Kiss and R. C. Duncan, Appl. Phys. Lett. 5, 200 (1964).

75. Z. J. Kiss, Phys. Rev. Lett. 13, 654 (1964).

76. T. Forster, Ann Phys. 2, 55 (1948); Z. Naturforsch 49, 321 (1949).

77. M. Inokuti, and F. Hirayama, J. Chem. Phys. 43, 1978 (1965).

78. M. Trlifaj, Czech. J. Phys. 6, 533 (1965); 8, 510 (1958).

79. M. Yokota, and O. Tanimoto, J. Phys. Soc. Jpn. 22, 779 (1967).

80. A. I. Burshtein, J. Lumin. 34, 167 (1985).

81. H. C. Chow, and R. C. Powell, Phys. Rev. B 21, 3785 (1980).

82. M. J. Weber Phys. Rev. B 4, 2932 (1971).

83. E. V. Zharikov, N. N. II'ichev, V. V. Laptev, A. A. Malyutin, V. G. Ostroumov, P. P. Pashinin, A. S. Pimenov, V. A. Smirnov, and I. A. Shcherbakov, Sov. J. Quantum Electron. QE-13, 82(1983).

84. N. Mortegi, and Shinoya, J. Lumin. 8, 1 (1973); P. Avouris, A. Campion, and M. A. ElSayed, Chem. Phys. Lett. 50, 9 (1977).

85. C. E. Swenberg and W. T. Stacy, Phys. Status Solidi 36, 717 (1969).

VITA

Faqir Mian Hashmi

Candidate for the Degree of

Doctor or Philosophy

Thesis: FOUR WAVE MIXING SPECTROSCOPY OF Cr^{3+} AND/OR Nd^{3+} -DOPED MIXED GARNET CRYSTALS

Major Field: Physics

Biographical:

Personal Data: Born in Quetta, Pakistan, September 9, 1956, the son of Raeesa and Salamat Hussain Hashmi. Married to Azizah Yahaya on December 28, 1989 and father of a son Sameer A. Hashmi.

Education: Graduated from Baluchistan University, Quetta, Pakistan in August, 1978 with major in Physics; Graduated from Southern Illinois University, Carbondale in 1983; Completed requirements for the Doctor of Philosophy degree at Oklahoma State University in July, 1992.

Professional Experience: Lecturer in the Physics Department of Baluchistan University Pakistan; Graduate Teaching Assistant at Oklahoma State University (1986,1992); Graduate Research Assistant in Center for Laser Research at Oklahoma State University (1987-91); Member of American Physical Society and Phi Kappa Phi.